Modélisation multi-échelle basée sur la microstructure de la déformation plastique dans les matériaux structurés harmoniques

Xiang Wang

ECOLE DOCTORALE GALILÉE (ED 146)

LSPM (CNRS)

THÈSE DE DOCTORAT

pour obtenir le grade de

DOCTEUR DE L'UNIVERSITÉ PARIS 13

Spécialité : Mécanique des Matériaux

par

Xiang WANG

Titre :

Microstructure-based multi-scale modeling of plastic deformation in harmonic structured materials

Soutenance publique prévue le 08 octobre 2020

Thèse soutenue devant le jury composé de :

Dmytro Orlov	Lund University, Sweden	Professeur	Rapporteur
Clément Keller	Insa de Rouen, France	Professeur	Rapporteur
Xu Chen	Tianjin University, China	Professeur	Examinateur
Véronique Doquet	École Polytechnique, France	Professeur	Examinatrice
Ioan Ionescu	Université Sorbonne Paris Nord	Professeur	Examinateur
Fabien Cazes	Université Sorbonne Paris Nord	MCF	Co-Encadrant
Guy Dirras	Université Sorbonne Paris Nord	Professeur	Co-Directeur de thèse
Jia Li	Université Sorbonne Paris Nord	Professeur	Directeur de thèse

Abstract

The 'harmonic structure (HS)' design method proposed by Ameyama and co-workers is the result of a relentless quest to obtain an improved combination of strength and ductility in metallic materials. Understanding the microstructure-property relationships and the underlying deformation mechanisms is of crucial importance in optimizing the microstructure design and quantitative prediction on mechanical properties. Although extensive experimental efforts have been made, it is found that these achievements are still insufficient for practical engineering needs. Experimental observations have shown that different harmonic structured materials generally exhibit different complex microstructures and accordingly different mechanical behavior, thus inducing distinctive deformation mechanisms. The objective of the present thesis is to develop a three-dimensional multi-scale numerical model to investigate the microstructure dependent mechanical behavior of different HS materials. An explicit self-consistent method called 'β-rule' is introduced into the model so that the direct meshing of a large number of grains for harmonic structured materials is averted and the gigantesque computation task is significantly reduced. A 3D crystal plasticity model for lamellar α+β colonies is adopted instead of the general crystal plasticity theory since the latter requires to explicitly constructing the mesh of the fine details of alternating laths of α phase and β phase. Besides, high fidelity modeling simulations are carried out to provide an insight into the microstructure-property relationships of Ti-6Al-4V with conventional homogeneous microstructure as well as the influence of strengthening effect of α/β phase interfaces. The developed model is capable of considering the influence of detailed microstructure features and crystallographic factors such as the anisotropy of slip strengths, the phase distributions, the realistic 3D textures, the length scale dependent critical resolved shear stress considering the grain boundary strengthening effect and the obstacle to slip transmission of α/β phase interfaces as well as a wide range of random grain orientations. The developed model is then implemented in a FE code Cast3M to numerically reproduce experimental tests concerning the monotonic and cyclic simple shear deformation of HS materials. The results obtained in the simulations are in good agreement with the experimental data.

Résumé

Le concept de « structure harmonique», SH, est une démarche mise en place pour répondre à la quête incessante pour obtenir une synergie entre la résistance et la ductilité dans les matériaux métalliques. Comprendre les relations entre la microstructure et les propriétés macroscopiques et les mécanismes de déformation sous-jacents est d'une importance cruciale pour optimiser la conception de la microstructure et la prévision quantitative des propriétés mécaniques. Bien que des efforts expérimentaux importants aient été faits, il s'avère que ces réalisations sont encore insuffisantes pour les besoins d'ingénierie pratique. Des observations expérimentales ont montré que différents matériaux structurés harmoniques présentent généralement des microstructures complexes différentes et en conséquence un comportement mécanique différent, induisant ainsi des mécanismes de déformation distinctifs. L'objectif de la présente thèse est de développer un modèle numérique multi-échelle en trois dimensions pour étudier le comportement mécanique dépendant de la microstructure de différents matériaux HS. Une méthode explicite auto-cohérente appelée 'β-rule' est introduite dans le modèle afin que le maillage direct d'un grand nombre de grains pour les matériaux structurés harmoniques soit évité et que la tâche de calcul gigantesque soit considérablement réduite. Un modèle 3D de plasticité cristalline pour les colonies lamellaires α+β est adopté à la place de la théorie générale de la plasticité cristalline car cette dernière nécessite de construire explicitement le maillage des détails fins des lattes alternées de la phase α et de la phase β. En outre, des simulations de modélisation haute fidélité sont effectuées pour fournir un aperçu des relations microstructure-propriété du Ti-6Al-4V avec une microstructure homogène conventionnelle ainsi que l'influence de l'effet de renforcement des interfaces de phase α/β. Le modèle développé est capable de prendre en compte l'influence des caractéristiques détaillées de la microstructure et des facteurs cristallographiques tels que l'anisotropie des forces de glissement, les distributions de phases, les textures 3D réalistes, la contrainte de cisaillement résolue critique dépendante de l'échelle de longueur en tenant compte de l'effet de renforcement des limites des grains et de l'obstacle pour faire glisser la transmission des interfaces de phase α/β ainsi qu'une large gamme d'orientations de grains aléatoires. Le modèle développé est ensuite implémenté dans un code FE Cast3M pour reproduire numériquement des tests expérimentaux en cisaillement simple

monotone ou cyclique des matériaux HS. Les résultats obtenus dans les simulations sont en bon accord avec les données expérimentales.

Acknowledgements

First of all, I would like to thank my principal supervisor Jia Li for his guidance, his help, and his support and the plenty of time he has dedicated to supervise my work. I would also like to express my gratitude to my advisor Fabien Cazes for his patience and his previous support and inspiration. I appreciate all their contribution, ideas and remarks.

I am also grateful to my co-supervisor Guy Dirras for the help and support he offered me. His knowledge and enthusiasm in science also inspire me a lot. It is important to mention Azziz Hocini and Zhe Zhang for their precious support and help in my research. I also want to thank David Tingaud for his valuable help and contribution in my experiments.

Finally, I would like to thank my parents and my wife, who mean the world to me, for everything they have given me, for their unconditioned support and understanding. I cannot imagine my life without you. I always feel guilty at not being able to spend time at home with you. I have been considering myself as the luckiest one in the world to have such great parents and good wife standing behind me with their love and support.

I am also grateful to Prof. Qian Gu and Prof. Yang Ke who have been leading me to academia when I was studying for my Master in China.

Table of contents

List of figures

Fig. 3.4 Experimental equipment: (a) shear test setup performed on an MTS M20 testing machine, (b) sample grasping device.

Fig. 3.5 Figures of the as-processed specimens: (a) and (c) IPF maps showing grain orientation ([0001] projection) for homogeneous coarse-grained CP-Ti and harmonic structured CP-Ti, respectively. The color code is relative to the standard stereographic projection triangle (inset); (b) and (d) figures showing the grain sizes and their distribution for homogeneous coarse-grained CP-Ti and harmonic structured CP-Ti, respectively (Hocini, 2017).

Fig. 3.6 IPF map alongside the texture strength measurement for the as-processed harmonic structured CP-Ti.

Fig. 3.7 Experimental results for (a) harmonic structured CP-Ti and homogeneous coarse-grained CP-Ti in the case of monotonic simple shear condition (b) hysteresis loops for harmonic structured CP-Ti and homogeneous coarse-grained CP-Ti in the case of cyclic simple shear condition when $\Delta\Gamma=1.155\%$ every cycle.

Fig. 3.8 Figures illustrating the microstructure of the as-processed specimens: (a) and (c) IPF maps showing grain orientation ([0001] projection) for homogeneous coarse-grained Ti-6Al-4V and harmonic structured Ti-6Al-4V, respectively. The color code is relative to the standard stereographic projection triangle (inset); (b) and (d) figures showing the grain sizes and their distribution for homogeneous coarse-grained Ti-6Al-4V and harmonic structured Ti-6Al-4V, respectively (Hocini, 2017). Notice the grain size gradient in the fine-grained regions (blue $\approx$0.45-2 μm; green $\approx$2-5 μm).

Fig. 3.9 Energy-dispersive X-ray spectroscopy map showing the relative abundance of chemical elements in α lath and β lath.

Fig. 3.10 Grain size (a) and IPF (b) maps, alongside the texture strength measurement (c) for the as-processed harmonic structured Ti-6Al-4V. Texture strength is expressed by the scale level at the bottom of (c).

Fig. 3.11 Experimental results for (a) harmonic structured Ti-6Al-4V and homogeneous coarse-grained Ti-6Al-4V in the case of monotonic simple shear condition (b) hysteresis loops for harmonic structured Ti-6Al-4V and homogeneous coarse-grained Ti-6Al-4V in the case of cyclic simple shear condition when $\Delta\Gamma=1.155\%$ every cycle.

Fig. 4.1 (a) Representation of the microstructure for bimodal α-β Ti-6Al-4V containing 180 grains/colonies in total, where the widths of β rib and α lath are

respectively 0.23μm and 1.36μm, and the volume fraction of equiaxed α grains is 50.0%. Equiaxed α grains are colored arbitrarily. Lamellar α+β colonies are colored using a binary color scale, where blue represents the α lath, red represents the β rib. (b) Examples of the generated α grains and lamellar colonies with random shape and different lamellae normal (represented by black arrows).

Fig. 4.2 Simulated stress-strain curve for the bimodal α-β Ti-6Al-4V with offset yield line (dashed).

Fig. 4.3 Volume averaged tensile stress for each equiaxed α grain and lamellar colony, at the overall strain of 1%, is plotted as a function of the angle between c-axis and loading direction z axis for the case where the influence of the lamellar microstructure on slip activities is considered by means of Eq. 4.10. Red points represent the response of lamellar colonies and green points represent the response of equiaxed α grains.

Fig. 4.4 Distributions of tensile stress in z direction at the overall strain of 1% obtained from simulation considering the influence of the lamellar microstructure on slip activities by Eq. 4.10, for colonies whose c-axis is at (a) a 4.4 degree and (b) a 1.9 degree to loading direction z axis. In the mesh, red represents β lamellae, colored parts represent α lamellae.

Fig. 4.5 Distributions of tensile stress in z direction at the overall strain of 1% obtained from simulation considering the influence of the lamellar microstructure on slip activities by Eq. 4.10, for colonies whose c-axis is at (a) a 40.9 degree and (b) a 34.4 degree to loading direction z axis. In the mesh, red represents β lamellae, colored parts represent α lamellae.

Fig. 4.6 Volume averaged tensile stress for each equiaxed α grain and lamellar colony, at the overall strain of 1%, is plotted as a function of the angle between c-axis and loading direction z axis for the case where the influence of the lamellar microstructure on slip activities isn't considered by means of Eq. 4.10. Red points represent the response of lamellar colonies and green points represent the response of equiaxed α grains.

Fig. 4.7 Distributions of tensile stress in z direction at the overall strain of 1% obtained from simulation considering the influence of the lamellar microstructure on slip activities by Eq. 4.10, for colonies whose c-axis is at (a) a 4.4 degree, (b) a 1.9 degree, (c) a 40.9 degree and (d) a 34.4 degree to loading direction z axis. In the mesh, red represents β lamellae, colored parts represent α lamellae.

every colored region is an equivalent grain representing a lamellar α+β colony as shown in (b), and 50 lamellar α+β colonies are created.

Fig. 6.5 Simulated overall stress-strain curves under monotonic simple shear loading corresponding to ten sets of random grain orientations.

Fig. 6.6 (a) Illustration of FE mesh used in the test of β-rule, (b) Numerical results obtained by FE model test for β-rule and polycrystalline simulation and the comparison with experimental data for homogeneous CG Ti-6Al-4V under monotonic simple shear loading condition.

Fig. 6.7 Illustration of RVEs including (a) 30, (b) 50 and (c) 100 CG regions for HS Ti-6Al-4V, where every colored part represents a CG region and the white part represents FG regions.

Fig. 6.8 Effect of the number of CG regions in the FE model on the overall response of HS Ti-6Al-4V under monotonic simple shear loading condition.

Fig. 6.9 Comparison between simulations and experimental results for homogeneous CG Ti-6Al-4V and HS Ti-6Al-4V in the case of monotonic simple shear condition.

Fig. 6.10 Simulated curves and experimental results for (a) homogeneous coarse-grained Ti-6Al-4V and (b) harmonic structured Ti-6Al-4V in the case of cyclic simple shear condition when $\Delta\Gamma$=1.155% every cycle.

Fig. 6.11 Effective shear stress distribution for (a) HS CP-Ti when Γ=24.0% and (b) HS Ti-6Al-4V whenΓ=12.7%.

Fig. 6.12 Effective shear stress distribution for (a) homogeneous CG CP-Ti when Γ=24.0% and (b) homogeneous CG Ti-6Al-4V when Γ=12.7%.

Fig. 6.13 Effective shear strain distribution for (a) homogeneous CG CP-Ti when Γ=24.0% and (b) homogeneous CG Ti-6Al-4V when Γ=12.7%.

Fig. 6.14 Simulated responses to variations in volume fraction of FG regions conducted on synthetic specimens (a) for HS CP-Ti and (b) for HS Ti-6Al-4V in comparison with simulations for experimental specimens.

Fig. A.1 Images showing the implementation of 'β-rule' in the present numerical model.

Fig. B.1 Illustration of meshes used in (a) polycrystalline simulation, where every colored part represents an equivalent grain and (b) "β-rule" simulation.

Fig. B.2 Simulated overall stress-strain curves under monotonic simple shear loading corresponding to ten sets of randomly generated crystalline orientations.

Fig. B.3 Distributions of (a) shear stress and (b) shear strain at the overall strain of

12.7% predicted by polycrystalline simulation.

Fig. B.4 Illustration of intergranular heterogeneity based on the volume averaged responses of 50 equivalent grains for lamellar α+β colonies.

Fig. B.5 Intragranular heterogeneity: (a) response at three volume averaged local strains (E = 5.1%, 9.7%, 14.1%) of all the points in grain10, (b) response at three volume averaged local strains (E = 4.1%, 8.1%, 12.2%) of all the points in grain39.

Fig. A.6 Fitting on monotonic simple shear test, the overall response of calibrated β-model is compared with that of polycrystalline simulation.

Fig. B.7 (a) Illustration of intergranular heterogeneity predicted by β-rule simulation, (b) the comparison of intergranular heterogeneities between polycrystalline simulation and β-model simulation, where the dotted lines represent the upper and lower bounds of each simulation.

Fig. B.8 Local responses for four selected equivalent grains obtained from polycrystalline simulation and β-model simulation under simple shear loading.

Fig. B.9 Validation of the calibrated parameters in β-model: comparison between the polycrystalline simulation and β-model, (a) monotonic tensile test and (b) cyclic simple shear test.

List of tables

Nomenclature

All symbols are also defined in the text.

Symbol	Description	Units
F	Tensile force	N
A	Cross-sectional area	mm^2
τ	Resolved shear stress	MPa
ϕ	Angle between F and the normal to the slip plane	º
λ	Angle between F and the slip direction	º
F_p	Plastic deformation gradient	-
F_e	Elastic deformation gradient	-
F	Total deformation gradient	-
L	Overall velocity gradients	-
L_e	Elastic velocity gradient	-
L_p	Plastic velocity gradient	-
γ^α	Shear strain on given slip systems	-
S^α	unit vector along slip direction	-
M^α	Unit vector along the slip plane normal	-
ψ	Function defining the elastic domain	-
$\dot{\gamma}^\alpha$	Shear strain rate on given slip systems	-
τ_α	Resolved shear stress on slip system α	MPa
$\hat{\tau}_\alpha^p$	Threshold function representing slip resistance	-
N_{sys}	Total number of slip systems	-
χ^α	Back stress for slip system α	MPa
k^α	Threshold stress representing the initial yielding	MPa
R^α	Isotropic stress	MPa
D^α	Drag stress representing the slip resistance	MPa
m	Strain-rate sensitivity parameter	-
E^e	Elastic Green-Lagrange deformation tensor	-
C	Elastic stiffness tensor	-
T	Second Piola-Kirchhoff stress tensor	-

$\boldsymbol{\sigma}$	Cauchy stress	MPa
$\boldsymbol{m}^{\alpha}$	Symmetric part of the Schmid tensor	-
$\boldsymbol{\sigma}^{g}$	Granular Cauchy stress	MPa
$\boldsymbol{\Sigma}$	Overall equivalent stress	MPa
$\boldsymbol{E}^{P}$	Plastic part of the overall strain tensor	-
$\boldsymbol{\varepsilon}^{pg}$	Plastic part of local strain in a given grain	-
C^{g}	Material parameter	GPa
$\boldsymbol{\beta}^{g}$	Phenomenological variable	-
$\boldsymbol{B}$	Mean of variable $\boldsymbol{\beta}^{g}$ for all grains	-
f^{g}	Volume fraction	-
$\dot{\boldsymbol{\beta}}^{g}$	Representing the evolution of $\boldsymbol{\beta}^{g}$	-
$\dot{\boldsymbol{E}}^{gp}$	Granular plastic strain rate	-
tot	Total number of slip systems in the slip geometry	-
Γ	Constant overall strain rate	-
$\Delta\Gamma$	Increments of the overall strain amplitudes	-
u	Displacement of the moving grip	mm
h	Width of the shear zone	mm
D	Average grain/colony size	μm
l_{α}	Average width of α lath in lamellar α+β colony	μm
l_{β}	Average width of β rib in lamellar α+β colony	μm
$V_{\alpha-grain}$	Volume fraction of equiaxed α grains	-
$V_{\beta-lath}$	Volume fraction of total β phase	-
$\boldsymbol{C}(\alpha,\beta,\gamma)$	Elasticity stiffness tensor function	-
α,β,γ	Euler angles	°
Q	Saturation of isotropic hardening variable R^{i}	MPa
a	Isotropic hardening modulus	-
k_{0}	Constant frictional stress	MPa
d^{i}	Widths of α lath and the β rib	μm
k_{y}	Hall-Petch constant	-
v^{α}	Volume fractions of α phase	-

| v^β | Volume fractions of β phase | - |

Abbreviation

The following table describes the interpretations of abbreviations and acronyms used throughout the thesis. Nonstandard acronyms that are used in some places to abbreviate the names of certain terminologies are not in this list.

Abbreviation	Meaning
CPFEM	Crystal Plasticity Finite Element
CP	Crystal Plasticity
BCC	Body Centred Cubic
FCC	Face Centred Cubic
HCP	Hexagonal Close Packed
CG	Coarse-Grained
FG	Fine-Grained
UFG	Ultrafine-Grained
HS	Harmonic Structure
CRSS	Critical Resolved Shear Stress
RVE	Representative Volume Element
EBSD	Electron Backscatter Diffraction
UMAT	User Material Subroutine
GND	Geometrically Necessary Dislocation
SSG	Statistically Stored Dislocation
ECM	Equivalent Constitutive Model

Chapter 1 Introduction

Titanium and its alloys are widely used in many applications ranging from aircraft, spacecraft, and medical devices to sports equipment (Geetha et al., 2009; Boyer, 1996; Leyens and Peters, 2003) due to their high corrosion resistance, biocompatibility and high strength-to-weight ratio. The relentless quest to obtain an improved combination of strength and ductility in titanium and its alloys has boosted the improvement of some microstructure manipulation methods using purposely deploying heterogeneous microstructures in metallic materials during the past decades. Among those new material processing routes, the 'harmonic structure (HS)' design method proposed by Ameyama and co-workers provides good control of the grain size distribution, the volume fraction and the spatial arrangement of heterogeneity, thus being our focus in this study.

Depending on the different applications, components made of HS titanium and its alloys may undergo various loadings. Understanding the deformation of these materials is therefore crucial for the efficient design of the harmonic structure. For this purpose, numerical studies providing an insight into the deformation mechanisms of plasticity and the physics of the deformation processes have to be carried out. Efficient numerical models for the HS materials require considering the influence of detailed microstructural features and the role of physical aspects.

Microstructures of metallic materials have strong influences on the deformation behavior at both the crystal scale and macroscopic scale. During the past decades, considerable effort has been devoted to understanding and simulating kinds of metallic materials at the microstructural scale in the quest to gain a fundamental understanding of the mechanism of plasticity processes which originate from crystal scale. In metals, the plasticity development at macroscopic scale is always closely linked with crystalline orientation distribution, crystal morphology and crystal structure as well as interaction between neighboring grains.

Over the past decades, considerable experimental studies have been carried out to apply the concept of harmonic structure design to various metallic materials and to investigate their mechanical properties. Researchers have also attempted to understand deformation mechanisms based on experimental observations of HS stainless steel (Park et al., 2018; Zhang et al., 2014). Additionally, in contrast to the numerous experimental efforts, only few modelling works have been performed in the

literature dealing with HS CP-Ti (Vajpai et al., 2016; Yu et al., 2015; Liu et al., 2018). To the authors' knowledge, no systematical numerical study has ever been reported to explore the deformation mechanisms for HS Ti-6Al-4V. It's then believed that understanding in detail the mechanics of plastic flow and damage through analytical and numerical modelling are among main priorities in developing HS materials now (Dmytro and Ameyama, 2020). Due to the difficulties faced in experimental and numerical researches which is directly caused by the complex microstructures possessed by harmonic structured CP-Ti and Ti-6Al-4V, the deformation mechanism and strengthening mechanism are not fully studied, especially for Ti-6Al-4V. Therefore, our work will be focused on the study of microstructure-based crystal plasticity model with respect to the HS CP-Ti and Ti-6Al-4V. By inspecting the plasticity development for these materials, this thesis work attempts to provide an insight into deformation and strengthening mechanisms of materials using the concept of harmonic structure design.

First, the high fidelity modeling simulations are also carried out where the fine details of alternating laths of α phase and β phase in lamellar α+β colonies are explicitly meshed in the FE model. The simulations provide us an insight into the microstructure-property relationships of Ti-6Al-4V with conventional homogeneous microstructure as well as the influence of strengthening effect of α/β phase interfaces which is a fundamental component of the crystal plasticity model for lamellar α+β colonies.

Afterwards, we move forward the previous numerical works by performing 3D crystal plasticity finite element method (CPFEM) based RVE simulations of CP-Ti and Ti-6Al-4V with conventional 'homogeneous' microstructure for different microstructural lengths and crystalline orientations in a polycrystalline material. These simulations are further used to testify the performance of a self-consistent scale transition rule called 'β-rule' in simulating the mechanical behavior of polycrystalline Ti-6Al-4V with conventional 'homogeneous' microstructure. Microstructure characterizations show that harmonic structured materials generally have huge contrast between the grain sizes in fine-grained (FG) and coarse-grained (CG) regions as well as complex microstructures. Consequently, it's very difficult if not impossible to construct FE meshes with high fidelity representation of microstructural details. A multi-scale numerical model, which incorporates the crystal plasticity and scale transition rule, is then established to explore an efficient way to simulate the

mechanical behavior of harmonic structured CP-Ti and Ti-6Al-4V. Both macroscopic stress-strain curves and distribution of local fields have been investigated to provide an insight into the strengthening mechanism and the deformation mechanism of HS CP-Ti and Ti-6Al-4V.

Chapter 2 Literature review: theoretical and experimental background

2.1 Titanium and Ti-6Al-4V

Titanium is classified as a nonferrous and light metal. This means its properties will be basically determined by the metallic bonding of atoms in the crystal lattice. Consequently, titanium possesses classic "metallic" properties, e.g., electrical conductivity, plastic deformation, increasing hardness and strength by alloying as well as the loss of ductility. Aluminum is classified as α-stabilizer because it extends the α phase field to higher β-transus temperature, and is also by far the most important alloying element of titanium. Ti-Al alloys have become the most important and most intensively investigated alloys until now.

It's generally thought that two properties, namely high specific strength and superior corrosion resistance, make titanium alloys stand out resulting in their preferential use in particular markets (Lutjering and Willaims, 2007). Since it was commercially produced by DuPont Company in 1948, titanium and titanium-based alloys have been widely used in aerospace, architecture, chemical processing, medicine, power generation, marine and offshore, sports and leisure, and transportation (Leyens and Peters, 2003).

Before focusing on the physical mechanisms of plastic deformation and how harmonic structure design method enhances the strength of materials, it's important to have a basic knowledge of the crystal structures and their role in plastic deformation.
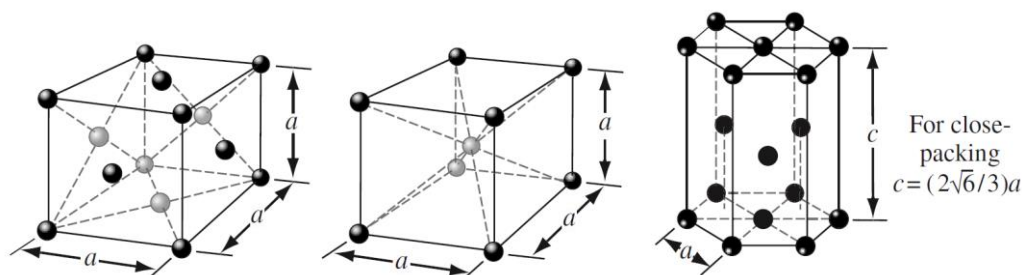
Fig. 2.1 Schematic showing the three most common crystal structures : (a) face-centered cubic; (b) body-centered cubic; (c) hexagonal close-packed (Argon, 2008).

When solidified from the melt, metals and many important non-metallic compounds are crystalline, i.e. a definite arrangement of constituent atoms is repeated periodically in three dimensions. The actual arrangement of the atoms is called crystal structure. Most of the reported crystal structures have a higher degree of symmetry

which is of great importance for the better representation of the symmetry that governs the elastic and plastic response. Three of the most common crystal structures found in metals are the face-centered cubic (FCC) lattice, the body-centered cubic (BCC) lattice, and the hexagonal close-packed (HCP) structure, as shown in Fig. 2.1.

Similar to many other metals, titanium can crystallize in different crystal structures within specific temperature ranges. At low temperatures, pure titanium crystallizes in HCP structure, called α-titanium, while at high temperatures BCC structure is stable and it's referred as β-titanium. The existence of the two different crystal structures is of crucial importance for titanium and titanium alloys since the various properties of titanium and titanium alloys are observed to be highly influenced by the corresponding microstructure (Leyens and Peters, 2003). Titanium alloy Ti-6Al-4V exhibits a kind of lamellar microstructure which is a result of simple cooling from temperatures above the β-transus temperature. When the temperature falling below the transus temperature, α nucleates at grain boundaries and then grows as lamellae into the (prior) β grain. Depending on the thermomechanical treatment, Ti-6Al-4V shows a wide variety of in microstructure. Two typical examples of attainable microstructures are the pure lamellar microstructure and the bimodal microstructure. The former is commonly generated by slow cooling from the β phase field with the lamellae becoming coarser with reduced cooling rate, as shown in Fig. 2.2a. And the bimodal microstructure usually needs to highly deform the alloy first to introduce enough cold work into the material and consists partly of equiaxed α in a lamellar α+β matrix, as shown in Fig. 2.2b.
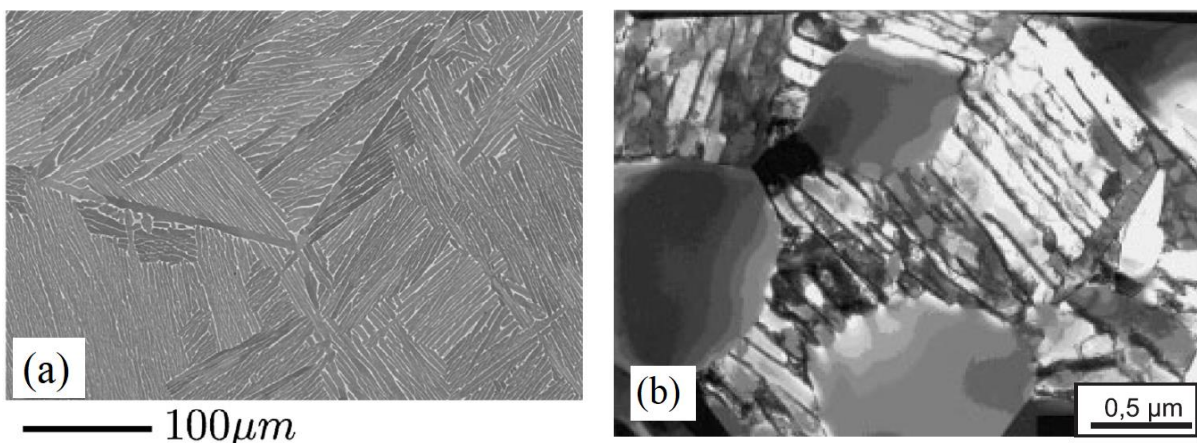
Fig. 2.2 Micrographs of the (a) pure lamellar microstructure, where darker areas are domains of α phase and lighter areas represent β phase (Kasemer et al., 2017), (b) bimodal microstructure, which is a combination of lamellar and equiaxed microstructure (Leyens and Peters, 2003).

Theoretically, a perfect crystalline solid will experience a homogeneous shear strain when loaded with a homogeneous shear stress before the ideal shear strength is approached. After that, the perfect crystalline solid becomes unstable and can deform freely to large strains when it goes through destructive shear collapse. However, real crystalline solids frequently include various lattice defects unless extremely great efforts are taken to assure perfection. In crystal plasticity, the defects of primary interest are mainly line defects such as dislocations of different types and planar defects consisting of stacking faults, grain boundaries. These lattice defects provide the physical bases for the local initiation of plastic processes which involve large local atomic displacements at these locations and usually are time-dependent (Argon, 2008). Although all lattice defects play a role in the plastic deformation of crystalline materials, it's believed that dislocations allow a highly efficient way to produce plastic shear strain and grain boundaries provide important obstacles to the dislocation motions at such sites.

2.2 Deformation mechanisms

- Plasticity and dislocations

Generally, when applying external force to the material, deformation arises accompanied by the increasing strains and proportionally rising stresses until the yield point. Before yielding, the deformation is thought to be elastic and reversible at the macroscopic scale where the material could return to its original shape once the external force is removed. However, beyond the yielding point, permanent deformation occurs which result in irreversible change of the material's shape. Extensive studies have shown that plastic deformation at ambient temperature occurs in crystalline metals mainly through dislocations, martensitic formation, and mechanical twinning. And in a wide literature dislocations are investigated as the most important lattice defects and the most effective carriers of plastic deformation (see Fig. 2.3).

- Slip planes and slip directions

As shown in Fig. 2.3b, the glide of many dislocations brings on slip which is most popular demonstration of plastic deformation in metals. It can be imagined as sliding or successive displacement of one plane of atoms over another on so-called

slip planes. As a consequence, individual chunks of crystal between two slip planes remain undistorted as shown in Fig. 2.4. Further plastic deformation arises either through more slip activity on present slip planes or through the activation of new slip planes. These dislocation movements on the slip planes allow plastic deformation to develop at much extremely lower stresses than that is needed to move all atoms on the whole slip plane. By the way, to provide a basic knowledge about the characteristic shear stress required for the slip, consider the crystal plotted in Fig. 2.4 which is subjected to tensile force F along the cylindrical axis. Assume the cross-sectional area of the cylinder is A, λ is the angle between F and the slip direction, ϕ is the angle between F and the normal to the slip plane, then it can be deduced that the shear stress τ resolved on the slip plane and in the slip direction is

$$\tau = \frac{F}{A} \cos\phi \cos\lambda \tag{2.1}$$
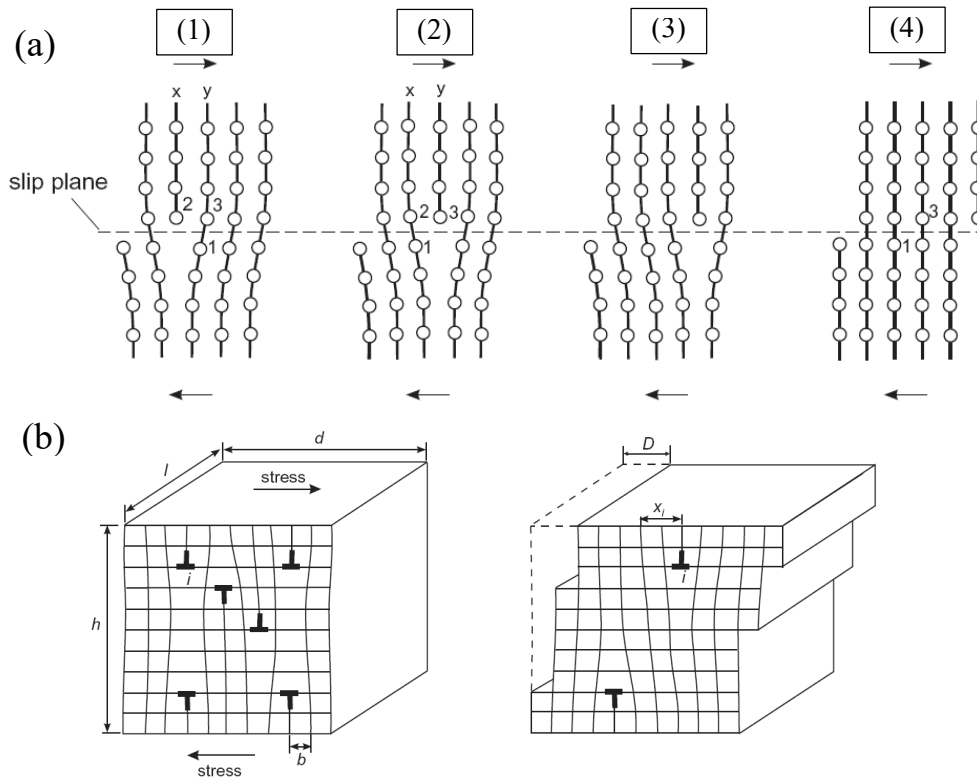
Fig. 2.3 Schematic illustrations showing (a) the effect of the movement of a single edge dislocation on crystallographic shear where the arrows indicate the applied shear stress and (b) many edge dislocations in a crystal subjected to an external resolved shear stress and the produced plastic displacement D (Hull and Bacon, 2001).

Plastic slip starts when the resolved shear stress τ for a slip system reaches a critical value τ_c called the critical resolved shear stress (CRSS). It's found that the

value of τ_c of a certain slip system is generally independent of the crystalline orientation and varies from each other in different slip systems in crystal structure such as HCP. The quantity $\cos\phi\cos\lambda$ is known as the Schmid factor.
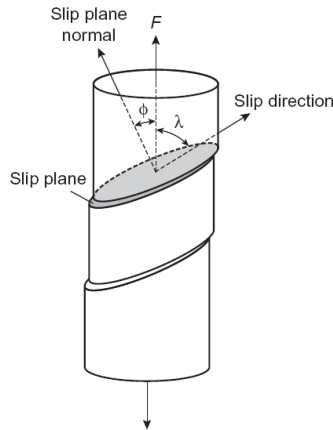
Fig. 2.4 Schematic illustration showing plastic deformation by the slip movement on slip planes in a cylindrical crystal.

- Grain boundaries and the Hall-Petch law

The grain boundaries are well known to be capable of impeding dislocation movements. The density of dislocation in a certain grain has a direct influence on the obstacles to the dislocations when traversing the gain boundaries into neighboring grains. The crystal lattice nearby the grain boundaries is usually much more disordered than that within the grain, thereby hindering the dislocations from moving in a continuous slip plane and preventing significant plasticity.

One of the main strengthening mechanisms is the grain boundary strengthening, commonly described by the Hall-Petch law, which is determined by the average grain size and the number of dislocations in a pileup (Hull and Bacon, 2001). According to the dislocation mechanics, dislocation pileups emerge when more and more dislocations move to the boundary. These dislocations produce repulsive stress fields which play a role of driving force to reduce the obstacles to diffusions across the boundary. This mechanical activity results in yielding within the neighboring grains (or micro-cracks) and brings on further deformation in the material. Experimental observations through transmission electron microscopy (Monnet et al., 2004; Castany et al., 2008) show that the decrease of grain sizes reduces the amount of possible pileup near the boundaries and in turn increases the magnitude of resolved shear stress to move a dislocation, thereby improving the yield strength. This deformation mechanism can be simply described by the Hall-Petch equation.

$$\sigma_y = \sigma_0 + \frac{k_y}{\sqrt{d}} \tag{2.2}$$

where σ_y is the yield stress, σ_0 is material constant for the resistance of the lattice to dislocation motion, k_y is strengthening coefficient, d is average grain diameter.

2.2.1 Deformation in the α phase

It's generally agreed in a wide range of literature that the dominate mechanism of plastic deformation in HCP polycrytsals under quasi-static external load is the glide of screw dislocations in the prismatic slip systems (see Fig. 2.5). It's also reported that the list of the secondary slip modes easily activated could be <a> type basal, <a> type first-order pyramidal, <c+a> type first/second-order pyramidal. Moreover, in some cases twinning cannot be neglected for pure titanium and some Ti-Al alloys in the investigation of mechanical behavior. From the viewpoint of CRSS, <c+a> type slip systems and twinning systems are much more difficult to be activated than the <a> type slip systems. Previous studies have also remarked that the difficulty of activating the <c+a> slip systems are caused by the low packing density (Numakura et al., 1986) and to facilitate the activation of the <c+a> slip systems, the ratio of critical resolved shear stress for prism and basal slip systems compared to <c+a> slip systems should be sufficiently low. However, when the direction of external loading is fixed, in certain crystalline orientations these 'harder' slip systems could play a significant role in determining the material behavior. It's worth noting that the presence of these 'harder' slip systems is important to provide sufficient degree of freedom to accommodate generalized deformation, particularly the deformation along the c-axis. Generally, these 'harder' slip systems dictate in the case that the movement of <a> type screw dislocations is largely restricted. The decrease of dislocation mobility can be caused by the fact that the crystal is subjected to parallel with the c-axis. As a direct consequence, the resolved shear stress on the slip plane of <a> type slip system is almost zero. In addition, twinning and <c+a> type slip have also been captured adjacent the grain boundaries in polycrystalline materials where their presence is important to relieve the incompatible strains during the deformation (Perilla and Sevillano, 1995).

Twinning occurs when some of the crystal lattice points of two individual crystals overlap in a symmetrical manner. The intergrowth of two individual crystals generally

exhibits many specific configurations. The surface on which the overlapping lattice points are located in crystals is called twin plane. In a twinning deformation, the displacement is more or less uniformly distributed in comparison with a step shear displacement of a crystal. The CRSS of a certain slip system can be largely increased by alloying additions due to the size misfit of atoms. And it's also agreed that the twinning is closely linked with the c/a ratio which has significant influence on the inter-planar spacing, packing densities, stacking fault energy and lattice distortions.
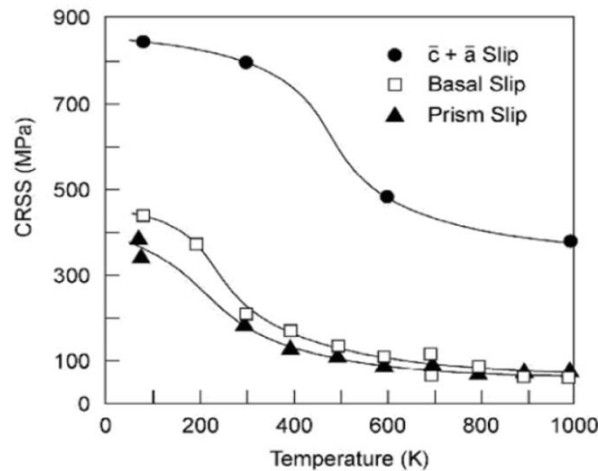
Fig. 2.5 The CRSS for the different slip systems calculated for single crystals of pure titanium (Lutjering and Willaims, 2007).

Twinning can impose significant influence on the deformation behavior and compatibility of HCP metals. The presence of multiple twinning modes in HCP structure is said to be responsible for the good ductility of some metals such as titanium and zirconium. On the other hand, some HCP metals exhibit bad ductility during deformation due to the lack of available twinning systems (Yoo, 1981). However, the twinning process in HCP is very complex to properly consider. Referring to the wide literature, a list of the reported twinning systems includes $\{10\bar{1}1\}$, $\{10\bar{1}2\}$, $\{11\bar{2}2\}$, $\{11\bar{2}4\}$, $\{11\bar{2}3\}$ and $\{11\bar{2}1\}$ (Tan et al., 1998). Fig. 2.6 is a schematic illustration showing the most frequently observed and most important twinning systems.

For titanium, the twinning systems $\{10\bar{1}2\}$ and $\{1\bar{2}11\}$ are activated by c-axis tension where the extension of crystal along the c-axis occurs, while the $\{10\bar{1}1\}$ and $\{1\bar{2}12\}$ are compression twinning systems which cause a distension of the crystal along the c-axis. It's noted that the orientation relation between the twinning shear and the internal stress of a crystal directly determines the number of independent modes which is available in a twin system (Yoo, 1981). Besides, there exist some

other aspects of twinning in HCP systems to which attentions should be paid, such as the various twinning shear with different magnitudes of each system and the ratio of the number of reallocated atoms during twinning to the number of atoms inside the unit cell of the twin. Both aspects affect the determination of which systems should be the easiest to activate. As mentioned above, the magnitude of the twinning shear is closely related to the c/a ratio. There is a general agreement that the $\{10\bar{1}1\}$ system has the lowest magnitude of twinning shear and should be the most likely system to be activated.

$$\{1\bar{2}11\} \qquad \{10\bar{1}2\} \qquad \{10\bar{1}1\} \qquad \{1\bar{2}12\}$$
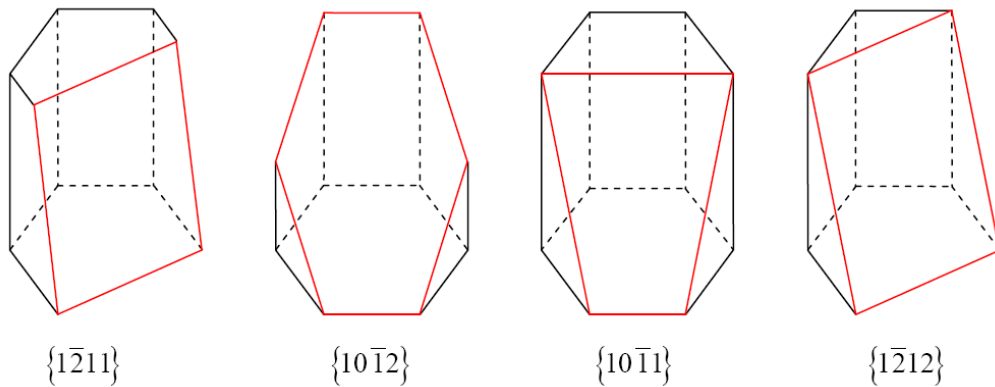
Fig. 2.6 Schematic illustration showing the most frequently observed twin habit planes in titanium (Mayeur, 2004).

To the authors' knowledge, in a wide range of literature, it's often assumed that the likelihood for twinning decreases with increasing aluminum content to the extent that twinning is rarely if ever observed in Ti-Al alloys with 6% Al (Williams et al., 2002; Lutjering and Williams, 2007; Kasemer et al., 2017; Leyens and Peters, 2003). Although twinning is observed in β phase, it's also suppressed by the alloying additions. Consequently deformation twinning is not modeled in many numerical simulations. However, it's also worth mentioning that some publications have reported that deformation twinning might be an active and important mechanism in Ti-6Al-4V for specific microstructures (e.g. an equiaxed microstructure) and/or loadings (e.g. cyclic deformation, dynamic deformation). Coghe et al. (2012) remarked that most studies reporting the suppression of deformation twins due to increased Al content only considered monotonic deformations and moderate strains and strain rates. And they investigated the importance of twinning for uniaxial compression of a Ti-6Al-4V alloy with an equiaxed microstructure and found that twinning deformation could be n more pronounced under dynamic loading conditions.

Prakasha et al. (2010) found that a significant texture change after 6% plastic deformation could only be explained by including the $\{10\bar{1}2\}$ tensile twinning as a dominant deformation mode at small levels of plasticity together with slip related grain rotation. It has also been observed that twinning has resulted in the rotation of entire grains. A general agreement concerning the effect of twinning deformation on the mechanical behavior of the Ti-6Al-4V alloy could not be achieved by far. However, considering the objectively complex multi-scale problem investigated in this thesis work, for the sake of simplicity, twinning deformation isn't modelled.

2.2.2 Deformation in the β phase

The crystalline structure of unalloyed pure titanium at room temperature is HCP. However, it will go through a phase transformation process from HCP microstructure to BCC microstructure when the temperature is elevated above 882 ºC and in turn will undergo a phase transformation process from BCC microstructure to HCP microstructure when cooling below the β transus temperature. Depending on the alloying elements, processing conditions and cooling rate, materials with all α phase, all β phase and a mixture of α and β phases can be produced. The BCC microstructure of β phase is different from the HCP which shows completely closed packed planes. There exist 12 slip systems in BCC microstructure whose close packed directions and slip directions are the {110} planes and the <111> respectively, as shown in Fig. 2.7. Owing to the presence of many easily activated slip systems in β phase compared with α phase, the β phase is usually observed to be more ductile. Moreover, the lattice of BCC is not so close packed and thus exhibits much higher diffusion rates and influences material's creep strength.
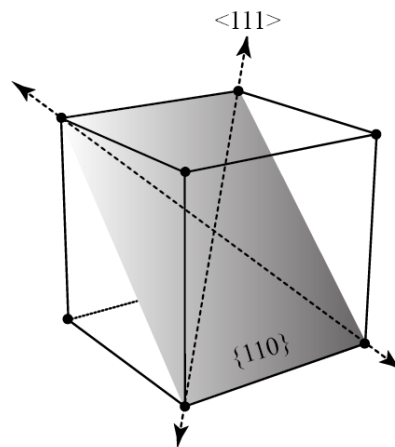
Fig. 2.7 Schematic illustration showing the slip systems in the β phase

2.2.3 Burgers orientation relationship

Once cooling below the β transus temperature, the most closely packed planes of the β phase {110} transform to the basal planes {0001} of α phase (see Fig. 2.8). According to the microstructure characterization, the distance between the basal planes in the transformed α phase is marginally bigger than the distance between the {110} planes in β phase, thus leading to a slight atomic distortion.

β phase   **β/α transformation**   **α phase**
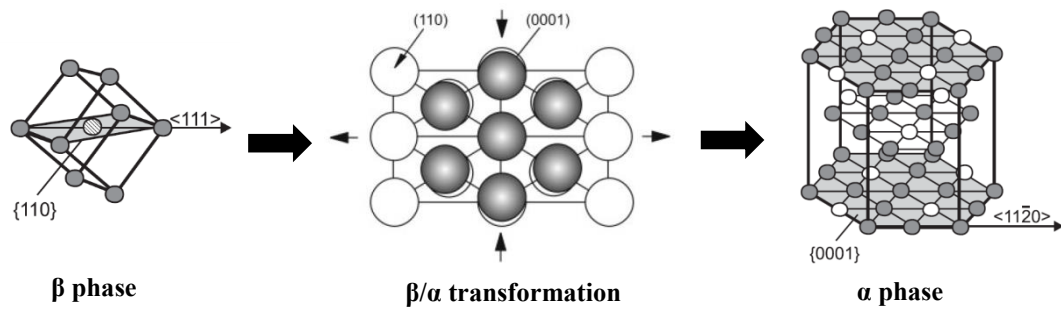
Fig. 2.8 β/α transformation according to Burgers relationship (Leyens and Peters, 2003)

After the phase transformation process, the crystallographic orientation of the α and β lamellae in lamellar α+β colonies are strictly coupled to each other obeying the Burgers orientation relationship (BOR) (Lutjering and Williams, 2007). The orientation relationship can be given by $(0\ 0\ 0\ 1)_\alpha$ // $\{110\}_\beta$ and $\langle 1\ 1\ \bar{2}\ 0\rangle_\alpha$//$\langle 111\rangle_\beta$ (see Fig. 2.9a).

The 12 $\langle 111\rangle\{110\}$ slip systems in BCC β phase and 3 $\langle 1\ 1\ \bar{2}\ 0\rangle(0\ 0\ 0\ 1)$ in HCP α phase provide 36 possible variants for the BOR in lamellar α+β colonies. However, as a first approximation of the material microstructure, only one of the variants is considered in the numerical model. This is also consistent with experimental observations that only a limited number of variants are captured in the final as-processed material (Mayeur, 2004). It's worth mentioning that the different variants of BOR directly affect the metallographic microstructure. In the prior β phases, individual α lamellar lath nucleates and grows with respect to the 36 variants of BOR. Consequently, the different possible variants generate multiple repetitions of the crystalline orientation of the lamellae which exhibits particular microstructure called basket-weave structure as shown in Fig. 2.9b.
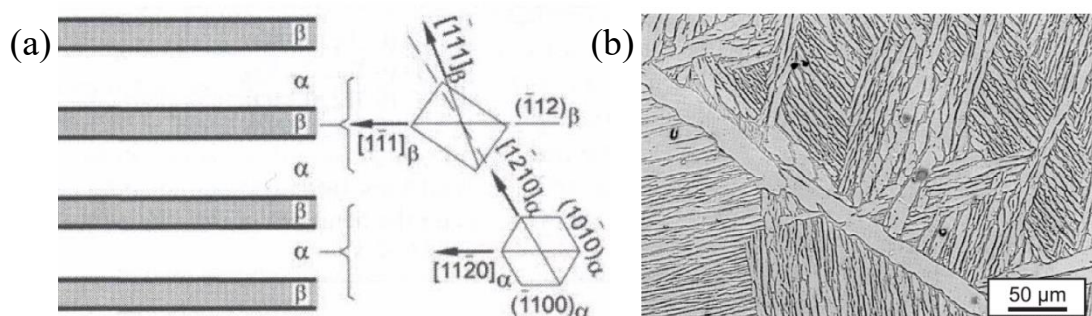
Fig. 2.9 Schematic illustrating (a) Burgers orientation relationship in lamellar α+β colonies and (b) lamellar microstructure of Ti-6Al-4V (Lutjering and Williams, 2007)

2.3 Strengthening approaches via microstructure manipulation

2.3.1 Major strengthening mechanisms

As mentioned above, dislocation motions are the most effective carriers of plastic deformation in crystalline solids. For FCC, BCC and HCP metals, the glide of dislocations in all slip systems is resisted by a lattice resistance of a certain magnitude, giving these materials a high resistance to the initiation of plasticity. Consequently, raising the plastic resistance can be effectively accomplished by elevating the resistance to dislocation motion through some strengthening mechanisms. From a mechanistic viewpoint, a dislocation mechanics view is crucial for well understanding the effectiveness of various strengthening mechanisms. Continuum plasticity approaches are believed to lack this ability both qualitatively and quantitatively.

Major strengthening mechanisms include the effect of lattice resistance, the solid-solution strengthening, the precipitation strengthening and the strengthening by strain hardening, as well as grain boundary strengthening.

The lattice resistance is generally considered from two different mechanistic viewpoints. The most important one is the glide resistance, also referred to as Peierls-Nabarro resistance, which often has different influences on edge and screw dislocations and is at very different levels in different crystal structures. The secondary one is the phonon drag which results from the interaction of a moving dislocation with lattice thermal vibrations but expected only at very high strain rate.

For solid-solution strengthening, introduction of a second constituent into a pure metal provides a very flexible means of strengthening according to the different form of the second-constituent atoms. Generally, the second-constituent atoms aggregate in various forms of increasing size, from randomly scattered individual solute atoms, through clusters of solute atom, to precipitate particles (Argon, 2008). These different forms then lead to interactions with dislocations of different levels and ranges.

For the precipitation strengthening, the precipitates and dislocations interact

through a variety of mechanisms. And these mechanisms often coexist in the same precipitate. In literatures, the interactions between dislocations and individual precipitate are usually considered in several approximations. When precipitates interact with dislocations at contact, the precipitates are sampled ideally by treating them as points in the glide plane which can be overcome once the cusp angle of the contacting dislocation arrives at a critical magnitude for shearing the precipitates. While for the case that precipitates have a size and/or modulus misfit, the interactions between the dislocations and precipitates are more diffuse and extend out of the glide plane of the dislocation.

Strengthening metals by strain hardening, also referred to as work hardening, has been used for decades. Although the basic elements and some major aspects have been well investigated and modeled, strain hardening is still a process which is at best only semi-quantitatively understood. Strain hardening is caused by the interactions of the strain fields of dislocations when the plastic deformation develops more and more. A principle problem is to understand the evolution of dislocation microstructures through experimental techniques such as microscopy and X-ray diffraction. Based on these observations, a variety of constitutive models are developed for several distinct strain hardening behaviors in metals with different crystal structures. Currently two forms of strain hardening are widely studied, interplane hardening and intraplane hardening. The former one results from the interaction of the stress fields of glide dislocations moving on parallel planes, which is investigated earlier than the other. The latter one results from interactions between dislocations and slip obstacles in their glide plane and is thought to be of central importance.

In polycrystals, grain boundaries are thought to strength the materials by playing two complementary roles in the process of deformation. First, when dislocations pass from one grain to another, grain boundaries put resistance to them; selected sets of slip systems are required to achieve compatible deformation among grain assemblies. Consequently, this results in an increase of plastic resistance which is higher than the critical resolved shear stress for pure single crystals. Generally, this fact can be analyzed by using the grain-size-independent Taylor factor which is only linked to the orientations of the investigated slip systems. However, it's observed that plastic resistance of polycrystals also depends on the grain size, with decreasing grain size resulting in increasing plastic resistance. This indicates that grain boundaries play another role in strengthening materials. A famous explanation of this strengthening

effect was proposed by Hall (1951) and Petch (1953) which is known as Hall-Petch law. It's observed that before the yield emerges some isolated slip activities are captured in some individual grains but that general yield requires percolation of slip processes among grains. Hall (1951) and Petch (1953) then proposed that this occurs when stress concentrations developed by dislocation pileups initiated in the soft grains and arrested at grain boundaries result in initiation of new slip processes in neighboring harder grains to achieve the required percolation (Argon, 2008).

2.3.2 Approaches to improved strength-ductility combination of metals

Previous researches have shown that metals like titanium, stainless steel can be processed to exhibit very high strength, but usually at the expense of severe loss of ductility (Saada and Dirras, 2009; Ma, 2006; Wang et al., 2002). Here some recent advances in overcoming this disadvantage are reviewed mainly about the application of methods using purposely deploying heterogeneous nano/micro-structures in metallic materials. Most of these structural design based on microstructure manipulation theory are currently being explored, including bimodal, harmonic, lamellar, gradient, domain-dispersed, and hierarchical nano/micro-structures. Although the underlying mechanisms of these distinct approaches have not been thoroughly understood, a design principle seems to be shared by these tactics where the designed structural heterogeneities lead to non-homogeneous plastic deformation and generate steep strain gradients, thereby boosting strain hardening and uniform tensile ductility at high flow stresses. Moreover, the distinct mechanical behaviors of individual grains resulting from these heterogeneous microstructures play a role similar to multiple phases in complex alloys such as Ti-6Al-4V sharing common material design. In this section, we will review some elementary details for several structural designs to provide a basic knowledge of novel approaches towards a synergy between high strength and high ductility. The harmonic structure design investigated in this report belongs to this category of microstructure manipulation methods.

It's currently of great interest to achieve good mechanical properties, i.e. improved strength-ductility combination, by novel microstructure manipulation methods. Recently, there have been some successful researches of new material processing routes which make the microstructural control on the nanometer and

micrometer scale possible. These new approaches start from creating heterogeneous nanostructures and microstructures in a single-phase metal, then extend to complex alloys and composites. However, from the materials science and mechanics perspectives, the study on those simpler single-phase materials can shed light on two primary questions for complex alloys and composites: (i) what kind of nano/micro-structures design in metals can push the boundary of the strength–ductility combination, and (ii) what are the new deformation mechanisms responsible for the improved strength–ductility combination in the heterogeneous nano/micro structures (Ma and Zhu, 2017).

Bimodal distribution of grains can be obtained by a thermomechanical processing route. Cryogenic rolling and secondary recrystallization are applied during which new grains grew abnormally at the expense of others to reduce surface area (Wang et al., 2002). Fig. 2.10 shows an example of bimodal grained Cu where micrometer-sized grains accounting for 25.0% volume fraction randomly distribute among ultrafine grains (<200 nm). The resulting material with bimodal grains exhibit a marked improvement in uniform elongation concurrent with pronounced strain hardening without sacrificing much of the strength. Wang et al. (2002) attributed the additional work hardening capacity of bimodal grained materials to accumulated dislocation resulting from extremely huge amounts of geometrically necessary dislocations that appear to accommodate the large strain gradient across the bimodal (ultrafine-coarse) grain boundaries.
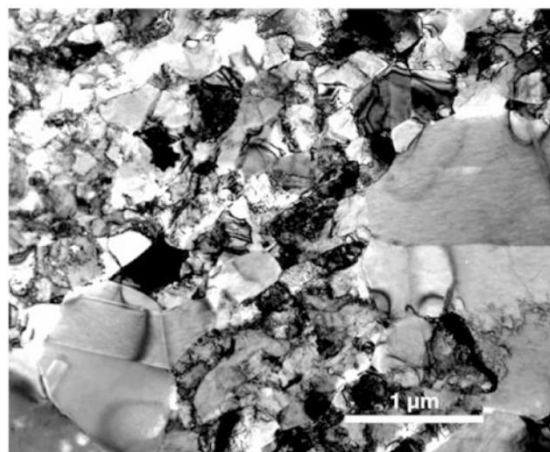
Fig. 2.10 Transmission electron microscopy (TEM) image showing an example of bimodal distribution of grains for Cu with 25% volume fraction of micrometer-sized grains randomly embedded among ultrafine grains (Wang et al., 2002).
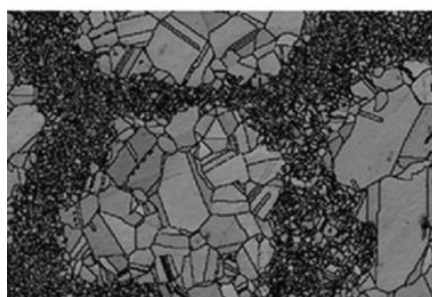
Fig. 2.11 EBSD maps showing microstructures of well-defined harmonic-structured SUS304L (Zhang et al., 2014).

Motivated by the studies on bimodal grained materials, a specific bimodal microstructure concept called "harmonic structure (HS)" was proposed by Ameyama and co-workers (Ameyama et al., 2012; Zhang et al., 2014), as shown in Fig. 2.11, which made use of a controlled non-uniform grain size refinement to delay plastic instability via improved strain hardening rate (Sekiguchi et al., 2010; Ota et al., 2015; Vajpai et al., 2015). This manufacturing process integrates the severe plastic deformation and powder metallurgy approaches. HS materials are produced by the hot consolidation of bimodal powders created by controlled surface plastic deformation, i.e. ball milling or jet milling. In HS, the heterogeneous microstructure has a specific arrangement, where the CG phase, named "core" is enclosed by an interconnected network of FG phase, named "shell". In recent years, the HS design concept has been successfully applied to processing a variety of metallic materials, such as titanium and its alloys, nickel copper, stainless steels, etc. Two good review articles are highly recommended (Vajpai et al., 2016a; Orlov and Ameyama, 2020) in which the elementary notions, basic principles, weaknesses and advantages as well as the present development status are discussed. The experimental observations available in the above-mentioned works have demonstrated an attractive combination of high strength, good ductility as well as higher fatigue resistance exhibited by HS materials.

Another derivative of bimodal grain structure is heterogeneous lamellar structure in which relatively soft micro-grained lamellae is embedded in a relatively hard ultrafine-grained lamella matrix, as shown in Fig. 2.12. The manufacturing process integrates asymmetric rolling and partial recrystallization, more details can be found in the work of Wu et al. (2015). The generated heterogeneous lamellar structured materials are reported to be as strong as their ultrafine-grained counterparts and at the same time as ductile as their conventional coarse-grained counterparts. According to

the strain partitioning analysis, it's remarked the relatively soft coarse-grained lamellae undergo much more plastic deformation than the neighboring hard ultrafine-grained regions. And accumulated geometrically necessary dislocations are observed in the soft, large grains adjacent the interfaces between the coarse grains and ultrafine-grained lamellae. An important kinematic hardening effect is noted in heterogeneous lamellar structures.
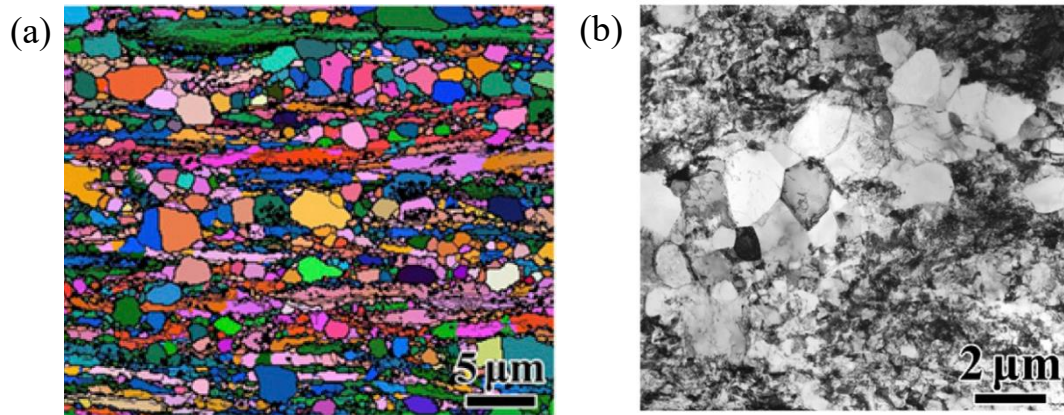
Fig. 2.5 Images showing an example of heterogeneous lamellar microstructure for Ti (Wu et al., 2015). (a) EBSD image of heterogeneous lamellar Ti after partial recrystallization. (b) Cross-sectional TEM image of recrystallized grains lamellae with two ultrafine-grained lamellae on two sides.

Another attempt of microstructure manipulation methods is the application in producing gradient grained materials where the grain size increases from nanoscale at the surface to coarse-grained scale in the core of a metal. To manufacture a gradient nano-grained layer enclosing a bulk coarse-grained core of metals, plenty of surface plastic deformation techniques have been proposed such as surface mechanical attrition treatment and surface mechanical grinding treatment (Lu et al., 2004; Li et al., 2008). A successful example of this approach can be referred to in the work of Lu (2014), as shown in Fig. 2.13. It can be seen in Fig. 2.13 that the top coating of the gradient structure is composed of nano-grains with an average grain size of about 20 nm. The grain size progressively grows to coarse grains at the micrometer scale. Generally, the resultant gradient grained materials exhibit high yield strength, extra strain hardening and good ductility. However, it should be noted that the currently used processing routes which mainly relies on various surface plastic deformation techniques limit the thickness of the gradient nano-grained layer, hence limiting the improvement of strength-ductility combination.

Microstructure diagram

Microstructure diagram
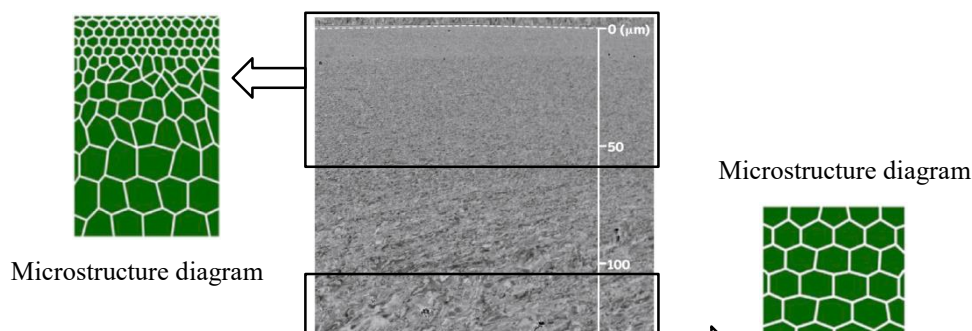
Fig. 2.13 Scanning electron microscopy image showing the gradient nano-grained copper with a gradual gradient in grain size from the surface (about 20 nm) to interior (the microscale), and schematics showing the evolution of microstructure diagram.

In addition to the above-mentioned novel processing methods involving microstructure manipulation techniques, there exist several structural designs such as dispersed nano-domains (Wu et al., 2015), hierarchically structured grains and twins (Wei et al., 2014) and phase-reversion-induced nano-grained/ultrafine-grained structure (Challa et al., 2014, 2016; Misra et al., 2010, 2015). These variations have all improved the materials' strength–ductility combination to various degrees.

2.4 Harmonic structure design

2.4.1 Theory of harmonic structure design

Strengthening of structural materials via microstructural manipulations is an efficient strategy of preparing lightweight materials with improved properties and performance. Among all the innovative methods of grain size refinement, the Severe Plastic Deformation (SPD), especially mechanical milling of powders, is an effective method to prepare fine-grained materials (Suryanarayana, 2001; Sánchez-De et al., 2010). The most commonly used bulk-SPD processes include high pressure torsion (HPT), equal channeling angular pressing (ECAP) and accumulative roll bonding (ARB), which are reported to have an advantage that the materials retain almost the same shape after processing (Horita et al., 1996, 1998; Segal, 1995; Saito et al., 1998). Besides, there also exists SPD-powder metallurgy (PM) processes such as mechanical milling (MM) and alloying milling (AM), which could be easily transferred to the conventional PM process. However, these bulk materials with "homogeneous" ultrafine-grained (UFG) and nano-grained (NG) microstructures, as shown in Fig. 2.14a, exhibit extremely high strength as compared to their coarse-grained (CG)

41

counterparts. However, these homogeneous UFG/NG materials suffer from the problem of extremely poor ductility, causing failure at small strains (Sauvage et al., 2012; Wei et al., 2004; Koch, 2003).
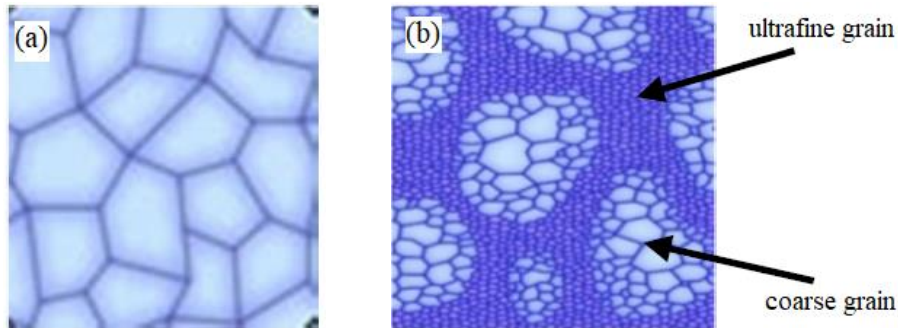
Fig. 2.14 A schematic illustrating (a) the coarse-grained structure design and (b) the harmonic structure design (Ameyama et al., 2012).

In order to obtain improved strength-ductility combination, which is an important property for gauging the enhanced performance in structural materials, a promising approach has been proposed to use a non-uniform grain size distribution, called "harmonic structure", to delay plastic instability and to improve strain hardening (Sekiguchi et al., 2010; Sawangrat et al., 2014; Zhang et al., 2014, 2015; Ota et al., 2015; Vajpai et al., 2015). It is essentially a bimodal microstructure in which deliberately introduced structural heterogeneity has a specific order: interconnected network of ultra-fine grained (UFG) regions, called "shell area", and coarse-grained regions called "core area", as shown in Fig. 2.14b. By controlling the grain size distribution, the volume fraction and the spatial arrangement of UFG parts, optimal harmonic structure can be obtained for maximal strengthening with minimal compromise of the ductility (Joshi et al., 2006).
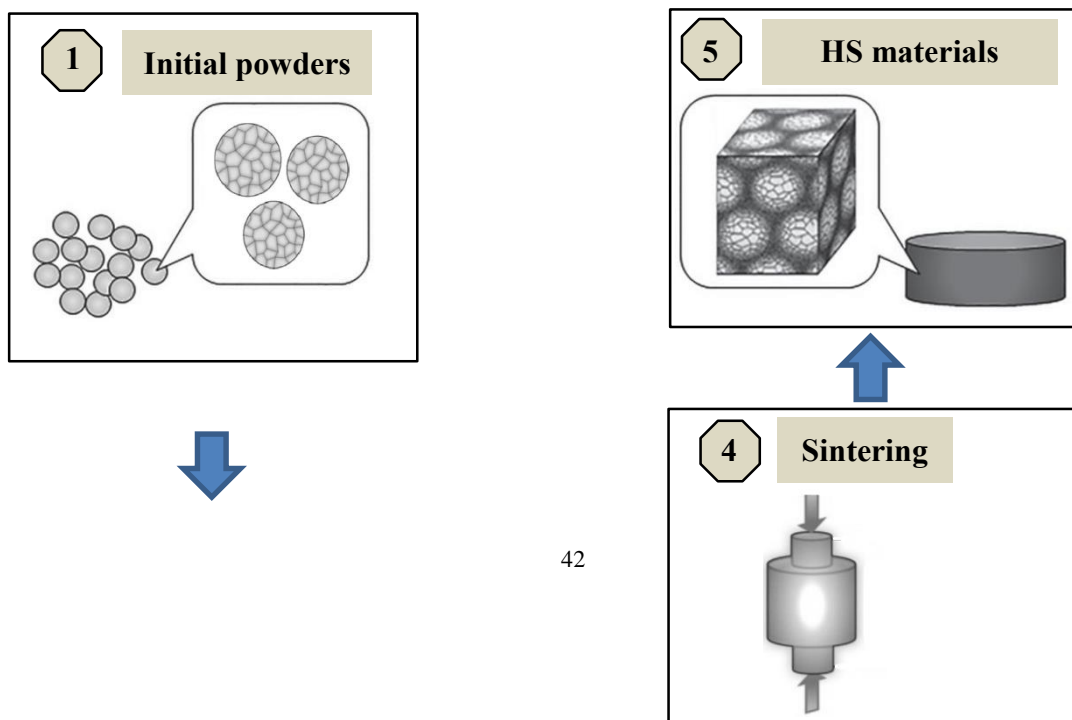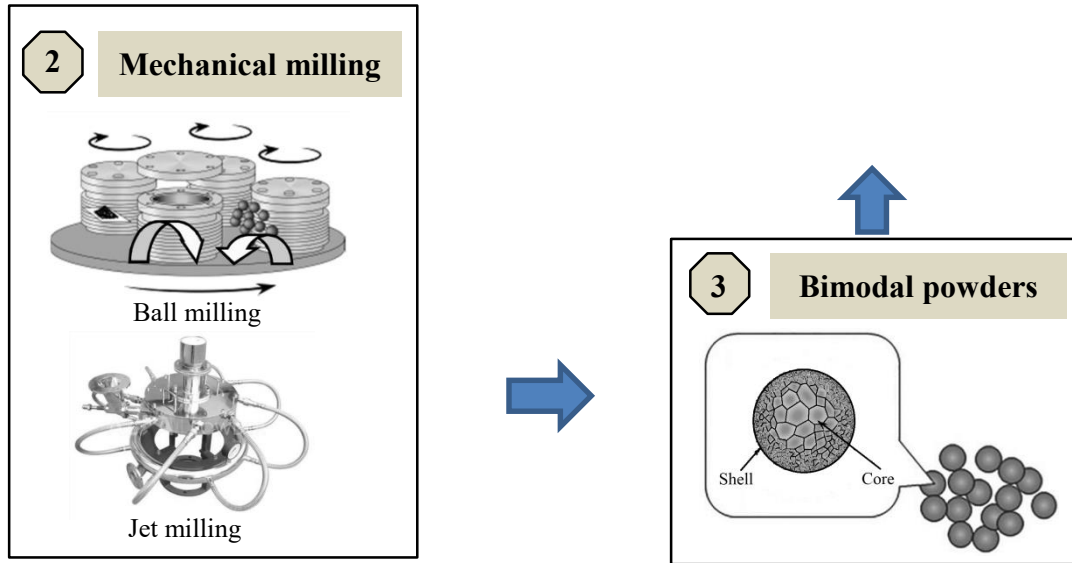
Fig. 2.15 Schematic diagrams illustrating the proposed powder metallurgy processing to prepare materials with harmonic structure design.

A thorough experimental investigation into the materials with harmonic microstructure has been carried out by researchers in the LSPM (Laboratoire des Sciences des Procédés et des Matériaux) laboratory at the Université Sorbonne Paris Nord (Ramtani et al., 2010; Hocini, 2017; Ueda et al., 2018; Mompiou et al., 2018). These work is part of the ANR project entitled HighS-Ti "High Strength Ti-based alloys with harmonic structure: Processing, Mechanical properties and Modeling" whose objective is to design and improve the harmonic microstructure by means of powder metallurgy. This project is carried out in collaboration with several scientific partners, l'Institut P' de Poitiers, l'Institut Jean Lamour (IJL) in Nancy, Centre d'Élaboration de Matériaux et d'Études Structurales (CEMES) in Toulouse and the Ritsumeikan University in Kyoto. Moreover, this project is in line with the previous ANR MIMIC "Methods in Engineering of multi-scale microstructures of metal types: Mechanical Properties and Micromechanical Modeling" piloted by the LSPM during which a certain expertise was obtained in the development and the control of bimodal structures. In this project, researchers have implemented a new concept combining severe plastic deformation (by grinding micrometric powders) and flash sintering to design massive materials having a so-called harmonic microstructure. The long-term goal of these investigations is to optimize the harmonic structure. They compared the harmonic structure to the conventional mono-modal structure in order to identify the effect of the harmonic microstructure on the macroscopic mechanical properties of the

materials thus revealing the underlying micromechanical mechanisms.

The manufacturing protocol to produce harmonic structured materials can be found in the work of Vajpai et al. (2016b). Here the procedures are detailed to provide a basic knowledge of this novel powder metallurgy processing to prepare materials with harmonic structure design. Main processing procedures are summarized in the following diagrams (in Fig. 2.15).

Two key ingredients are involved in the processing procedure to produce harmonic structured materials. First, deformed powder particles with bimodal grain size distribution, as shown in Fig. 2.15 (step 3), are obtained through controlled severe plastic deformation. Mechanical milling such as ball milling or jet milling, as shown in Fig. 2.15 (step 2), are generally used to achieve the desired plastic deformation in the metallic powders. It's worth mentioning that the option of mechanical milling approach mainly depends on the overall consideration of the size of powder particles, the chemical reactivity, permissible level of contamination from milling media with respect to specific materials, and ductility and nature of strain hardening behavior of the material being milled (Vajpai et al., 2016b). Then sintering procedure with particular consolidation conditions is applied to the deformed powder particles to generate bulk materials with harmonic structure, as shown in Fig. 2.15 (steps 4 and 5).
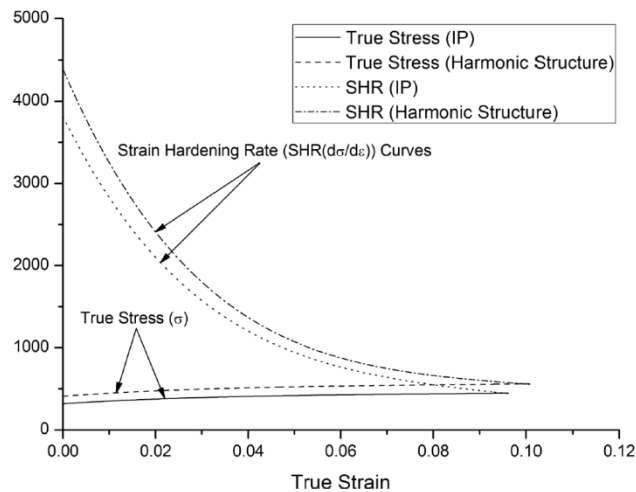
Fig. 2.16 True stress-strain curves, together with their corresponding strain hardening rate curves of the pure Titanium samples with harmonic microstructure and homogeneous coarse-grained microstructure under pure tension (Vajpai et al., 2016b).

An interesting observation with respect to the difference between homogeneous coarse-grained materials and harmonic structured materials is presented in the work

(Vajpai et al., 2016b), which may reveal some explanation of the superior properties of harmonic structured materials. As depicted in Fig. 2.16, for homogeneous coarse-grained pure titanium and harmonic structured pure titanium, the strain hardening rate generally decreases rather quickly during the early stage of deformation as the true strain increases gradually. Then it's followed by a quite small amount of decrease of strain hardening rate until the strain hardening rate curves intersect with each other at the point of plastic instability, i.e., $d_\sigma/d_\varepsilon = \sigma$. On one hand, it can be observed that homogeneous coarse-grained pure titanium and harmonic structured pure titanium show more or less similar overall macroscopic deformation behavior. On the other hand, it can be noticed that the application of harmonic structure design extends the range of uniform plastic deformation to higher level, thus delaying the plastic instability and improving the strain hardening.

A deep insight into the deformation mechanisms of harmonic structured materials is presented in the work of Park et al. (2018) where micro-digital image correlation (micro-DIC) is used to observe strain distribution in harmonic structured 304L stainless steel during deformation. The experimental observation shows that the high stress areas mainly concentrate in the relatively hard ultrafine-grained regions while the soft coarse-grained regions carry higher strain, which is consistent with the general deformation mechanisms of bimodal materials with hard/soft phases. The DIC results particularly indicate the significant strain partitioning along the boundaries between ultrafine-grained regions and coarse-grained regions. And strain peaks are also observed near the boundaries. Based on the observations, the authors conclude that the high heterogeneity exhibited by the harmonic structured microstructure generate plenty of geometrically necessary dislocations (GNDs) to accommodate the plastic incompatibility. Moreover, more GNDs are commonly concentrated at the grain boundaries.

2.4.2 Current applications of harmonic structure design

In this section, we will summarize the results of microstructure characterizations and microstructure-related experimental observations of typical metals to which the harmonic structure design has been successfully applied. This purpose of this section is to highlight the significant influence of microstructure heterogeneities introduced by harmonic structure design on the mechanical properties of metals. This is also an

important support to the constitutive models developed in this thesis work.
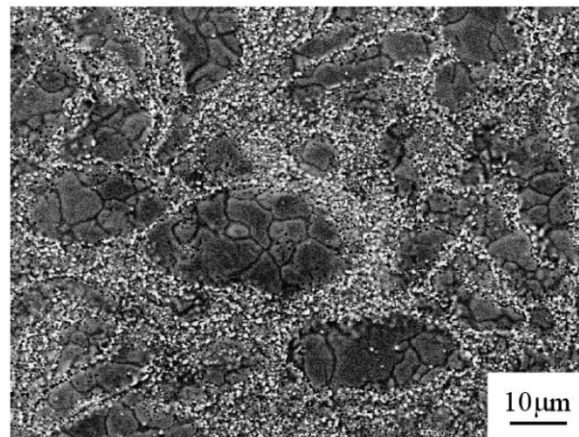
Fig. 2.17 SEM micrograph of SUS316L HRS compact with harmonic microstructures consisting of coarse-grained regions and fine-grained regions (Fujiwara et al., 2010).

Stainless steel is one of the earliest metals which are successfully processed to exhibit harmonic microstructures. Fujiwara et al. (2010) applied hot roll sintering (HRS) process to mechanically milled austenitic stainless steel powders and produced HRS materials with bimodal microstructure consisting of coarse-grained regions and fine-grained regions (Fig. 2.17). Here the powders which were mechanically milled for 10 hours were consolidated by HRS process, and then were heat-treated at 1173 K for 1 hour. It can be seen in the figure that the fine-grained regions (white areas) forms a network of nano-grains surrounding the coarse-grained regions (dark areas) consisting of meso-grains. This bimodal microstructure was called "Nano / Meso Harmonic Microstructure". It's reported that the volume fraction of fine-grained regions can be controlled by milling time, i.e., the fine-grained regions expand with milling time increasing. Moreover, the fine-grained regions are of austenite + sigma duplex microstructure and are composed of grains whose sizes are less than 1μm. And coarse-grained regions consist of austenite grains of several microns.

To have an overall view about the mechanical performance of harmonic structured austenitic stainless steel, tensile tests are carried out for compacts with various post heat treatments, as shown in Fig. 2.18, in comparison with the experimental result of the 90% cold rolled and heat treated bulk material (represented as 90% C.R. HT-773K, 2 hours). The figure shows that the HRS compact produced from powders milled for 10 hours (represented as MM 36ks) exhibit almost the same tensile strength but much better uniform elongation capacity. By fixing the mechanically milling time, it's observed that annealing plays an important role in the

mechanical properties, that is to say, increasing the annealing temperature and time results in larger grains in coarse-grained regions and less volume fraction of fine-grained regions. Consequently, the tensile strengths of HRS compacts decrease when increasing the annealing temperature and the elongation capacity is improved remarkably.
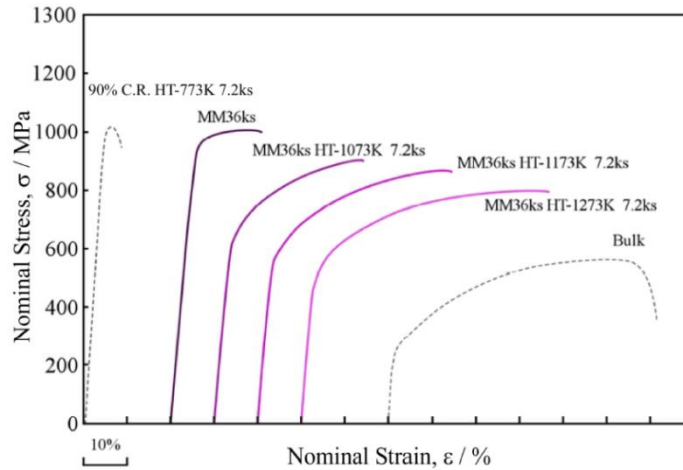
Fig. 2.18 Nominal stress-strain curves of the HRS compacts with various post heat treatments in comparison with the experimental result of the 90% cold rolled and heat treated bulk material (Fujiwara et al., 2010).
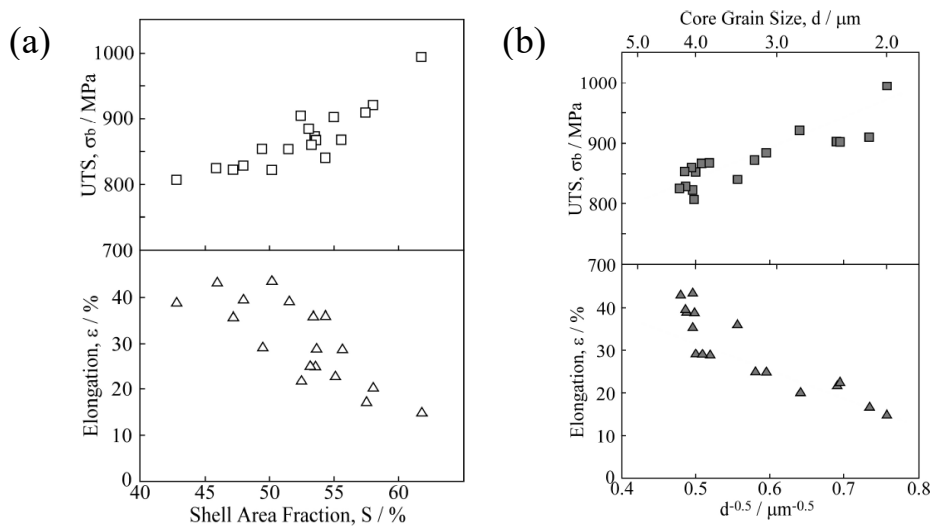
Fig. 2.19 Relationship between (a) the volume fraction of fine-grained regions and (b) grain sizes of coarse-grained regions and the ultimate tensile strength and elongation, respectively (Fujiwara et al., 2010).

Additionally, it's worth mentioning the interesting observations between the mechanical properties and microstructure features concerning the HRS austenitic stainless steel. It's found that microstructure features such as volume fraction of fine-grained regions and grain sizes of coarse-grained regions can be changed by

mechanical milling time and annealing conditions. Fig. 2.19a shows that increasing the volume fraction of fine-grained regions leads to the increase of ultimate tensile stress (UTS) and meanwhile the decrease of elongation. And Fig. 2.19b shows that increasing the grain sizes of coarse-grained regions results in the decrease of UTS and the increase of elongation. The correlation between UTS and core grain size follows the Hall-Petch relation. It's sound to remark that the harmonic microstructure has significant influence on the mechanical properties of the austenitic stainless steel.
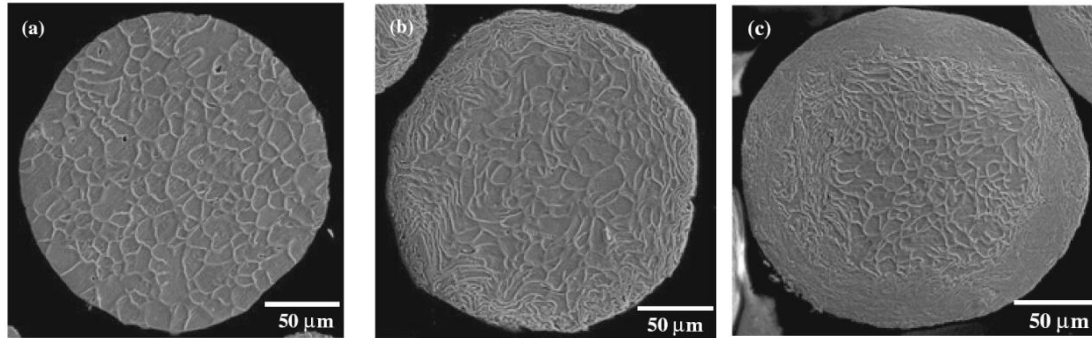
Fig. 2.20 SEM micrographs showing the microstructures of (a) as-received powder, and powders milled for (b) 15 hours and (c) 20 hours for commercially pure copper (Sawangrat et al., 2014).

Afterwards, similar researches about the application of harmonic structure design to SUS329J1 two-phase stainless steel (Ota et al., 2013), SUS304L stainless steel (Zhang et al., 2014), SUS316L stainless steel (Zhang et al., 2016, 2017) have been carried out to provide us overall understanding about the advantages of harmonic structure design and its potential in industries. Even though these studies have shown different focus and various achievements based on their experimental observations, the main characteristics of the microstructure, the improvement of strength- ductility combination and the microstructure-property relationships share many similarities described above.

Another successful implementation of harmonic structure design is the production of harmonic structured copper. The purpose is the same as in the above mentioned study of harmonic structured stainless steel, achieving better strength-ductility combination. In addition to the different conditions of mechanical milling and sintering processes which is originally dependent on the materials, the advantages of harmonic structure design are observed in the experimental results for commercially pure copper (Sawangrat et al., 2014; Orlov et al., 2013). However, it's worth noting that some interesting observations are reported in these studies. As shown in Fig. 2.20, after the mechanical milling process the heavily deformed powder

particles reveal gradient microstructures where grains in the center are equiaxed and grains within the boundary area exhibit significant ultra-refined microstructures. Moreover, the thickness of regions consisting of ultra-refined grains increases with the mechanical milling time becoming longer, as can be noticed in Fig. 2.20b, c. These observations confirm that mechanical milling process generate highly localized plastic deformation at the boundary of copper powder particles. Consequently, the harmonic structured compacts prepared from powder particles with longer mechanical milling time consist of fine-grained regions of larger thickness compared with those compacts prepared from powder particles with relatively shorter mechanical milling time, as shown in Fig. 2.21. The similar features are also found in some other materials and can be thought as general characteristics of harmonic structured materials. Since the mechanical properties of harmonic structured materials are believed to be closely linked with the microstructure features, the relationship between the mechanical milling time, the thickness of fine-grained regions and the resultant properties play an important role in optimizing the microstructure design and should be seriously considered in the simulations concerning the harmonic structured materials.
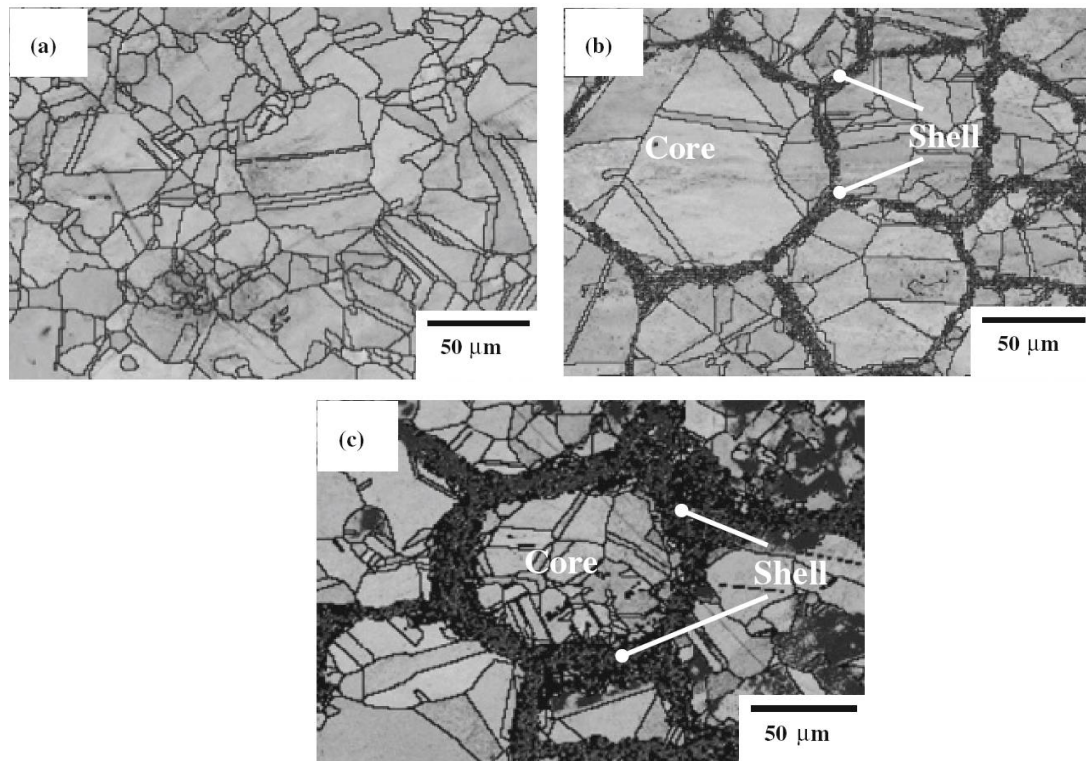
Fig. 2.21 EBSD image quality maps overlaid with grain boundaries for commercially pure copper compacts prepared from the (a) initial powder, and powders milled for (b) 15 hours and (c) 20 hours

which can be found in Fig. 2.13 (Sawangrat et al., 2014).
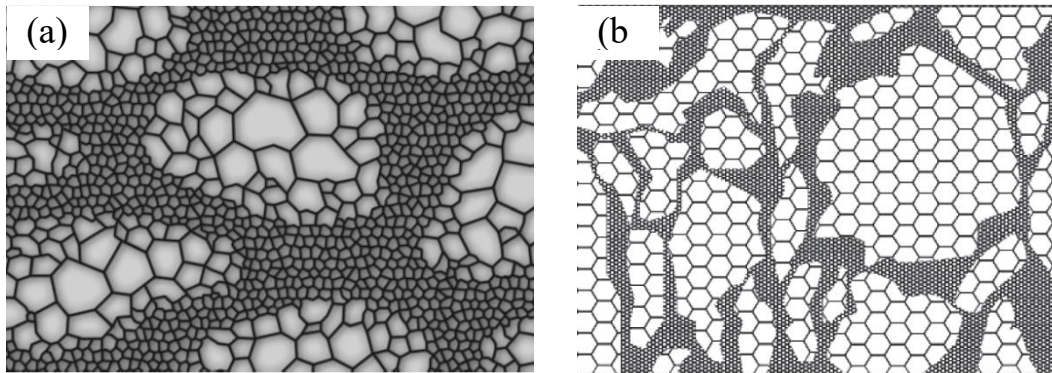
Fig. 2.22 Schematic illustrations of the microstructures for (a) harmonic structured commercially pure titanium (Sekiguchi et al., 2010) and (b) copper (Orlov et al., 2013).

It's also worth mentioning that except the 'strong' harmonic structure observed in the resultant materials where the fine-grained regions are three dimensionally interconnected and the coarse-grained regions are generally convex and embedded with the continuous network of fine-grained regions (as shown in Fig. 2.22a), there exist 'weak' harmonic structures where the fine-grained regions remain to be three dimensionally interconnected while the shape of coarse-grained regions may be irregular and concave (as shown in Fig. 2.22b). There is a general agreement that the microstructure features of the fine-grained regions and coarse-grained regions have significant influence on the mechanical properties of harmonic structured materials. However, from the experimental perspective how the above-mentioned 'strong' and 'weak' harmonic structure could affect the material properties has never been included in the studies. And in the numerical works the representative of the harmonic structures using finite element meshes mainly tackles the 'strong' harmonic structure and its effect on the results is usually underlying and mixed with other effects such as grain size effect.

2.5 Plasticity models at different scales

Investigating the deformation mechanism of materials under different external loading conditions with the help of constitutive models is crucial to their application in industries. Therefore, it's meaningful to review the major mechanisms and numerical models studying the mechanical behavior at various length scales in literature before developing an effective numerical method for harmonic structured materials. In this section, a basic knowledge of some macroscopic and microscopic

constitutive models will be briefly summarized to provide an overall understanding about which kind of model is proper in describing the mechanical behavior of harmonic structured materials.

Macroscopic plasticity

Macroscopic plasticity theory is developed mainly on the basis of experimental observations of ductile materials, thus being phenomenological. Referring to a typical stress/strain curve of a material, the main assumptions can be summarized as follows.

The material is usually assumed to be homogenous and isotropic at each continuum point. In particular cases, the anisotropy can be considered by means of certain extension of typical plasticity theory. After the yield stress is reached, materials undergo plastic deformation where an irreversible deformation process emerges, i.e. there exists macroscopic permanent deformation even external loads are completely removed. Equations which describe the relationship between macroscopic stress/strain are main ingredient of the plasticity theory, such as the yield criteria defining the initial yield surface, the flow rule describing the evolution of macroscopic stress as a function of the overall strain and the hardening rule estimating the evolution of yield surface.

Strain gradient plasticity

Even at the macroscopic scale, size effect is frequently observed in wide experiments, such as the Hall-Petch effect (Hall, 1951) and the indentation size effect (Poole et al., 1996; Ma and Clarke, 1995). However, the typical plasticity theory and crystal plasticity theory without the introduction of length scale variables are incapable of considering the size effect properly and effectively. To solve this problem, strain gradient plasticity (SGP) was proposed in the work of (Fleck et al., 1994) which was based on the research work concerning the higher order continuum elasticity and dislocation mechanics.

In the framework of SGP, it's assumed that plastic flow is influenced by both the strain itself and the strain gradient. From the perspective of dislocation mechanics, strain and strain gradient is related to statistically stored dislocations (SSD) and geometry necessary dislocations (GND). During the past decades, the strain gradient plasticity has shown its good performance in wide topics involving the length scale effect on the strength of polycrystalline materials (Smyshlyaev and Fleck, 1996), the behavior of shear bonds (Sluys and Estrin, 2000) and crack propagation (Wei and

Hutchinson, 1997) and the grain boundary effect in polycrystals (Shu et al., 2001).

Although it has properly introduced the size effect into the conventional continuum plasticity, the drawback of strain gradient plasticity is also evident. The SGP fails to simulate the size effect in cases where strain gradient is missing, for example the size effect presented in the uniaxial tension test (Balint et al., 2006). This is caused by the fact that in the strain gradient plasticity theory no dislocation activities is involved and the dislocation density alone is incapable of describing the dislocation activities of polycrystalline materials.

Discrete dislocation plasticity

The discovery of dislocations and their activities have led to the development of dislocation mechanics 1930's. The dislocation theory is then frequently employed in the investigation of mechanical behavior of metallic materials, particularly the plasticity. As mentioned above, dislocations are widely regarded as the carrier of plastic deformation of metallic materials. According to the dislocation mechanics, dislocations will glide on a slip plane at a certain velocity when the local stress reaches a critical value to overcome the lattice resistance to initiate the dislocation motion. Therefore, plastic flow can be understood as the overall motion of plenty of dislocations which lead to the irreversible change of material shape. Moreover, it's reported that the interaction between dislocations and the interaction between the dislocations and obstacles closely hinder the dislocation motion. This in turn evokes the pile-up of dislocations and an improvement of critical stress to initiate plastic deformation, such as the straining hardening.

With the further understanding of the role of discrete dislocations in the performance of ductile materials, some attempts to propose a practical discrete dislocation plasticity model have been carried out in recent years. Early development of discrete dislocation plasticity can be found in the work of Brown (1964) and Bacon (1967) where the deformation is assumed to be only caused by edge dislocations. Due to the large development of computational technique and the improvement of dislocation theory, the numerical application of dislocation dynamics is able to describe the details of dislocation activities at the expense of acceptable computation cost. Lubarda et al. (1993) and Vandergiessen et al. (1995) developed a classical 2D framework to solve the boundary condition problem where the collective motion of discrete dislocations was simulated to describe the plastic flow. And Kubin et al.

(1992) developed 3D numerical simulation framework for discrete dislocation plasticity. Currently, the modelling of 3D dislocation dynamics is mainly fulfilled by two methods, i.e. the approach using line discretization (Madec et al., 2000)and the approach using representation of a curved dislocation segment (Groh, 2009). And most of previous works dealt with isotropic continuum solid, few studied the elastic anisotropy (Rhee et al., 2001).

The application of discrete dislocation plasticity in solving boundary value problems in literature is generally carried out by using the superposition method developed by Vandergiessen et al. (1995). The non-exhaustive list of recent applications of this framework includes uniaxial tension test of single crystal and polycrystalline samples (Balint et al., 2006), the investigation of bending plasticity (Cleveringa et al., 1999), the influence of grain size on the polycrystalline materials' strength (Balint et al., 2005). Besides, discrete dislocation plasticity was also employed in the study of indentation size effect. Generally speaking, the discrete dislocation plasticity theory is capable of simulating the highly localized stress/strain fields in the investigated samples. Its advantage over strain gradient plasticity is that the discrete dislocation plasticity theory is able to describe the size effect when the strain gradient is absent in materials. Furthermore, it's also widely used in the simulations concerning micro-bending, nano-indentation and nano-sliding, etc.

Crystal plasticity

The crystal plasticity theory is based on a basic understanding of the material behavior that the plastic deformation of metallic materials is heavily influenced by their crystal structure. This understanding as well as a plenty of experimental observations have motivated the development of crystal plasticity theory and its application in predicting the material behavior. However, earliest efforts were mainly made to simulate the anisotropy of plastic deformation where the interaction between individual grains and complex boundary value problem were out of the reach (Taylor, 1938; Kroner, 1961). Those early approaches carried out the study of crystal plasticity by imposing different simplified assumptions on the strain or stress variable within the grains, thus being incapable of simulating the real metallic materials. With the advent of finite element method and robust algorithms, the crystal plasticity theory reveals its good ability of solving complex problems. More details about crystal plasticity will be presented in the following sections since it's the main ingredient of

the numerical model in this thesis.

The observation of material anisotropy is widely reported revealing the relationship between the mechanical property and the microstructure, which is the key issue solved by the crystal plasticity. The mechanical responses could be different when the material is subjected to external load with different direction. Yield surface shifts as a result of the anisotropy of the material, where the three components of macroscopic stress exhibit discrepancy during the strain hardening. Such experimental observation enlightens researches to formulate the crystal plasticity theory in which the plastic deformation mechanism is traced back to the influence of microstructure features of a material at the microscopic scale. Microstructure texture and its evolution are then taken into consideration to describe the anisotropy of a material by integrating the deformation of individual grains and their interactions with neighboring grains. Consequently, this topic inspired the researchers to develop crystal plasticity finite element modeling (CPFEM) method to simulate the macroscopic plasticity of crystalline materials by incorporating the crystallographic and anisotropic features as well as the role of microstructure under certain boundary conditions.

Multi-scale plasticity

The term 'multi-scale' indicates the incorporation of constitutive models which are defined at different length scales. The most popular need for multi-scale methods exists in those issues where constitutive models at a single length scale may reach their limits. A well-known application is the incorporation of dislocation interactions obtained from discrete dislocation dynamic simulations with dislocation density-based constitutive laws in the CPFEM (Arsenlis and Tang, 2003). However, the direct use of simulation data achieved from atomic-scale simulations is still challenging for the reason that there exist a large discrepancy in space and time scale between atomic-scale and the crystal scale (Roters et al., 2010). In this thesis, our multi-scale modelling integrates the constitutive models at the microscopic scale and the mesoscopic scale as well as the macroscopic scale, thus avoiding the above mentioned discrepancy theoretically. But it has to be remarked that the lack of integration of atomic-scale simulations into the multi-scale modelling makes the multi-scale model phenomenological, not very physics-based. This will be improved in the future work.

Atomistic	Discrete Dislocations Plasticity	Dislocation Patterns	Crystal Plasticity	Macroscale Plasticity
$O(10^{-10}m)$	$O(10^{-8}m)$	$O(10^{-7}m)$	$O(10^{-6}m)$	$O(10^{-3}m)$
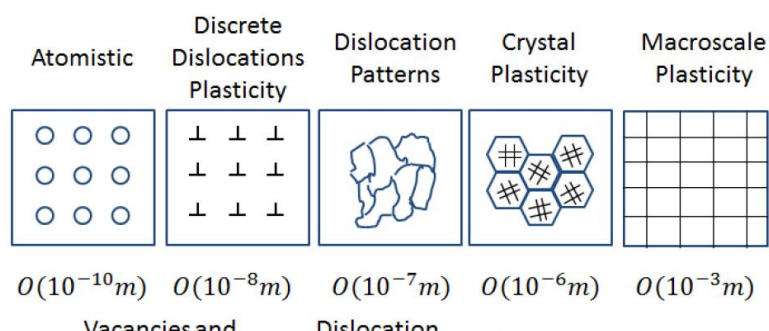
Fig. 2.23 The hierarchy of length scales in multi-scale plasticity ranging from atoms to macroscale (Xu, 2015).

The main object of multi-scale plasticity is to solve mechanic problems of polycrystalline materials where the investigated mechanical behaviors occur and develop at different scale. And the establishment of the multi-scale plasticity has to be based on the understanding of material behavior at different scales. For example, when studying the deformation and failure of ductile polycrystals, the strength and deformability of materials are influenced by crystal defects (vacancies and impurities), line defects, planar defects (grain boundaries, interfaces) and volume defects (precipitates) together. Consequently, a comprehensive constitutive modelling framework should include the deformation mechanisms covering the atomic length scale, the crystal length scale, mesoscopic scale and macroscopic scale. Fig. 2.23 shows an example which carries out the modelling at different length scales from automatic scale to macroscale.

In general, multi-scale modelling makes use of either unidirectional or bidirectional modelling strategies to pass information (or results) between different length scales. The former one only delivers information from a lower length scale to a higher length scale. For example, in the work of Shilkrot et al. (2002), a multi-scale modelling has incorporated the atomistic scale and the mesoscopic (continuum) scale in which all the elastic constants, thermal expansion coefficients and crystal parameters are calculated from the atomistic scale model and then used as input data of constitutive models at the mesoscopic scale. Generally speaking, multi-scale modelling using unidirectional strategy to pass information has the advantage of easy implementation and efficient computation because the models at the lower length scale don't require the feedback computation results from the models at the higher length scale. However, it has to be noted that this multi-scale modelling shows limited capability of describing complex mechanical phenomenon (Curtin and Miller, 2003), since it only regards the lower length scale models as 'parameter providers' and the

mechanical behavior has usually to be simplified in this case.

As a comparison, the multi-scale modelling using bidirectional modelling strategy to pass information provides more realistic and comprehensive description of the interaction between mechanical behaviors at different length scales. During the past decades, this multi-scale modeling has been widely used in the topics such as the coupling of electronic structure and atomistic modelling (Pettifor et al., 2002), the coupling of atomistic to discrete dislocation dynamics (Shilkrot et al., 2004) as well as the coupling of atomistic to continuum. In thesis, for the sake of simplicity and efficiency within the three-dimensional CPFEM, only the multi-scale modeling using unidirectional strategy to pass information from the low length scale (micro-scale) to higher length scale (macro-scale) is employed.

Chapter 3 Experiments: deformation behavior of CP-Ti and Ti-6Al-4V

In this chapter, we present briefly the experimental data used in numerical simulations. These experimental results serve as indispensable database for all the numerical studies throughout the thesis work. There are totally three sets of mechanical tests as well as the corresponding microstructure characterizations employed in particular numerical simulations.

3.1 Tensile tests on Ti-6Al-4V with conventional structure

3.1.1 Material and tensile test

There are two crystallographic phases present in the investigated Ti-6Al-4V, viz. the α phase showing hexagonal close packed crystal symmetry and a secondary β phase displaying body centered cubic crystal symmetry. These two phases are experimentally observed to have volume fractions of approximately 93% and 7%, respectively. The bimodal microstructure of α-β Ti-6Al-4V is characterized by transformed β colonies consisting of alternating α and β lamellae and equiaxed α grain. Fig. 3.1 shows the micrograph of the bimodal microstructure. The microstructural morphology was measured from images obtained by using scanning electron microscopy (SEM) and EBSD techniques. Morphological data concerning key microstructural features are given in Table 3.1.
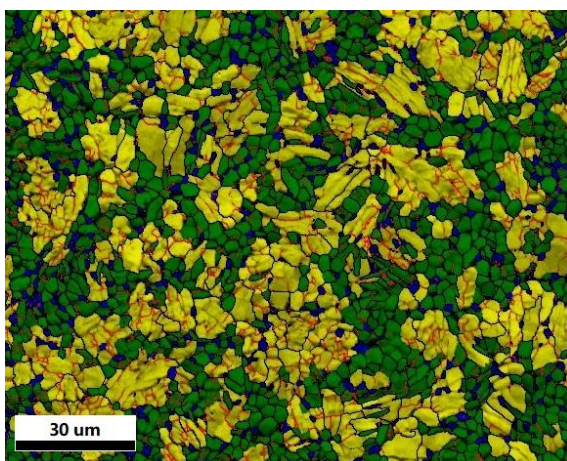
Fig. 3.1 A micrograph of bimodal α-β Ti-6Al-4V. Yellow regions represent lamellar α+β colonies, and other regions represent equiaxed α grains. The microstructure characterization is part of the ANR project entitled HighS-Ti "High Strength Ti-based alloys with harmonic structure: Processing, Mechanical properties and Modeling".

Tensile test specimens were prepared to evaluate the material's yield strength by

performing mechanical test with an MTS M20 machine. The sample had a gauge length, width and thickness of 3mm, 1mm and 1mm. Tensile test was conducted monotonically at an engineering strain rate of 0.0056 s^{-1}. Yield strength was determined by the 0.1% offset method from the engineering stress-strain curve. Fig. 3.2 shows the experimental stress-strain curve for the investigated bimodal α-β Ti-6Al-4V. The sample exhibits yield strength of 973.2 MPa.
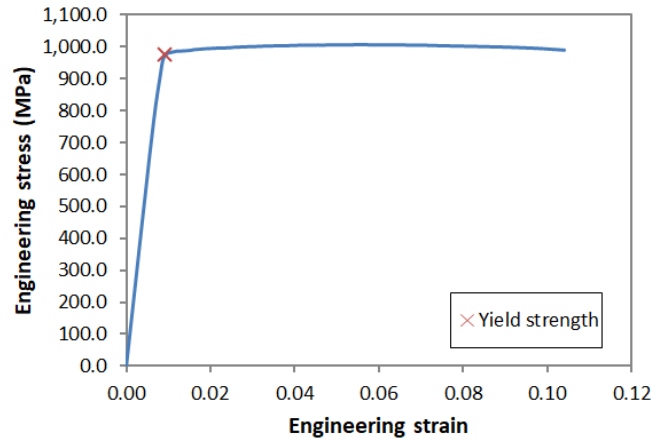
Fig. 3.2 Experimental stress-strain curve for the bimodal α-β Ti-6Al-4V under tensile loading

Table 3.1

Microstructural morphological data

Parameter	Value	Description
D	8.84μm	Average grain/colony size
l_α	1.36μm	Average width of α lath in lamellar α+β colony
l_β	0.23μm	Average width of β rib in lamellar α+β colony
$V_{\alpha-grain}$	50.2%	Volume fraction of equiaxed α grains
$V_{\beta-lath}$	7.0%	Volume fraction of total β phase

3.1.2 Microstructure characterization

A practical description of the crystallographic texture for the bimodal α-β Ti-6Al-4V could be given in three aspects, viz. spatial phase arrangement, crystallographic orientation distribution and grain/colony size distribution. These aspects provide relevant information to support the finite element mesh generation.

The image of bimodal microstructure (Fig. 3.1) indicates that the arrangement of equiaxed α grains and lamellar $\alpha+\beta$ colonies can be regarded as highly random. Moreover, no preferential crystallographic orientations are observed for the equiaxed

α grains and lamellar colonies. It should be noticed that the crystallographic orientations of the α and β phases in a lamellar α+β colony are strictly coupled to each other obeying the Burgers orientation relationship (Sekiguchi et al., 2010; Suri et al., 1999), which will be briefly presented later in this paper.

Representation of the investigated bimodal microstructure is also closely linked to the experimental identification of grain/colony size distribution. In this work, a practical method (Thomas et al., 2012) of estimating three dimensional statistics from extrapolation of the EBSD two dimensional data is employed to provide reliable information about grain/colony size distributions. The average grain/colony size could be parametrized as the average diameter D of the equivalent sphere. To estimate the value of this parameter, the equivalent projected circle diameters (ECD) are first calculated from the two dimensional optical micrographs. By applying the assumption that the equiaxed α grains and lamellar α+β colonies are approximately spherical in three dimensions, D can be approximated by the following relation using the principles of stereology:

$$D = \frac{4}{\pi} \cdot ECD \tag{3.1}$$

The distribution of normalized diameter $D_{nor}=D/<D>$, where $<D>$ denotes the average over all grains and colonies, measured from the EBSD images, is illustrated in Fig. 3.3 by the solid curve.
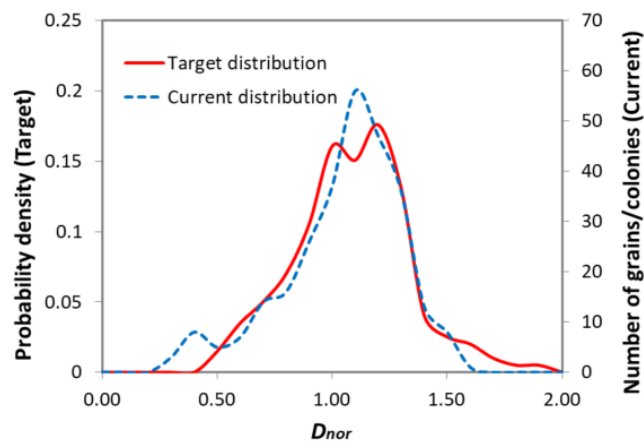
Fig. 3.3 Target distribution (solid line) and current distribution (dotted line) of normalized equivalent diameter D_{nor} of grains and colonies.

3.2 Monotonic and cyclic shear tests on CP-Ti with conventional structure and harmonic structure

3.2.1 Experimental procedure

In the present work, the pure titanium powders were prepared by using the Plasma Rotating Electrode Process (PREP) with particle size in the range of 100-180μm,. These powders were then used to prepare both the conventional (coarse grained) and harmonic structured CP-Ti samples. The chemical composition of the powders is presented in Table 3.2. The PREP titanium powder was mechanically milled (MM) in a planetary ball mill under argon gas atmosphere for 100 hours. Further, the milled powders were sintered for a period of 10 minutes at 1073K (800℃) under vacuum atmosphere to obtain the coarse grained and harmonic structured compacts. Full details on the processing route have been given by Sekiguchi et al. (2010) and Vajpai et al. (2015). The microstructural characterization of the initial powder, milled powder and the sintered compacts were observed using Scanning Electron Microscope (SEM) and Electron Backscattered Diffraction (EBSD) techniques for further analyses.

Table 3.2

Chemical composition of the PREP pure titanium powders.

Element	Ti	O	Fe	N	H	C
Amount (mass %)	99.81	0.111	0.04	0.015	0.012	0.004

Special samples were prepared in order to evaluate the mechanical properties by performing mechanical tests under monotonic and cyclic simple shear loads with an MTS 20/M testing machine with a load capacity of 100 kN equipped with a special shearing device (see Fig. 3.4). The sample geometry is a coin-shaped cylinder with 20 mm in diameter and 1 mm in thickness. The effective sheared volume is 15×2 ×1 mm^3 (Ueda et al., 2018). The external load is measured by the overall shear strain defined by Γ=u/h, where u denotes the displacement of the mobile grasp; h=2mm is the width of the sample. The loading process was controlled by a constant overall strain rate of $\dot{\Gamma} = 10^{-3}$ s^{-1} in both the monotonic and cyclic tests. Two kinds of cyclic shear tests with imposed increasing overall strain amplitudes were carried out for coarse-grained CP-Ti and harmonic structured CP-Ti. The increment of the overall

strain amplitudes is $\Delta\Gamma=1.155\%$ per cycle.
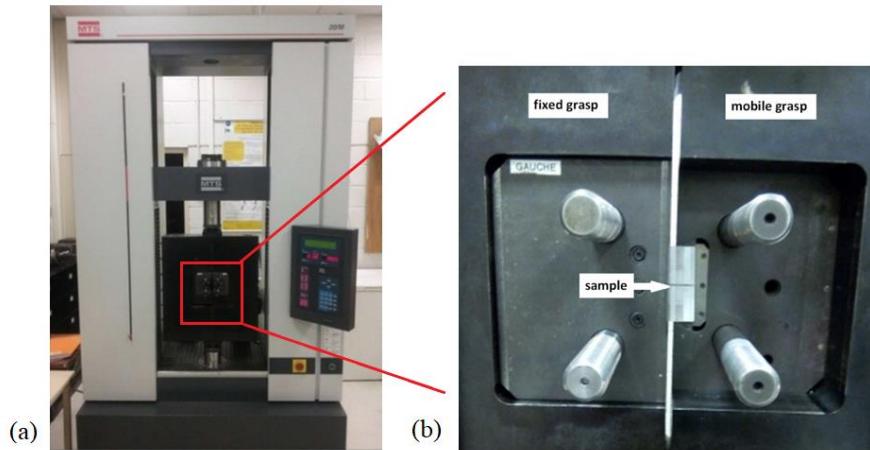
Fig. 3.4 Experimental equipment: (a) shear test setup performed on an MTS M20 testing machine, (b) sample grasping device.

3.2.2 Microstructure characterization

The description of the crystallographic texture for both CG CP-Ti and HS CP-Ti includes three aspects: spatial arrangement, grain orientation distribution and grain size distribution. These texture characteristics can be observed and measured from the EBSD images, as shown in Fig. 3.5.

The grain distribution data were measured from the EBSD images. The software MTEX was used to generate the experimental grain size and orientation list (Liu et al., 2018; Bachmann et al., 2010). According to the EBSD data, the CG CP-Ti could be viewed as an aggregation of single-crystal grains with random grain orientations. The average size of the grains is approximately 25 μm, as shown in Fig. 3.5b. The HS CP-Ti has a distinctive bimodal grain size distribution, with an average size of 5 μm for the FG region and 30 μm for the CG region, as shown in Fig. 3.5d. According to Fig. 3.6, the maximum pole density is very low (approximately 1.4 for the HS structures). Therefore, the grain orientations in both the FG and the CG regions can be considered as randomly distributed.
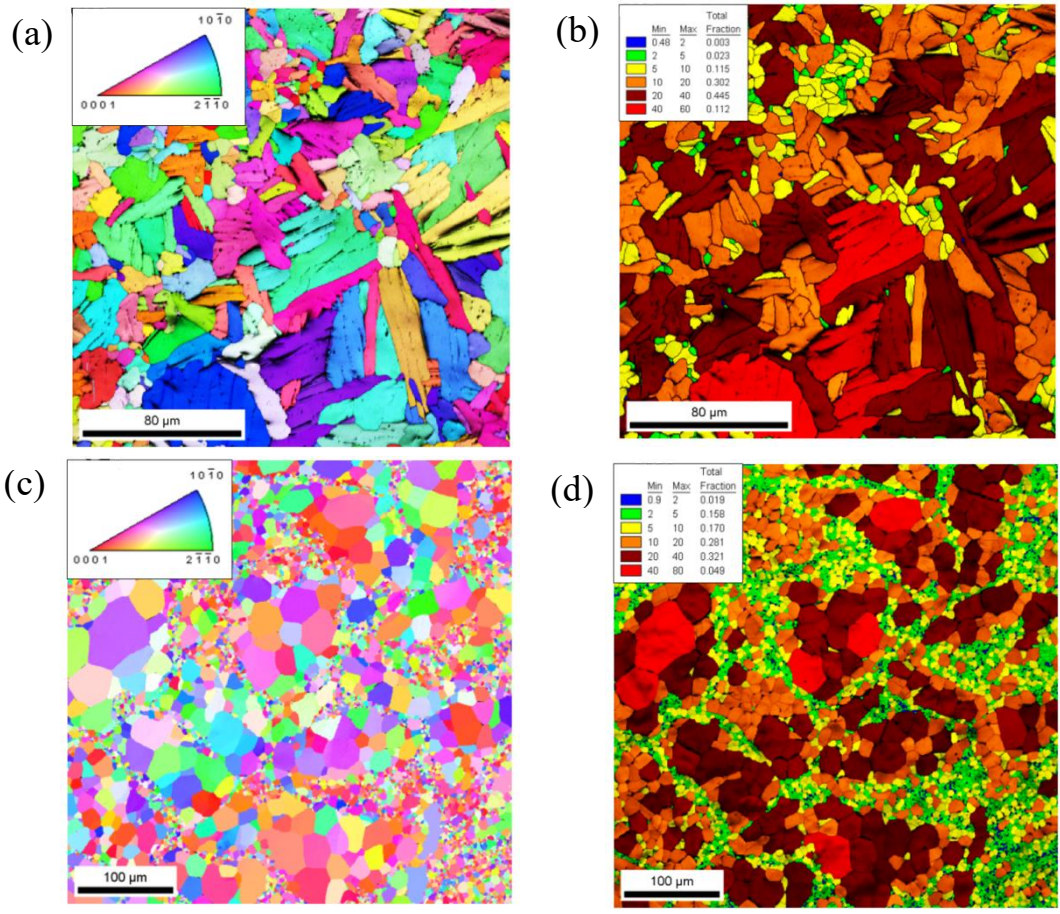
Fig. 3.5 Figures of the as-processed specimens: (a) and (c) IPF maps showing grain orientation ([0001] projection) for homogeneous coarse-grained CP-Ti and harmonic structured CP-Ti, respectively. The color code is relative to the standard stereographic projection triangle (inset); (b) and (d) figures showing the grain sizes and their distribution for homogeneous coarse-grained CP-Ti and harmonic structured CP-Ti, respectively (Hocini, 2017).

Fig. 3.6 IPF map alongside the texture strength measurement for the as-processed harmonic structured CP-Ti (Hocini, 2017).

3.2.3 Experimental results

The obtained engineering stress-strain curves are shown in Fig. 3.7. Results for homogeneous CG CP-Ti and heterogeneous HS CP-Ti are shown in the same figure in order to facilitate the observation of strengthening effect of the HS design. It can be seen from the figures that the application of the harmonic structure design on CP-Ti improves significantly the material strength with acceptable loss of ductility in comparison with its homogeneous CG counterpart in both the monotonous and cyclic shear tests. In the monotonic shear tests (Fig. 3.7a), the HS CP-Ti presents a ultimate shear strength of approximately 684 MPa and a yield stress estimated at about 320 MPa, while the conventional homogeneous CG CP-Ti has a ultimate shear strength of approximately 561 MPa and a yield strength of 220 MPa. The material strength is increased by 17.7%. The cyclic shear tests show that the homogeneous CG CP-Ti is more ductile than the HS CP-Ti. The cumulative imposed shear strain is around 174.0% for CG CP-Ti and 121.0% for HS CP-Ti when ΔΓ=1.155% every cycle. On the other hand, HS CP-Ti is more resistant because it reaches higher level of shear stress.
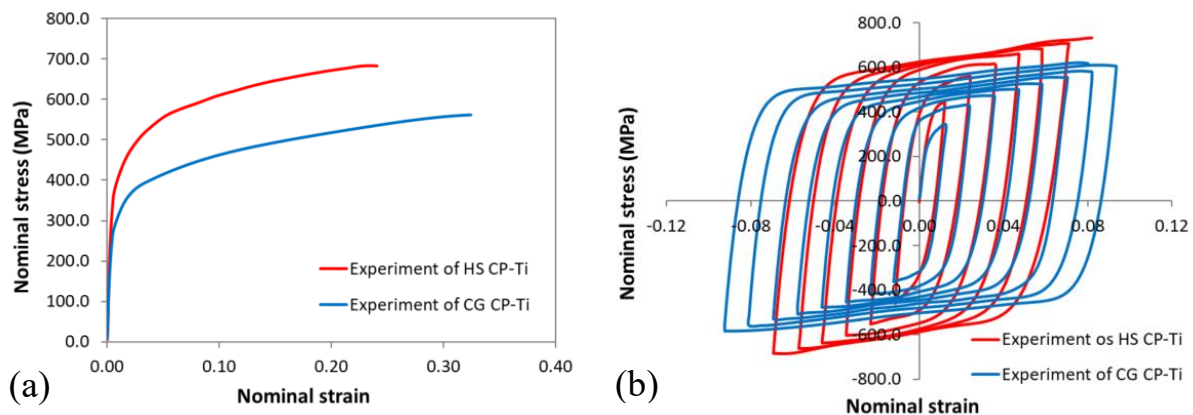
(a)   (b)

Fig. 3.7. Experimental results for (a) harmonic structured CP-Ti and homogeneous coarse-grained CP-Ti in the case of monotonic simple shear condition (b) hysteresis loops for harmonic structured CP-Ti and homogeneous coarse-grained CP-Ti in the case of cyclic simple shear condition when ΔΓ=1.155% every cycle (Hocini, 2017).

3.3 Monotonic and cyclic shear tests on Ti-6Al-4V with conventional structure and harmonic structure

3.3.1 Experimental procedure

In this study, Plasma Rotating Electrode Process (PREP) was used to prepare the Ti-6Al-4V powders whose average particle size was about 186.0μm. The chemical

composition is as follows (wt%): Al(6.51) V(4.26) O(0.18) Fe(0.17) C(0.01) N(0.003) H(0.002) Ti(balance). Homogeneous CG Ti-6Al-4V samples with β annealed microstructure were then prepared from the as-PREP powders.

For the production of the HS Ti-6Al-4V alloys, the PREP powders were further processed by mechanical milling (MM) in a planetary ball mill at room temperature under argon gas atmosphere for 25 hours. The as-PREP powders and MM powders were consolidated to make the bulk materials by spark plasma sintering (SPS) at 1123K (850 ℃) under vacuum atmosphere for 30 min. The microstructure characterizations were achieved by using scanning electron microscopy (SEM) and electron backscatter diffraction (EBSD) techniques from which the key microstructural length scales can be obtained. Full details on the processing route have been given by Dirras et al. (2015). Fig. 3.8a shows the microstructure of the investigated homogeneous CG Ti-6Al-4V, which is characterized by β annealed microstructures, where the β phase lamellae are embedded in the α phase to form lamellar α+β colonies. Fig. 3.8c shows the harmonic microstructure of the HS Ti-6Al-4V specimens, in which CG regions are surrounded by a spatially interconnected network of FG regions. It's observed that the FG regions are mainly composed of relatively small equiaxed α phase grains while the CG regions are primarily composed of lamellar α+β colonies.

3.3.2 Microstructure characterization

Due to the difficulty of identifying the lamellar colony size, the average lamellar colony size is assumed to be identical to the average length of α laths. Considering the significant contrast between widths of α and β laths, Energy-dispersive X-ray spectroscopy (EDS) was used for the chemical characterization of the sample to determine the relative abundance of the chemical elements in α lath and β lath, respectively. Then a more convincing measurement of the average width of β lath was achieved through Fig. 3.9 where the local variation of chemical compositions of Ti, Al, V in α lath and β lath is captured. The measured average lamellar α + β colony size, widths of α lath and β lath were 49.4μm, 2.5μm and 0.2μm, respectively. For the HS Ti-6Al-4V, the volume fraction of FG regions is 13.34% and the average grain size of the equiaxed α phase is 2.05μm. Based on experimental identification, the lamellar α+β colonies in CG regions are assumed to have the same

microstructural lengths as measured for homogeneous CG Ti-6Al-4V.
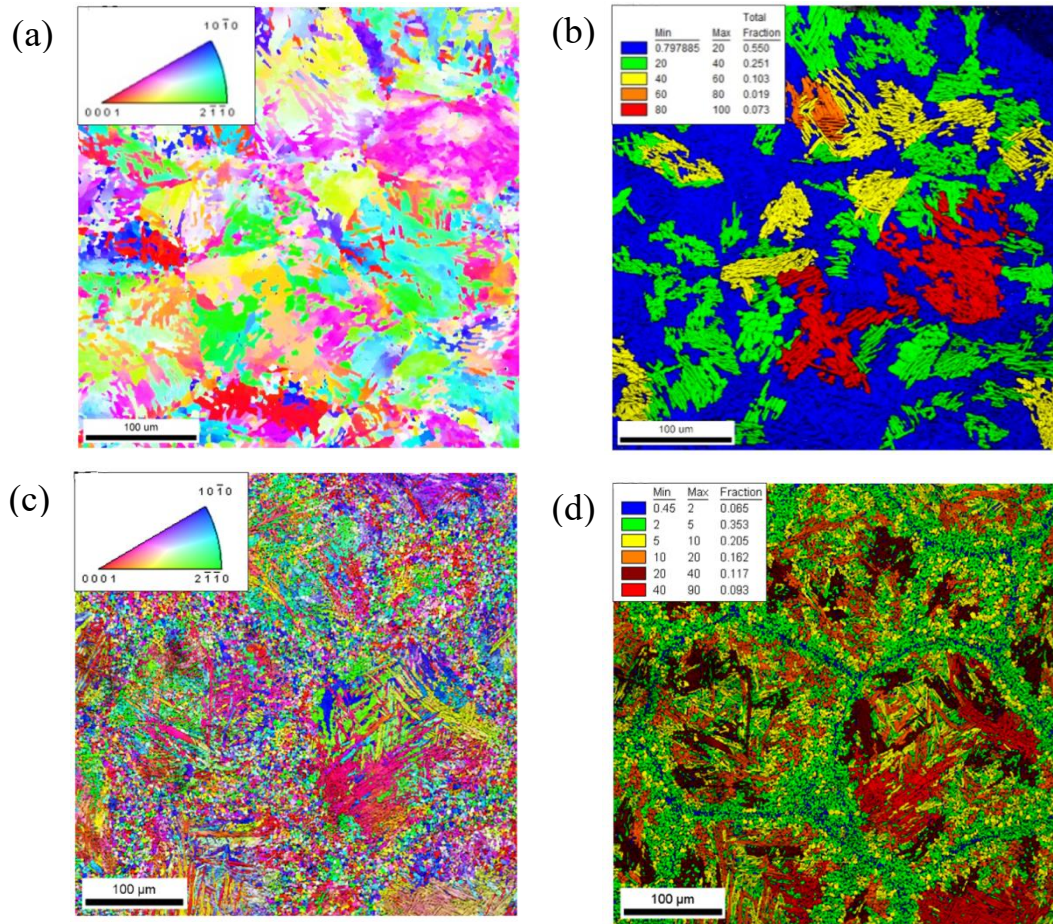
Fig. 3.8 Figures illustrating the microstructure of the as-processed specimens: (a) and (c) IPF maps showing grain orientation ([0001] projection) for homogeneous coarse-grained Ti-6Al-4V and harmonic structured Ti-6Al-4V, respectively. The color code is relative to the standard stereographic projection triangle (inset); (b) and (d) figures showing the grain sizes and their distribution for homogeneous coarse-grained Ti-6Al-4V and harmonic structured Ti-6Al-4V, respectively (Hocini, 2017). Notice the grain size gradient in the fine-grained regions (blue ≈0.45-2 μm; green ≈2-5 μm).

The mechanical properties were studied by performing mechanical tests on homogeneous CG Ti-6Al-4V and HS Ti-6Al-4V specimens under monotonic and cyclic simple shear loads on an MTSM20 testing machine equipped with a shearing device. The samples are cylindrical plates of 20 mm in diameter and 1 mm in thickness with $15 \times 2 \times 1 \text{mm}^3$ effective sheared volume. The overall shear strain is defined by $\Gamma = u/h$, where u denotes the displacement of the moving grip, and $h = 2.0 \text{mm}$ is the width of the shear zone. The load was applied with a constant overall strain rate of 10^{-3}s^{-1}. Monotonic simple shear tests and cyclic simple shear tests with imposed increasing overall strain amplitudes were performed. The increment of the overall strain amplitudes in cyclic shear tests was $\Delta\Gamma = 1.155\%$ per cycle.
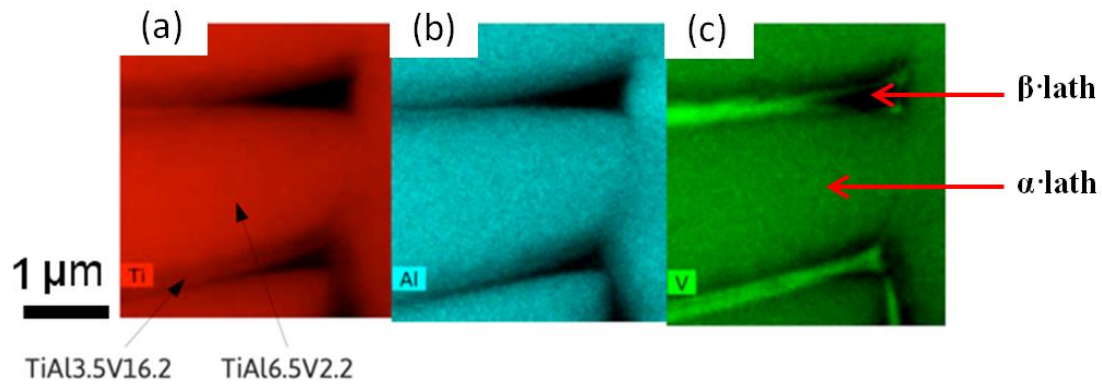
Fig. 3.9 Energy-dispersive X-ray spectroscopy map showing the relative abundance of chemical elements in α lath and β lath. The work is done by a scientific partner the Center for Elaboration of Materials and Structural Studies (CEMES) of Toulouse.

According to the inverse pole figure (IPF), no preferential grain orientation is observed. For the sake of brevity, only the analysis on IPF data of harmonic structured Ti-6Al-4V is presented as an example. It can be seen in Fig. 3.10 that the maximum pole density is quite low (about 1.6). The same results can be expected for other samples since the high temperature fabrication process used is the same. Therefore, the Euler angles which represent the grain orientations for Ti-6Al-4V can be considered as randomly distributed.
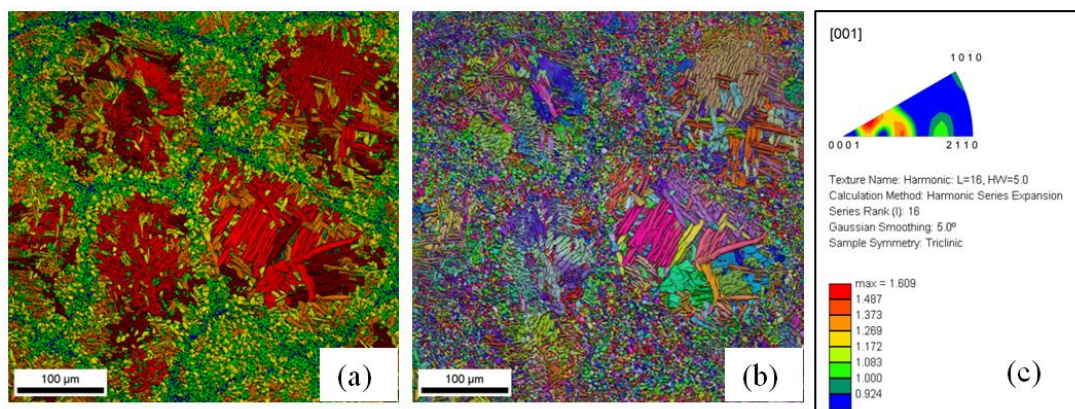
Fig. 3.10 Grain size (a) and IPF (b) maps, alongside the texture strength measurement (c) for the as-processed harmonic structured Ti-6Al-4V. Texture strength is expressed by the scale level at the bottom of (c). The microstructure characterization is part of the ANR project entitled HighS-Ti "High Strength Ti-based alloys with harmonic structure: Processing, Mechanical properties and Modeling".

3.3.3 Experimental results

Results (in Fig. 3.11) for homogeneous CG Ti-6Al-4V and heterogeneous HS Ti-6Al-4V are shown in the same figure in order to emphasis the strengthening effect of the HS design. Fig. 3.11 shows the strengthening effect of harmonic structure

design for β-annealed Ti-6Al-4V through the monotonic shear tests and cyclic shear tests and no loss of ductility have been observed in comparison with their homogeneous CG counterparts. The monotonic shear tests exhibit that the ultimate shear stress of Ti-6Al-4V is only augmented by 6.6%, from 1021 MPa (homogeneous CG Ti-6Al-4V) to 1088 MPa (HS Ti-6Al-4V). It's worth mentioning that the improvement of Ti-6Al-4V's strength by applying harmonic structure design is not as significant as that observed in CP-Ti. This phenomenon is of great interest in this thesis work since it directly reveals that different microstructure features could result in different mechanical properties even though the applied harmonic structure design is the same. While the cyclic shear tests show that the homogeneous CG Ti-6Al-4V is less ductile that the HS Ti-6Al-4V. This characteristic is contrary to that observed in the experiments for CP-Ti samples.
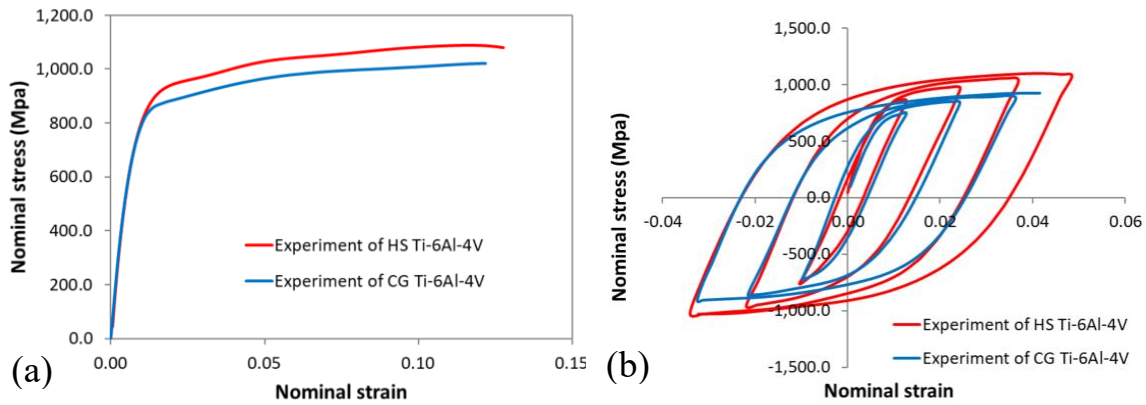
Fig. 3.11. Experimental results for (a) harmonic structured Ti-6Al-4V and homogeneous coarse-grained Ti-6Al-4V in the case of monotonic simple shear condition (b) hysteresis loops for harmonic structured Ti-6Al-4V and homogeneous coarse-grained Ti-6Al-4V in the case of cyclic simple shear condition when ΔΓ=1.155% every cycle (Hocini, 2017).

Chapter 4 Numerical studies on the influence of microstructural features on yield strength of Ti-6Al-4V by using a CPFEM high fidelity model

4.1 Introduction

In this chapter, the deformation behavior of the lamellar α+β colonies in Ti6Al4V microstructure is investigated by using the so called high fidelity modeling method (Kasemer et al., 2017) so that insight into the deformation mechanism and the microstructure-property relationship can be gained. The concepts proposed by Mayeur (2004), which accounts for the Burgers orientation relationship in a lamellar α+β colony in the 3D crystal plasticity model, are incorporated in the present high fidelity modeling such that the influences of microstructure features can explicitly be evaluated. Through this numerical study, we can investigate and then better understand the relationship between the microstructure and the mechanical properties of Ti-6Al-4V.

In this Chapter, a numerical study is presented in investigating the influence of microstructural features on the yield strength of bimodal α-β Ti-6Al-4V. Tensile tests and microscopic observation are conducted to provide experimental data of yield strength and microstructure characterization (see the experimental data presented in Chapter 3. Sets of representative volume elements (RVE) are generated using characterization data collected from electron back-scattered diffraction (EBSD). To investigate the sensitivity of macroscopic yield strength to the morphology of microstructure, the geometrical parameters such as size of equiaxed α grains and lamellar colonies, lamellar width, volume fraction of equiaxed α grains and Burgers orientation relationship (BOR), are studied systematically in a series of simulations. The simulations use crystal plasticity finite element framework to model the deformation behavior of the generated virtual samples under tensile loading condition. Yield strength trends as functions of investigated microstructural features are examined. Moreover, inspection of local deformation of individual equiaxed α grain and lamellar colony provides an insight into the relations between the microstructure and the mechanical properties.

4.2 Numerical model

4.2.1 Crystal plasticity formulation

Crystal plasticity finite element modelling (CPFEM) is a numerical method which combines the continuum mechanics and the crystal plasticity theory of metals (Donea et al., 2004). Reliable and efficient crystal plasticity theory is required not only to study the deformation mechanisms of single crystals but also to supply a robust basis for multi-scale modelling of polycrystals. Thanks to numerous pioneering works (Taylor, 1934, 1938; Schmid and Boas, 1935; Nye, 1953), the phenomenological description of macroscopic plastic strains in metals is physically well-defined in the framework of crystal plasticity theory. The cornerstone of continuum crystal plasticity theory is mainly based on the dislocation slip mechanism of crystalline materials and mesoscopic medium mechanics theory. Consequently, more realistic microscopic deformation mechanisms can be considered in the constitutive behavior laws of the metallic materials.

In all the kinematic treatments, an important concern is the way by which the shape of the investigated material changes from the reference configuration to a deformed configuration. For crystalline materials, it's recalled that the lattice could deform both by elastic displacements and by permanent displacements of local atoms. This understanding has led to a multiplicative decomposition of the total deformation gradient. Then the transformation from the reference configuration to the deformed configuration can be described as two distinct parts: plastic slip characterized by the plastic deformation gradient $\boldsymbol{F}_p$ and elastic stretching of the lattice characterized by the elastic deformation gradient $\boldsymbol{F}_e$. Therefore, the total deformation gradient $\boldsymbol{F}$ connecting the reference with the current configuration can be written in a multiplicative elastic-plastic decomposition form:

$$\boldsymbol{F} = \boldsymbol{F}_e \boldsymbol{F}_p \tag{4.1}$$

The Green-Lagrange deformation tensor $\boldsymbol{E}^e$ with respect to the intermediate configuration is calculated as

$$\boldsymbol{E}^e = \frac{1}{2}(\boldsymbol{F}_e^T \boldsymbol{F}_e - \boldsymbol{I}) \tag{4.2}$$

At the continuum level, the elastic portion of deformation is assumed to obey a linear elastic constitutive relationship, and the stress-strain relation is then defined in

terms of the elastic portion of deformation by Hooke's law. For the sake of simplicity, deformation twinning is not modeled in this work. To provide a reasonable description of mechanical behavior, anisotropy is considered in elastic and plastic responses of a single crystal by means of the elastic stiffness tensor:

$$\boldsymbol{T} = \boldsymbol{C}(\alpha, \beta, \gamma)\boldsymbol{E}^e = \boldsymbol{C}(\alpha, \beta, \gamma)(\boldsymbol{E} - \boldsymbol{E}^P) \tag{4.3}$$

where $\boldsymbol{T}$ is the second Piola-Kirchhoff stress tensor. The elasticity stiffness tensor $\boldsymbol{C}(\alpha, \beta, \gamma)$ reflects the symmetry of the investigated crystal and is a function of the crystal orientation which is represented by the Euler angles (α, β, γ).

The second Piola-Kirchhoff stress tensor $\boldsymbol{T}$ is related to the Cauchy stress tensor through the deformation gradient:

$$\boldsymbol{\sigma} = \frac{1}{\det \boldsymbol{F}} \boldsymbol{F} \boldsymbol{T} \boldsymbol{F}^T \tag{4.4}$$

Kinetic equations describing the evolution of the plastic slip rate $\dot{\gamma}^\alpha$ define the relationship between the slip shearing rate and the driving force $\boldsymbol{\tau}_\alpha$ on a given slip system α. Here the typical approach adopted in classical plasticity or visco-plasticity theories is applied. Within the wide literature, the kinetic equations have been postulated in various forms (rate dependent or rate independent). Generally, all materials are more or less rate dependent, but in the case of low homologous temperatures the rate independent approximation is also acceptable for metals.

In this thesis work, the rate dependent formulation is employed where all slip systems are assumed to be possible to activate once the threshold function is in the plastic domain. The relationship between the shearing rate of slip systems and the driving forces (resolved shear stresses) as well as the current state of the material can be given by a rate dependent formulation. The flow rule used to calculate the plastic slip rate $\dot{\gamma}^i$ of slip system i is as follows:

$$\dot{\gamma}^i = \dot{\gamma}_0 \left\langle \frac{|\tau^i| - R^i - k^i}{D^i} \right\rangle^m sgn(\tau^i) \tag{4.5}$$

where i denotes the slip system, τ^i is the resolved shear stress or the driving force (CRSS), k^i is the length scale dependent threshold stress, R^i is the evolution of isotropic hardening, $\dot{\gamma}_0$ is the reference shearing rate, D^i is the drag stress representing the slip resistance and assumed to be constant, m is the inverse strain-rate sensitivity exponent, $sgn(\tau^i)$ denotes the direction of plastic flow. All slip systems are possible to be activated once the stresses are above the threshold.

For each slip system i, whose slip direction vector and slip plane normal vector

are $\boldsymbol{S}^i$ and $\boldsymbol{M}^i$ respectively, the corresponding resolved shear stress τ^i can be calculated as:

$$\tau^i = \boldsymbol{\sigma} : \boldsymbol{m}^i \tag{4.6}$$

with

$$\boldsymbol{m}^i = \frac{1}{2}\left(\boldsymbol{S}^i \otimes \boldsymbol{M}^i + \boldsymbol{M}^i \otimes \boldsymbol{S}^i\right) \tag{4.7}$$

The isotropic hardening R^i is assumed to evolve along with the hardening rate following a phenomenological nonlinear hardening rule:

$$\dot{R}^i = a\left(Q - R^i\right)\left|\dot{\gamma}^i\right| \tag{4.8}$$

where Q denotes the saturation of isotropic hardening variable R^i, a denotes the isotropic hardening modulus.

The plastic portion of deformation $\dot{\boldsymbol{E}}^p$ is a linear summation of all activated shearing modes defined by the symmetric part of the Schmid tensor in the slip geometry:

$$\dot{\boldsymbol{E}}^p = \sum_{i=1}^{s} \dot{\gamma}^i \, \boldsymbol{m}^i \tag{4.9}$$

where s denotes the total number of the slip systems in the slip geometry.

4.2.2 Burgers orientation relationship and deformation modes

In this section, the microstructure aspect of the Ti6Al4V alloy is briefly presented. The slip systems considered in this work are shown in Table 4.1, namely 24 HCP slip systems for α phase and 12 BCC slip systems for β phase. A sufficient number of independent slip systems are particularly employed to provide degrees of freedom to accommodate generalized plasticity in the 3D simulations.

Ti-6Al-4V alloy possess a complex microstructure essentially characterized by the lamellar α+β colonies containing secondary α and β phases arranged in lamellar structure. There are 24 different slip systems in the α phase and 12 slip systems in the β phase.

The crystallographic orientation of the α and β lamellae in lamellar α+β colonies are strictly coupled to each other obeying the Burgers orientation relationship (Lutjering and Williams, 2003; Suri et al., 1999). These relationships are as follows: $(0\ 0\ 0\ 1)_\alpha \ // \ \{1\ 1\ 0\}_\beta$ and $<1\ 1\ \bar{2}\ 0>_\alpha \ // <1\ 1\ 1>_\beta$.

Table 4.1

Slip systems used for α and β crystallographic phases.

Phase	Crystal type	Name of slip families	Indices	Number of slip systems
α	HCP	Basal	$\{0001\}11\bar{2}0$	3
α	HCP	Prismatic	$\{1010\}\bar{1}\bar{1}\bar{2}0$	3
α	HCP	Pyramidal <a>	$\{1011\}\bar{1}\bar{1}\bar{1}0$	6
α	HCP	Pyramidal <a+c>/A	$\{01\bar{1}1\}2\bar{1}\bar{1}\bar{3}$	12
β	BCC	-	$\{110\}111$	12

It's generally believed that lamellar colonies have higher yield strength than equiaxed α grains (Leyens, 2003). However, based on the observation that β-Ti alloys have lower yield strength than α-Ti alloys, in some numerical studies the critical resolved shear stress of the BCC slip systems of the β phase in colonies is assumed to be less or equal to that of HCP slip systems in the α phase (Leyens, 2003; Kasemer et al., 2017). Consequently, all possible slip systems in β phase are easier to activate than HCP slip systems except the basal one in α phase. Therefore it usually results in weaker lamellar α+β colonies in terms of mechanical response, which is opposite to the common notion that the presence of lamellar colonies increases the material strength. To better consider the influence of the lamellar microstructure, the obstacle effect of the interfaces between α and β phases to dislocation motion have to be considered (Mayeur and McDowell, 2007; Neeraj et al., 2005; Brockman, 2003). Inspired by the notion in the work of Goh et al. (2003) and Mayeur (2004), we assume that slip systems with a slip direction intersecting the α/β interfaces are difficult to activate because of the relatively small effective slip distance. This mechanism is called *hard deformation mode*.

For hard deformation mode, the threshold stresses of these HCP and BCC slip systems are governed by the α lath width and the β rib width respectively through a Hall-Petch type relation:

$$k^i = k_0 + k_y\left(d^i\right)^{-0.5} \tag{4.10}$$

where k_0 is a constant frictional stress on each slip system. For the α phase lamellae and β phase lamellae, d^i is the widths of α lath and the β rib respectively. k_y is Hall-Petch constant and is non-zero only for hard slip systems.

On the contrary, the slip systems which either glide parallel to the phase

interfaces or have parallel slip planes in both phases are assumed unaffected by the interfaces' obstacles as the effective slip distances are much longer. This mechanism is called *soft deformation mode*. These soft slip systems consist of three basal, one prismatic and two $\langle 111 \rangle \{110\}$ slip systems. The corresponding threshold stresses of these soft slip systems are not governed by the microstructural length scales as the hard slip systems. Similarly, threshold stresses of all HCP slip systems in equiaxed α grains are not length scale dependent too.

4.2.3 Global algorithm

The above-described constitutive formulations were implemented numerically into a finite element code named Cast3M developed by the French Alternative Energies and Atomic Energy Commission by using a user-defined material subroutine (UMAT) written in Fortran language. The simulation method is capable of modeling large deformation of a polycrystal. The external displacement-controlled loads are applied incrementally. Equilibrium is required at each loading step. The global algorithm is briefly listed as follows:

1. At each incremental loading step, resolve the macroscopic incremental elastic problem by taking the plastic strain of the previous step into consideration, and then calculate the stress fields;

2. At each Gauss point, evaluate the flow rule and check for the visco-plastic process, then calculate the plastic slip rate for all possible slip systems;

3. Calculate the plastic strain velocity at each Gauss point;

4. Recalculate the macroscopic stress and internal variables by taking the updated plastic strain into account until the convergence.

4.2.4 Mesh generation and boundary conditions

In this Section, the 3D high fidelity finite element models of the bimodal microstructure of Ti-6Al-4V are generated on the basis of the Voronoi tessellations by using the four node tetrahedral elements (TET4). A special algorithm was adapted to create the complicated bimodal microstructure. This algorithm produces convex equiaxed α grains and lamellar $\alpha+\beta$ colonies with planar facets separating them. The construction of planar boundaries is aimed to avoid 'stair-stepped' boundaries

between grains/colonies, which have been reported to be the source of local instabilities in simulations (Kanit et al., 2003). The bimodal RVEs contain about 180 grains/colonies in total, composed of approximately 360,000 elements and 60,000 nodes, as shown in Fig. 4.1.

Based on the microstructure characterization presented-above, these FE models exhibit the following features:

1. The equiaxed α grains and lamellar $α+β$ colonies are randomly arranged only with particular attention paid to avoid large clusters of either phases. Particular efforts were made such that the resulting FE meshes for lamellar $α+β$ colonies consist of a certain number of parallel planes representing the phase interfaces according to which α and $β$ phases can be separated. The volume ratio between α and $β$ phases can easily be controlled through two factors: first, the volume fraction of the equiaxed α grains and second, the volume fraction of α phase in lamellar $α+β$ colonies.

2. The crystallographic orientations of the equiaxed α grains and lamellar $α+β$ colonies are randomly distributed. Every individual grain/colony has its phase identification and a crystallographic orientation defined by 3 Euler angles. Inside each lamellar $α+β$ colony, the crystallographic orientation of each phase is closely linked to the lamellae normal following the Burgers orientation relationship. Each time a new orientation is assigned, the FE mesh of a lamellar colony changes and the whole simulation geometry changes accordingly.

3. The sizes of the equiaxed α grains and lamellar $α+β$ colonies are generated according to the microstructure characterization data. The parameters in the construction of FE meshes are determined by fitting the red target curve presented in Fig 3.11. In the same figure, we compare a current distribution of grain/colony sizes generated from this normal distribution law, represented by the dashed curve, with the target distribution. A good agreement between the target and current distributions can be observed when the total number of the generated grains and colonies is 180. It should be noticed that large FE models with many grains and colonies generally provide a good fitting results and a reasonable description of microstructure's heterogeneity at the expense of heavy computational effort. In order to get a good compromise, the total number of grains and colonies in a RVE in this work is chosen in the range of 100-300.

Tensile simulations with constant strain rate of the polycrystalline model are conducted in this work in accordance with the used experimental data. Homogeneous

strain boundary conditions were imposed on the contour of the mesh by a displacement vector $u_i = \varepsilon_{ij} r_j$. Four lateral faces were free in all boundary conditions, whereas a displacement was imposed on the two faces perpendicular to z axis (see Fig. 4.1a). For the tensile tests in z direction, the tensor components were, $\varepsilon_{11} = 0$, $\varepsilon_{22} = 0$, $\varepsilon_{33} = 5.0\%$, $\varepsilon_{12} = 0$, $\varepsilon_{13} = 0.$, $\varepsilon_{23} = 0$.

(a)

30μm
(Z)

30μm
(X)

30μm
(Y)

Bimodal microstructure

Lamellar colonies

(b)

Equiaxed α grain

Lamellar colony

Lamellar colony

Fig. 4.1 (a) Representation of the microstructure for bimodal α-β Ti-6Al-4V containing 180 grains/colonies in total, where the widths of β rib and α lath are respectively 0.23μm and 1.36μm, and the volume fraction of equiaxed α grains is 50.0%. Equiaxed α grains are colored arbitrarily. Lamellar α+β colonies are colored using a binary color scale, where blue represents the α lath, red represents the β rib. (b) Examples of the generated α grains and lamellar colonies with random shape and different lamellae normal (represented by black arrows).

4.2.5 Material parameters

Model parameters were either gathered from associated literature or calibrated from the experimental result (see the experimental data in Section 3.3. Single crystal elastic constants for α phase and β phase were based on the values reported in the related works (Barton and Dawson, 2001; Kelly and Groves, 1970) and are listed in

Table 4.2. The values of the slip strengths D^i for different slip systems were determined by referring to the work of Song et al. (2008) and similar to values reported in other literature (Bridier et al., 2009; Yang et al., 2001). The slip strength of bcc slip systems was set equal to that of the basal systems of the hcp slip systems. k_y was taken as the average of the values reported in Kalidindi et al. (2003) and Picu and Majorell (2002). k_0 was estimated by fitting the yield strength of the monotonic tensile test for the bimodal α-β Ti-6Al-4V. The values of $\dot{\gamma}_0$ and m in the flow rule were chosen from the work of Zhang et al. (2007) with minor change. Strain hardening parameters, namely Q and a, were chosen to limit the magnitude of hardening and effectively suppress evolution of the saturation strength by referring to Kasemer et al. (2017). Other parameters except the elastic constants are listed in Table 4.3.

Table 4.2

Single crystal elastic constants for α phase and β phase in units of GPa, using the notion defined in Kelly and Groves (1970).

β			α				
C_{11}	C_{12}	C_{44}	C_{11}	C_{12}	C_{33}	C_{44}	C_{13}
133.1	95.1	42.7	159.58	91.06	181.17	46.7	69.47

Table 4.3

Crystal plasticity parameters used in this work.

Parameter	Value	Parameter	Value
D^{basal}(MPa)	353	k_0(MPa)	10.6
D^{prism}(MPa)	397	k_y(MPa $\cdot$ $mm^{0.5}$)	17.0
$D^{pyr<a>}$(MPa)	441	M	15.0
$D^{pyr<c+a>}$(MPa)	503	$\dot{\gamma}_0(s^{-1})$	0.003
D^{bcc}(MPa)	353	Q(MPa)	20.0
		A	20.0

4.3 Simulation results and discussion

A series of simulations were designed to investigate the influence of microstructural features on yield strength of the bimodal α-β Ti-6Al-4V. To this end, an RVE with fixed dimension of 30×30×30 μm^3 was built to generate an array of virtual samples with varied geometry features and subjected to tensile loading up to

the onset of plastic yielding. The main microstructural features studied in the present work were the grain/colony size (D), the widths of α lath (l_α) and β rib (l_β) in lamellar $\alpha+\beta$ colony, the volume fraction of equiaxed α grain ($V_{\alpha-grain}$), the mechanical constraints introduced by Burgers orientation relationship (BOR). A full list of simulations is designed around these values and presented in Table 4.4.

Table 4.4

List of simulations conducted to investigate the influence of microstructural features on yield strength for bimodal α-β Ti-6Al-4V. Replications refer to the number of orientation sets used for each geometry with a prescribed microstructural feature.

Simulations	No. of grains/colonies	l_α/l_β	$V_{\alpha-grain}$(%)	BOR	Hall-Petch	Replications
Set 1	180	6	50	Yes	Yes	5
Set 2	180	6	50	Yes	No	5
Set 3	40,80,130,180,230	6	50	Yes	Yes	5
Set 4	180	2,4,6,8,10	50	Yes	Yes	5
Set 5	180	2,4,6,8,10	50	Yes	No	5
Set 6	180	6	25,37.5,50,62.5,75	Yes	Yes	1
Set 7	180	6	25,37.5,50,62.5,75	No	Yes	1

4.3.1 Simulations Set 1: Using referential values of parameters

The basic values of the microscopic parameters are fixed as follows: the total number of grains/colonies is 180, l_β=0.23±0.1µm, l_α/l_β=6, $V_{\alpha-grain}$ =50% with the BOR and the Hall-Petch law (Eq. 4.10) respected. These simulations permit us to compare with the experimental data and to validate the numerical model. Moreover, detailed insight can be gained on deformation mechanisms of different microscopic factors.

Comparison with the experimental data: The simulation results using CPFEM model on the basis of the generated high fidelity representation of the bimodal microstructure (Fig. 4.1) are compared with the experimental data of the monotonic tensile test for the bimodal α-β Ti-6Al-4V. This is to experimentally validate the used constitutive model and the proposed representative microstructure, before a series of numerical studies about the microstructure's influence on material properties are carried out on the generated virtual specimens. In fact, a good fitting with the

experimental stress/strain curve is not a prerequisite for qualitative investigation of microstructure's influence on material properties as long as values of model parameters are chosen reasonably (Kasemer et al., 2017). Here the emphasis is placed on the comparison between engineering yield strength obtained from the tensile experiment, defined by the by the 0.1% offset method, as shown in Fig. 4.2. The numerical yield strength is estimated to be 958.8 MPa, which is in a good agreement with the experimental one (973.2 MPa).
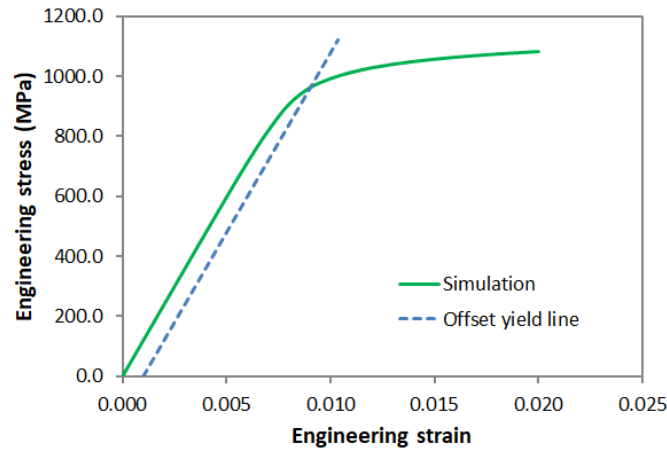
Fig. 4.2 Simulated stress-strain curve for the bimodal α-β Ti-6Al-4V with offset yield line (dashed).

Stress distribution in grains/colonies: Fig. 4.3 displays the volume averaged tensile stress for each equiaxed α grain and lamellar colony as a function of the angle of their c-axis to the loading direction z axis, where the influence of the lamellar microstructure on slip activities in α lamellae and β lamellae is considered by means of Hall-Petch relationship (Eq. 4.10). The analyzed response is corresponding to the moment when overall tensile strain is 1%, which is slightly after the onset of global yield.

From Fig. 4.3, it's seen that when the equiaxed α grains and lamellar colonies have their c-axis of the contained α phase closely aligned with the tensile loading direction z axis, the volume averaged tensile stress is highest. This can be explained by the fact that when the influence of the lamellar microstructure on slip activities is considered, the most easily activated slip systems are still within the basal and prismatic ones as long as Burgers orientation relationship is obeyed, and for HCP slip systems the stiffest orientation is typically c-axis where the basal or prismatic slip is difficult to activate. It should be noticed that when l_α/l_β is 6, the volume fraction of β phase in the lamellar colonies is relatively low and it's α phase that plays the predominant role. Fig. 4.3 also shows that as the angle increases from 0º to 45º, the

volume averaged tensile stress decreases and reaches its lowest point, which implies that slip activities become easier, and consequently the grains and colonies are softer. When the angle between c-axis and the loading condition z axis crosses 45º, the volume averaged tensile stresses are observed to increase again. The evolution of volume averaged tensile stress with respect to the angle shows a certain degree of symmetry. But generally speaking the c-axis remains to be the stiffest orientation. It's seen that the variation of volume averaged tensile stress among all angles can reach approximately 300-400 MPa for lamellar colonies and 200-300 MPa for equiaxed α grain. It can be remarked that the mechanical behavior of both α grains and lamellar colonies is greatly influenced by the crystallographic orientation. This observation probably explains why the yield strength of the material is most variable when the number of grains/colonies is 40 (see Fig. 4.8). And it underlines again that sufficient grains/colonies are important to preserve the macroscopic isotropy of the material.
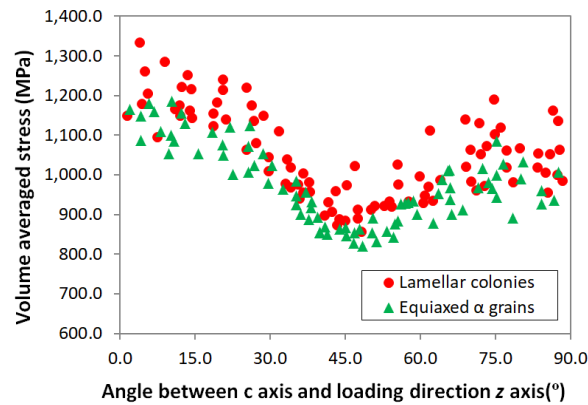
Fig. 4.3 Volume averaged tensile stress for each equiaxed α grain and lamellar colony, at the overall strain of 1%, is plotted as a function of the angle between c-axis and loading direction z axis for the case where the influence of the lamellar microstructure on slip activities is considered by means of Eq. 4.10. Red points represent the response of lamellar colonies and green points represent the response of equiaxed α grains.

Besides, it's worth noting that, by introducing the effect of the lamellar microstructure into the current model; the lamellar colony tends to be harder than the equiaxed α grain when their c-axes are at a same angle to the loading direction z axis, as shown in Fig. 4.3. This is most likely caused by the strengthening effect of α/β phase interfaces in lamellar structure which provides obstacles to dislocation motion and hinders the onset of plastic deformation on slip systems with a slip direction intersecting the α/β interfaces. This observation is consistent with the yield strength trend plotted in Fig. 4.13 where the yield strength decreases with increasing volume fraction of α grain. The more the relatively softer α grains in the material, the lower

the yield strength.

Stress distribution in individual lamellar colony: Having a close look at the local deformation of individual lamellar colony may provide us an insight into the influence of microstructural features on the resulting macroscopic behavior. Our focus is now on the different responses observed in α and β phases within the colony and discussing their mechanism of formation and influence on the material properties. It's found that in a small number of colonies, bands of relatively low tensile stress are formed in β lamellae and separated by areas of intense tensile stress presented in α lamellae (see Fig. 4.4), while in the majority of colonies tensile stress in β lamellae is higher (see Fig. 4.5) or at least comparatively identical to that in α lamellae. Furthermore, it's found that all the colonies with β lamellae being relatively softer have their c-axis closely aligned with the tensile loading direction z axis. This is most likely attributed to the fact that when the c-axis of α lamellae is closely aligned with the loading direction, one of {110} slip planes in β lamellae is closely parallel to the loading direction because of the Burgers orientation relationship and therefore the resolved shear stresses on the two BCC slip systems within the {110} slip plane could be quite large, slip would be easier to activate and consequently β lamellae turns to be softer. Fig. 4.4 shows the spatial distribution of tensile stress for two lamellar colonies whose c-axis is closely oriented along the loading direction. However, the case where the c-axis of α lamellae is closely aligned with the loading direction doesn't frequently appear, therefore such response is only observed in a small number of colonies.

As a comparison, Fig. 4.5 shows the spatial distribution of tensile stress for two lamellar colonies whose c-axis is not oriented along the loading direction. It's seen that stress concentration emerges in β lamellae, which is contrary to the response observed in Fig. 4.4. This may be attributed to the relatively small effective slip distance in β lamellae than that in α lamellae and consequently stronger obstacles to dislocation motion in β lamellae is resulted and much higher threshold stress is assumed by Eq. 4.10, thus making the β lamellae harder. These observed local responses are found to be in a good agreement with the yield strength trend in Fig. 4.10. When l_α/l_β is large, its variation only has a smaller effect on yield strength because the mechanical constraints introduced by β lamellae mainly effect the neighboring domain. But with l_α/l_β being small, for example 2, and the volume fraction of colonies being fixed, the volume fraction of β lamellae increases greatly

and the influence of harder β lamellae maybe observed.

Fig. 4.4 Distributions of tensile stress in z direction at the overall strain of 1% obtained from simulation considering the influence of the lamellar microstructure on slip activities by Eq. 4.10, for colonies whose c-axis is at (a) a 4.4 degree and (b) a 1.9 degree to loading direction z axis. In the mesh, red represents β lamellae, colored parts represent α lamellae.
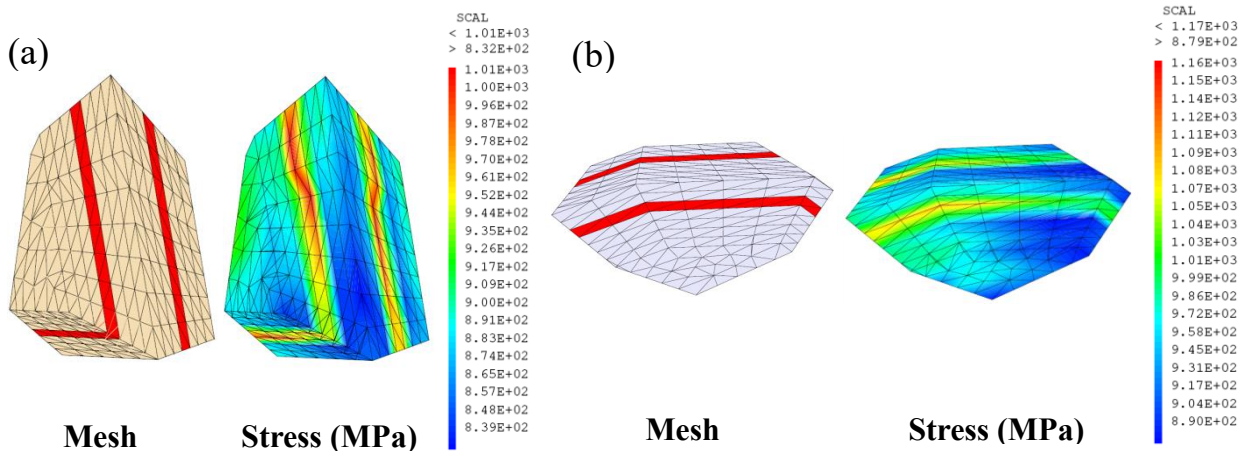
Fig. 4.5 Distributions of tensile stress in z direction at the overall strain of 1% obtained from simulation considering the influence of the lamellar microstructure on slip activities by Eq. 4.10, for colonies whose c-axis is at (a) a 40.9 degree and (b) a 34.4 degree to loading direction z axis. In the mesh, red represents β lamellae, colored parts represent α lamellae.

4.3.2 Simulations Set 2: Role of the α/β interfaces

In the work of Kasemer et al. (2017), the slip resistance of the BCC slip systems of the *β* phase lamellae is assumed to be less or equal to that of HCP slip systems in the *α* phase lamellae and the constitutive relations don't include an inherent length scale. It's said the local stress field is influenced by the morphology of the microstructures and distribution of phases. Under this scheme, their simulations show that the inclusion of the *β* lamellae lowered the yield strength and makes the material

softer. This is not consistent with our understandings and experimental observations. In Fig. 4.13, it's shown that, with the consideration of the obstacles of α/β interfaces through the Hall-Petch type relation (Eq. 4.7), the influence of microstructural length scale for lamellar colonies can be well captured. Numerical results which are in agreement with our understanding that the presence of lamellar colonies increases the material strength can be obtained.

Stress distribution in grains/colonies: Once again the local deformation of individual lamellar colony is inspected to provide us an insight into the local response resulted by neglecting the influence of lamellar structure represented by Eq. 4.10. As a comparison with simulation discussed in Fig. 4.3, Fig. 4.6 plots the volume averaged tensile stress as a function of the angle of c-axis for the corresponding α phase to the loading direction z axis. The simulation uses the same geometry but doesn't take into account of the influence of α/β interfaces. In Fig. 4.6, it's shown that the calculated volume averaged tensile stresses exhibits the same trend as that for simulations plotted in Fig. 4.3. There is also a strong correlation between the volume averaged tensile stress and the angle of c-axis to loading direction z axis, but the variation of stresses for each α grain and lamellar colony is comparatively smaller than that observed in Fig. 4.3. And it's difficult to identify which one is harder, because the volume averaged tensile stresses for equiaxed α grains and lamellar colonies are more or less overlapping with each other.
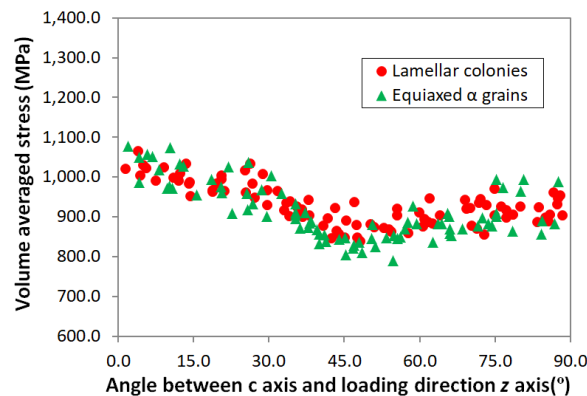
Fig. 4.6 Volume averaged tensile stress for each equiaxed α grain and lamellar colony, at the overall strain of 1%, is plotted as a function of the angle between c-axis and loading direction z axis for the case where the influence of the lamellar microstructure on slip activities isn't considered by means of Eq. 4.10. Red points represent the response of lamellar colonies and green points represent the response of equiaxed α grains.

Stress distribution in individual lamellar colony: But having a look at the tensile stress distribution of every lamellar colony, it's found that colonies with their

c-axis closely aligned with the tensile loading direction z axis all have bands of relatively low tensile stress in β lamellae, as the same as observed in the case where the influence of the lamellar microstructure on slip activities is considered. The same colonies with c-axis being closely oriented along the loading direction are selected to plot the spatial distribution of tensile stress, as shown in Figs. 4.7a and 4.7b. While for colonies whose c-axis isn't closely oriented along the loading direction, bands of relatively low tensile stress are still observed in β lamellae as shown in Figs. 4.7c and 4.7d, which is contrary to the results in Fig. 4.5. The β lamellae tend to soften the colonies whatever the crystallographic orientation is. This is most likely attributed to the relatively low slip resistances of BCC slip systems compared to those of HCP slip systems. Slip is then more easily activated in β lamellae. When the volume fraction of β phase is high in colonies, the softening effect is more significant. It's consistent with the observations in Fig. 4.11.
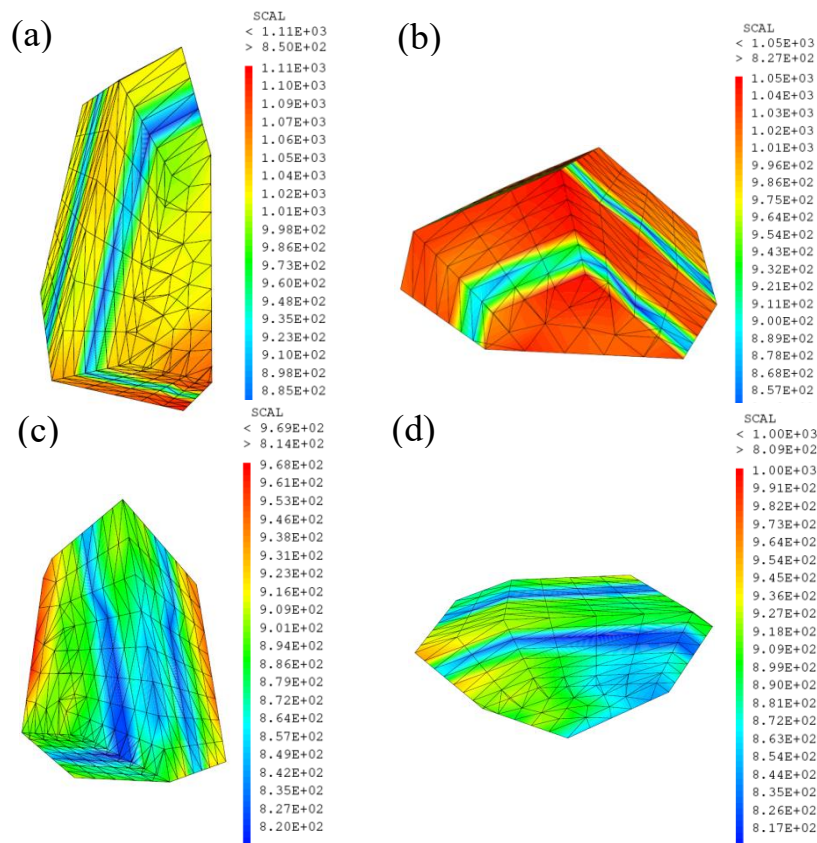
Fig. 4.7 Distributions of tensile stress in z direction at the overall strain of 1% obtained from simulation considering the influence of the lamellar microstructure on slip activities by Eq. 4.10, for colonies whose c-axis is at (a) a 4.4 degree, (b) a 1.9 degree, (c) a 40.9 degree and (d) a 34.4 degree to loading direction z axis. In the mesh, red represents β lamellae, colored parts represent α lamellae.

4.3.3 Simulations Set 3: Influence of the grain/colony size

By using fixed values for other parameters, five microstructure geometries with 40, 80, 130, 180, 230 grains/colonies in an RVE were constructed. To obtain reliable sensitivity analyses for each of the five microstructure geometries, five simulations, each with a different crystal orientation set, were carried out for each microstructure geometry.

The results of sensitivity analyses of yield strength to variation of the grain/colony size are plotted in Fig. 4.8. It can be seen from Fig. 4.8 that there is a strong positive correlation between the total number of grains/colonies and the offset yield strength. It's observed that the yield strength increases as the total number of grains/colonies increases or as the size of grains/colonies decreases. As the refinement of grains/colonies introduces larger grains/colonies boundaries which impede dislocation motion, the onset of plastic deformation is therefore hindered and higher yield strength is obtained.
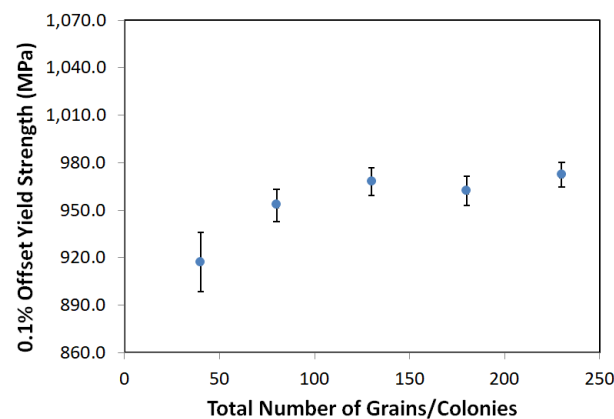
Fig. 4.8 Evolution of yield strength of bimodal α-β Ti-6Al-4V obtained from simulations for variations in the grain/colony size, which is represented by the total number of grains/colonies.

4.3.4 Simulations Set 4: Influence of the lamellar width

Five microstructure geometries with l_α/l_β= 2, 4, 6, 8 and 10 respectively were generated. The range of variation of the ratio was determined by referring to realistic ranges observed in experiments (Lee, 2004). Moreover, five simulations using a distinct crystal orientation set were conducted for each l_α/l_β ratio. Example geometries with varying lamellar width can be seen in Fig. 4.9.

For the variation of l_α/l_β the lamellar, the yield strength is observed to remain

nearly constant (Fig. 4.10). It can be said that the variation of α lath width has a smaller effect on yield strength compared to the strong influence observed for variation of other microstructural features. It's interesting to notice that, in this geometry set, the volume fraction of β phase changes along with the variation of l_α/l_β, as shown in Fig. 4.10. It's seen that when the value of l_α/l_β increases from 2, the volume fraction of β phase drops largely at first from 16.7 and then changes smoothly as $l_\alpha/l_\beta > 6$. This trend is somehow in agreement with the yield strength trend.
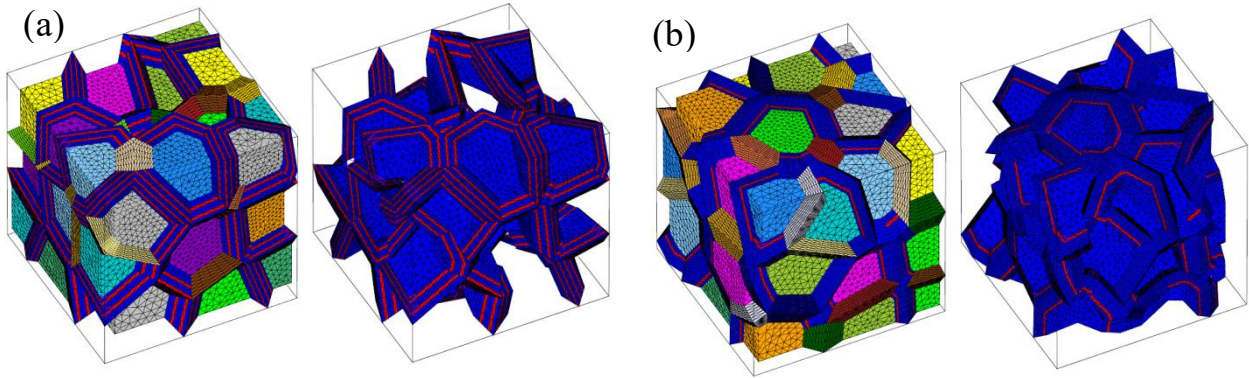
Fig. 4.9 Examples of microstructure geometries containing 180 grains/colonies, with $V_{\alpha-grain}$ being 50.0%, and l_α/l_β being (a) 2 and (b) 10. The two simulation geometries are assigned with different orientation sets. Equiaxed α grains are colored arbitrarily. Lamellar $\alpha+\beta$ colonies are colored using a binary color scale, where blue represents the α lath, red represents the β rib.
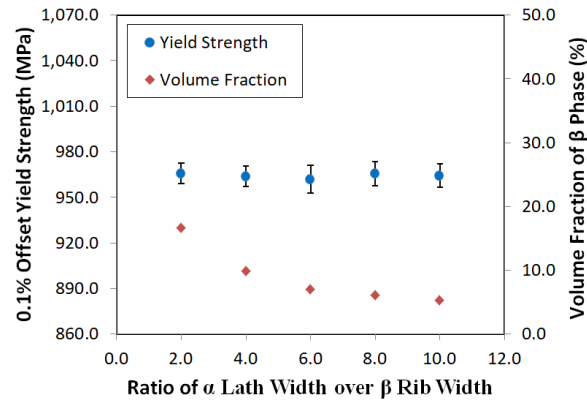
Fig. 4.10 Evolution of yield strength of bimodal α-β Ti-6Al-4V obtained from simulations for variations of lamellar width, where the β rib width is fixed, the ratio of α lath width over β rib width is varied.

4.3.5 Simulations Set 5: Influence of the lamellar width without considering the α/β interface effect

In this section, to provide an insight into the effect of the introduction of Eq. 4.9

or the influence of lamellar microstructure, the same set of geometries for the study of variation of the lamellar width as summarized in the third simulation set in Table 4.3 are used to carry out simulations where the deformation mechanism represented by Eq. 4.10 is out of the constitutive model and the threshold stress is the same in all slip systems for the α lamellae, β lamellae and equiaxed α grains. The yield strength trend and the evolution of the volume fraction of β phase are plotted together in Fig. 4.11. It's seen that the yield strength increases first but remains constant as the ratio of α lath width over the β rib width increases, which is different from the results shown in Fig. 4.10. This can be explained by the fact that the slip resistances of 12 BCC slip systems in β phase are equal to those of 3 basal slip systems and lower than those of other 21 slip systems in α phase. The slip activities in β phase are very likely to emerge at a lower stress than that in α lamellae and equiaxed α grains. The inclusion of the β lamellae softens the material. When the volume fraction of β phase is high, the yield strength turns to be lower. But its effect on yield strength is also limited. If the volume fraction of β phase changes in a small range, little or no effect on the yield strength is observed. This indicates that the strengthening effect of the inclusion of β phase lamellae cannot be well captured only by the microstructure representation of lamellar colonies in FE meshes. It's necessary to explicitly incorporate the length scale effect of the lamellar microstructures into the constitutive laws as proposed in this work.
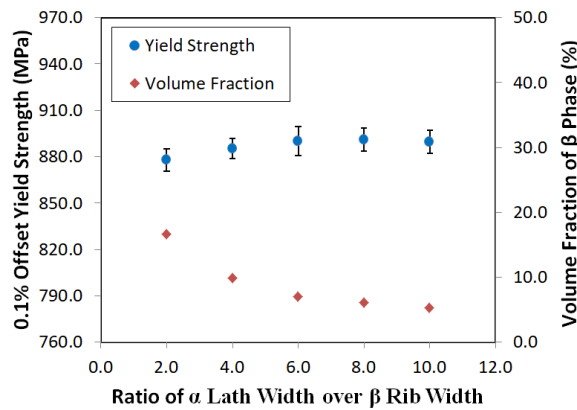
Fig. 4.11 Evolution of yield strength of bimodal α-β Ti-6Al-4V obtained from simulations for variations in the lamellar width, where the β rib width is fixed, the ratio of α lath width over β rib width is varied and the obstacles of α/β interfaces are not considered by neglecting Eq. 4.7.

4.3.6 Simulations Set 6: Influence of the volume fraction of equiaxed α grains

Five microstructure geometries with $V_{\alpha-grain}$ being 25%, 37.5%, 50%, 62.5% and 75% respectively were constructed. Example geometries with varying $V_{\alpha-grain}$ can be seen in Fig. 4.12.
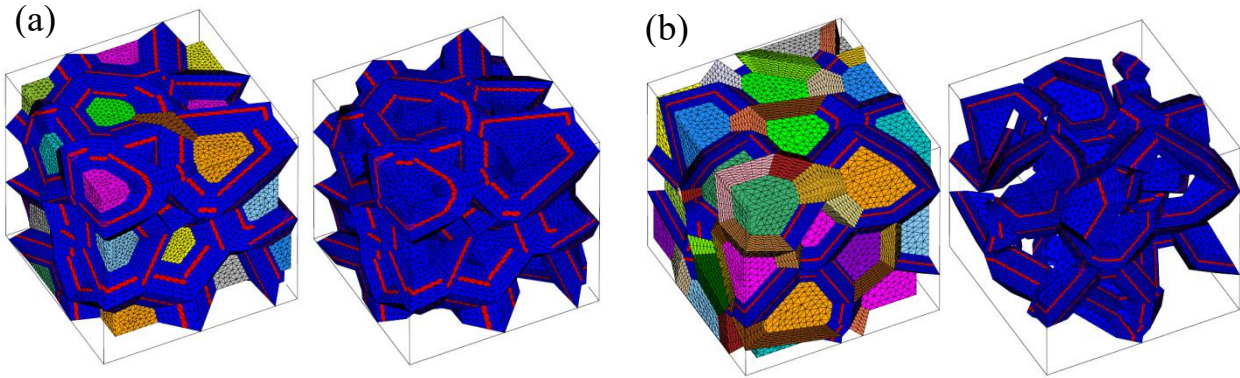
Fig. 4.12 Examples of microstructure geometries containing 180 grains/colonies, with l_α/l_β being 6, and $V_{\alpha-grain}$ being (a) 25% and (b) 75%. Equiaxed α grains are colored arbitrarily. Lamellar α+β colonies are colored using a binary color scale, where blue represents the α lath, red represents the β rib.
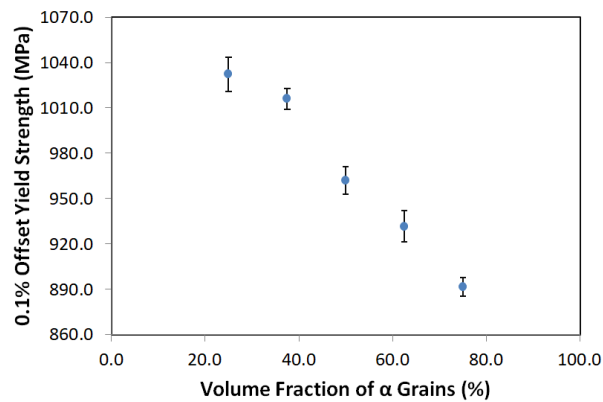
Fig. 4.13 Evolution of yield strength of bimodal α-β Ti-6Al-4V obtained from simulations for variations in the volume fraction of equiaxed α grains.

Fig. 4.13 shows the yield strength trend when $V_{\alpha-grain}$ varies in the range of 0.25 to 0.75, while other microstructural features are fixed as described. It's shown that a strong negative correlation is observed between the volume fraction of α grains and the offset yield strength: the yield strength decreases with increasing volume fraction of α grains. This trend is consistent with the common understanding that lamellar colonies are harder than equiaxed α grains. The more lamellar colonies are contained in the Ti-6Al-4V, the higher yield strength the material shows. Similar

negative correlation between the volume fraction of α grains and yield strength was also observed in the numerical study and experimental data of Zhang et al. (2007).

4.3.7 Simulations Set 7: Influence of the Burgers orientation relationship

Same microstructure geometries as defined at set 3 were simulated first with the BOR strictly respected in lamellar $\alpha+\beta$ colonies. Then each geometry was simulated again with the crystallographic orientation of α phase (both in equiaxed α grain and α lamellae) remaining the same and the orientation of β lamellae randomly assigned.

Fig. 4.14 presents the yield strength trend for simulations when $V_{\alpha-grain}$ varies in the range of 0.25 to 0.75 too, while one set of simulations with the enforcement of Burgers orientation relationship between α and β lamellae, and another without. It's seen that when Burgers orientation relationship is not enforced, the yield strength is higher. This is most likely caused by the fact that, when the crystallographic orientations of α and β lamellae in lamellar colonies are strictly coupled to each other obeying the Burgers orientation relationship, basal slip systems and the two $\langle 111 \rangle \{110\}$ slip systems (see Fig. 4.1a) have parallel slip planes and the dislocation motions in these planes are able to traverse the entire length of lamellar colonies effectively. Once the Burgers orientation relationship is not enforced, dislocation motions in these planes will also be impeded by the α/β interfaces and therefore slip activities on more slip systems in both phases are hindered by the lamellar microstructure, thus producing high yield strength. Moreover, the fewer of equiaxed α grains in the material and the more of the lamellar $\alpha+\beta$ colonies, the difference is bigger between the two sets of simulations.
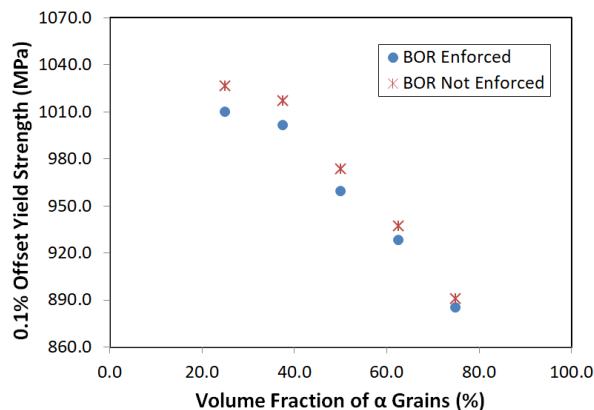
Fig. 4.14 Evolution of yield strength of bimodal α-β Ti-6Al-4V obtained from simulations for Burgers orientation relationship enforced or not.

4.4 Summary and conclusions

In above sections, the microstructure sensitivities of the macroscopic behavior are studied by means of both the stress-strain curves and the distribution of local fields. Deformation mechanisms are discussed for each selected microstructure feature in order to provide an understanding about how the variation of a microstructure feature affects the yield strength of the material. For the sake of convenience, the main influences of investigated microstructures on the yield strength of bimodal α-β Ti-6Al-4V are summarized in Table 4.5.

Table 4.5

Influence of microstructure on the yield strength of Ti-6Al-4V.

Case	Main influence
Increase No. of grains/colonies	Yield strength increases obviously when No. of grains/colonies is less than 150 and then tends to saturate.
Increase l_α/l_β	Yield strength varies slightly. The lath widths have a smaller effect on yield strength compared to others.
Increase volume fraction of α grains	Yield strength decreases significantly.
BOR enforced	Yield strength decreases. The higher the volume fraction of lamellar colony, the more the yield strength decreases.
Effect of α/β interfaces considered	Yield strength increases significantly. Lamellar colonies are distinctly harder than equiaxed α grains.

This section presents a numerical study on the usefulness of high fidelity microstructure representation of bimodal α-β Ti-6Al-4V and finite element modeling in better understanding the influence of microstructural features on material's strength. A core objective is to provide reliable prediction of the mechanical properties for newly designed structural alloys Ti-6Al-4V. The methodology provided in this work consists of the construction of complex and high fidelity representation of microstructures including fine geometric details from EBSD characterization data. In this method, microstructural features of interest are allowed to be altered independently to generate virtual samples and desirable crystallographic orientations

such as Burgers orientation relationship are allowed to be enforced. A deformation mechanism is conveniently introduced into the constitutive model to improve the model's ability to produce numerical results which is consistent with experimental observations. The simulations demonstrated that:

- The simulated yield strength is observed to be governed by the size of equiaxed α grain and lamellar colony. The yield strength increases as the size of grains/colonies decreases. Inclusion of β lamellae tends to increase the yield strength. The more lamellar colonies are contained in the Ti-6Al-4V, the higher yield strength the material shows. The enforcement of Burgers orientation relationship between the crystallographic orientation of α and β lamellae softens the material. Lamellar width has little effect on the yield strength. But the presence of α/β phase interfaces plays an important role in strengthening the lamellar colonies.

- Inspection of local deformation shows that the mechanical behavior of equiaxed α grains and lamellar colonies are significantly influenced by the crystallographic orientation. For lamellar colonies, c-axis is still the stiffest orientation. Mechanical constraints between α and β lamellae greatly depend on the α/β phase interfaces and are closely linked to the crystallographic orientation.

- It's improper to neglect the influence of α/β phase interfaces on mechanical properties of lamellar colonies in the simulations using high fidelity microstructure representations. Otherwise numerical results which are counterintuitive to experimental observations may be obtained.

Chapter 5 Crystal plasticity study of cyclic deformation behavior of HS CP-Ti

5.1 Introduction

The harmonic structured CP-Ti exhibited superior mechanical properties as compared to its homogeneous fine-/coarse-grained counterparts. In recent years, Ameyama and coworkers have successfully applied the bimodal design concept to processing harmonic structured CP-Ti and its alloys (Ameyama et al., 2012; Ciuca et al., 2013; Ota et al., 2014). A great effort has been made on the experimental characterization of the effects of processing routes on their structure and was limited to the creation of harmonic structured CP-Ti and evaluation of its mechanical properties (Wang et al., 2002; Witkin et al., 2003; Han et al., 2005; Billard et al., 2006). High strength without ductility loss has been reported for CP-Ti under monotonic tensile loading at room temperature (Vajpai et al., 2016).

In contrast to the considerable experimental effort, only few modelling works have been performed in the literature related to titanium alloys with harmonic structure (Vajpai et al., 2016; Liu et al., 2018; Orlov et al., 2020). Vajpai et al. (2016) built a specific representative volume element (RVE) around a core of a HS titanium by using the finite element (FE) method. In the work of Liu et al. (2018), a polycrystalline multi-scale approach was used to construct a FE plasticity-damage model of the pure HS titanium. Orlov et al. (2020) presented a simple yet powerful phenomenological model to evaluate strain partitioning between coarse- and ultrafine-grain structure components in HS materials and to estimate the magnitude of back-stress forming at their interphases. Their analysis using this model has shown that HS promotes a favorable strain partitioning between CG and UFG phases and the build-up of back-stress in the vicinity of their interfaces. Moreover, these preliminary studies focused essentially on the material response under monotonic tensile loading. To the authors' knowledge, the mechanical behavior of this class of materials under cyclic loading, which govern the fatigue resistance of the materials, have not been thoroughly investigated so far.

In this chapter, the mechanical response of the harmonic structured CP-Ti under monotonic and cyclic shear loading was investigated. Monotonic shear tests and cyclic shear tests with imposed increasing strain amplitudes were carried out for

coarse-grained and harmonic structured samples. The experimental data were used to justify the numerical model and to identify some material parameters. Then a constitutive model was established on the basis of crystal plasticity. To predict the size-dependent properties of the grains, the Hall-Petch relationship was explicitly introduced into the hardening laws. The hardening laws were implemented to a finite element numerical model. Due to the large amount of grains in the shell and core regions, direct meshing of the polycrystal grains is not feasible. In order to overcome this difficulty, a multiscale approach incorporating a scale transition rule- 'β-rule' for polycrystals proposed by Cailletaud (1987, 1992) was used. More details about the can be found in Appendix A. The localization-homogenization technique within the multi-scale approach allows building a macroscopic RVE including a large number of core regions and dealing with it in the frame-work of the multiscale scheme. Afterwards, this numerical model was applied to simulate the CG and HS CP-Ti samples under monotonic and cyclic shear loading. Finally, the numerical results were compared with the experimental data. Accordingly, the accuracy, the performance as well as some mechanical implications of the proposed numerical model were discussed.

5.2 Simulation methods

5.2.1 General consideration

In the field of numerical modelling of polycrystalline metals, the majority of the numerical works conducted so far in literature make use of the crystalline plasticity finite element method (CPFEM), which studies the heterogeneous mechanical response by considering the polycrystalline material as aggregates of individual grains. This results in cumbersome numerical work in considering the local constitutive equations and the crystal orientation for every single grain.

However, this method can no longer be used for modelling the harmonic structured CP-Ti. In fact, meshing every single grain located in both fine-grained and coarse-grained phases in three dimensions is an inefficient technique for harmonic structure due to the significant difference of the bimodal grain sizes. This difficulty can be overcome by using the so-called multi-scale models, which make the computational work significantly reduced and the 3D simulation of harmonic structured CP-Ti feasible. The multiscale approach used in the present work is

inspired by the works of Cailletaud (1987, 1992), Pilvin (1990), Abdul-Latif and Saanouni (1994), Liu et al. (2018).

The multi-scale modeling scheme is shown in Fig. 5.1. At *macroscopic level*, a finite element model is built to represent the harmonic structure. The coarse-grained regions (cores) and the fine-grained regions (shells) are separately meshed by using the Voronoi tessellation technique. The macroscopic stress field is calculated at this macroscopic scale. Then at *mesoscopic level,* a RVE including a large number of grains is built at each Gauss point of the elements. At this level, the macroscopic stresses are localized to each grain following a specific rule named the β-rule. Finally, at *microscopic level,* all the slip systems in a grain are considered in order to evaluate the plastic strain rate by using the crystal plasticity theory. The macroscopic strain velocity can therefore be calculated by using a homogenization technique.

Macroscopic (element level)	Mesoscopic scale (at each Gauss point)	Microscopic scale (in each grain)

FE model built by using the Voronoi tessellation. Core and shell regions are separately	RVE with 50-100 grains included. The grain size and the crystal orientation were	Crystal structure: Slip families, slip planes and slip directions.
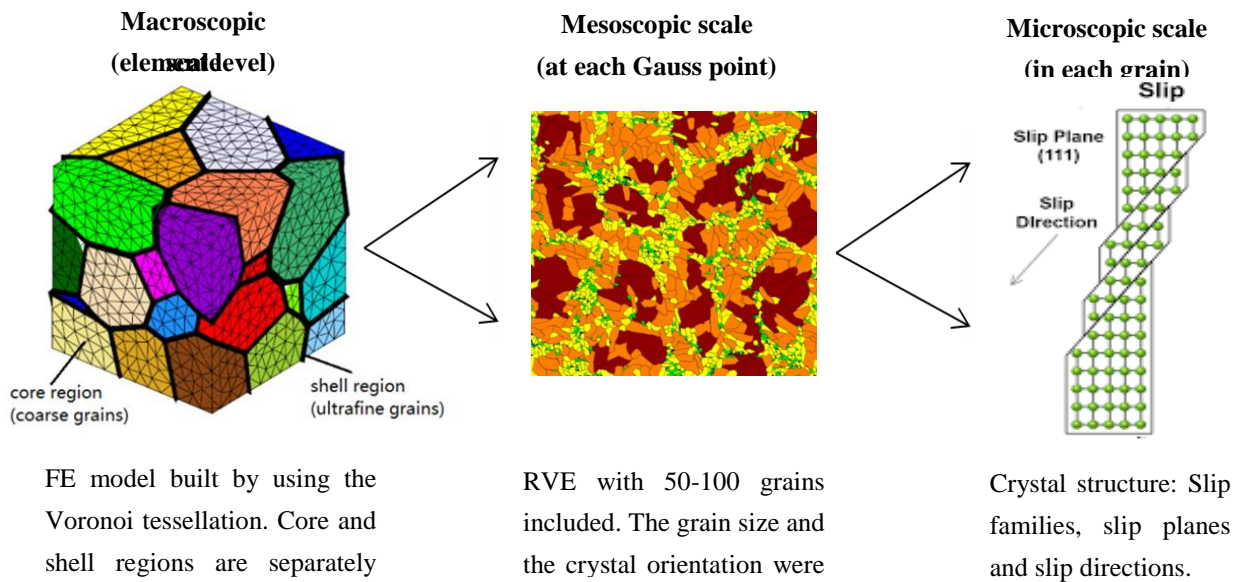
Fig. 5.1: Images showing the multi-scale modelling scheme.

5.2.2 Constitutive model

Macroscopic constitutive relation

For the sake of simplicity, it's assumed that the linear elastic constitutive relation is applied to the macroscopic finite element model. Then the second Piola-Kirchhoff stress tensor $\boldsymbol{T}$ could be evaluated by means of the elastic part of the Green-Lagrange strain tensor $\boldsymbol{E^e}$ according to their work conjugation relatioship:

$$\boldsymbol{T} = \boldsymbol{C}\boldsymbol{E^e} = \boldsymbol{C}(\boldsymbol{E} - \boldsymbol{E^p}) \tag{5.1}$$

where C is the elasticity stiffness tensor, E is the total Green-Lagrange strain and E^p is its plastic part.

The Cauchy stress tensor could be deduced by using the following relationship:

$$\boldsymbol{\sigma} = \frac{1}{det \, \boldsymbol{F}} \boldsymbol{FTF^T} \qquad (5.2)$$

where $\boldsymbol{F}$ is the deformation gradient tensor. The plastic strain tensor $\boldsymbol{E^p}$ will be determined by applying the crystal plasticity theory in a microscopic scale and by using a micro-macro transformation model.

Localization at the granular level and CSS level

As there are many fine grains in the shell regions and much fewer coarse grains in the core regions, direct finite element meshing of every single grain is not an efficient technique. In this work, a localization-homogenization procedure proposed by Cailletaud (1987) is applied to overcome this difficulty. We consider a RVE at each Gauss point of the finite elements including a sufficiently large number of grains. We first calculate the plastic strain in each grain by using the crystal plasticity theory. The average plastic strain at the corresponding Gauss point is then estimated by homogenization.

In order to determine the plastic strain at the granular level, we need to estimate the stress state in each grain through a localization procedure. Determination of the applied stress at the granular level and the slip system level could be conducted respectively through two successive steps of localization.

First, localization of the macroscopic stress tensor σ in the grain level can be realized by using a self-consistent method (Berveiller and Zaoui, 1979; Weng, 1981; Cailletaud, 1987, 1992). In this study, the so-called "β-rule", which was proposed by Gailleteau (1987) and modified by Pilvin (1990), is used. According to the "β-rule", the granular stress tensor $\boldsymbol{\sigma^g}$ can be estimated as follows:

$$\boldsymbol{\sigma^g} = \boldsymbol{\sigma} + C^g \left[\sum_{g=1}^{G} f^g \boldsymbol{\beta^g} - \boldsymbol{\beta^g} \right] \qquad (5.3)$$

where G is the number of the grains in the RVE at each Gauss point; C^g is a material coefficient representing the modulus of the intergranular kinematic hardening; f^g is the granular volume fraction of each grain; $\boldsymbol{\beta^g}$ is a variable measuring the inter-granular kinematic hardening and its expression is given by the following differential equation:

$$\dot{\boldsymbol{\beta}}^g = \dot{\boldsymbol{E}}^{gp} - C_\beta \boldsymbol{\beta}^g \sum_{i=1}^{tot} |\dot{\gamma}^i| \qquad (5.4)$$

where C_β is a material constant; $\dot{\boldsymbol{E}}^{gp}$ is the granular plastic strain rate and will be evaluated by means of the crystal plasticity.

Based on the first step of localization, the granular stress could be localized to all the slip systems of the grain to obtain the resolved shear stresses, which could be regarded as the driving force for plastic slip on the CSS.

For each slip system i, whose slip direction vector and slip plane normal vector are $\boldsymbol{S}^i$ and $\boldsymbol{M}^i$ respectively, the corresponding resolved shear stress (driving force or CRSS) τ^i can be calculated as:

$$\tau^i = \boldsymbol{\sigma} : \boldsymbol{m}^i \qquad (5.5)$$

with

$$\boldsymbol{m}^i = \frac{1}{2}\left(\boldsymbol{S}^i \otimes \boldsymbol{M}^i + \boldsymbol{M}^i \otimes \boldsymbol{S}^i\right) \qquad (5.6)$$

Crystal plasticity model at the CSS level

In this work, the following yield function for each CSS is chosen:

$$f^i = \left|\tau^i - \chi^i\right| - R^i - k^i \qquad (5.7)$$

where the exponent i denotes the slip system; χ^i is the back stress, k^i is the initial value of the critical resolved shear stress with R^i being its evolution, respectively. For the sake of simplicity, the interaction of isotropic hardening between different slip systems is neglected. Plastic slip can occur only when the function f^i is positive. The flow rule of hyperbolic form, proposed by Méric and Cailletaud (1991), is used to obtain the plastic slip rate $\dot{\gamma}^i$ of the slip system i:

$$\dot{\gamma}^i = \dot{\gamma}_0 \langle \frac{f^i}{D^i} \rangle^m sgn\left(\tau^i - \chi^i\right) \qquad (5.8)$$

where $\dot{\gamma}_0$ denotes the reference shearing rate, D^i is the drag stress representing the slip resistance, m describes the strain-rate sensitivity, $sgn\left(\tau^i - \chi^i\right)$ represents the direction of plastic flow. Slip activity can only appear when the stresses are above the threshold for all slip systems.

As mentioned above, the non-linear kinematic-isotropic hardening rule is used to describe the complex cyclic hardening of both harmonic structured CP-Ti and its coarse-grained counterpart. The main advantage of the non-linear kinematic hardening rule is its ability to better represent the non-linear stress-strain evolution

and to model the Bauschinger effects (Koiter, 1969). The back stress evolution law used in the present work has the following form:

$$\dot{\chi}^i = B\dot{\gamma}^i - C\chi^i|\dot{\gamma}^i| \tag{5.9}$$

Chaboche (1989) pointed out that isotropic hardening is the main factor governing the cyclic hardening. The isotropic hardening rate $\dot{R}^i$ of the slip system i can be related to the plastic slip rate $|\dot{\gamma}^i|$ as follows (Chaboche, 1989):

$$\dot{R}^i = a(Q - R^i)|\dot{\gamma}^i| \tag{5.10}$$

where Q denotes the saturating value of the isotropic hardening variable R^i, a is a parameter related to the number of cycles needed for the saturation of R^i. Integrating the above equation with the initial value $R^i(t = 0) = 0$ gives:

$$R^i = Q(1 - e^{-b\gamma^i}) \tag{5.11}$$

with
$$\gamma^i = \int_0^t |\dot{\gamma}^i| dt, \tag{5.12}$$

where γ^i is the accumulated plastic slip strain of the slip system i.

The threshold stress k^i is closely related to the free slip length of each slip. Thus a Hall-Petch type relationship is used to assess the scale effects:

$$k^i = k_0(1 + k_y(d^i)^{-0.5}) \tag{5.13}$$

where k_0 is a referential critical resolved shear stress, k_y is fixed coefficient. d^i is the characteristic microstructure length, d^i denotes the grain sizes of the equiaxed α grains.

5.2.3 Global algorithm

The above-described constitutive formulations were implemented numerically into the finite element code Cast3M developed by the French Alternative Energies and Atomic Energy Commission within the framework of large deformation by using a user-defined material subroutine (UMAT) written in Fortran. The external displacement-controlled loads are applied incrementally. Equilibrium is required at each loading step. The global algorithm is briefly listed as follows:

1. At each incremental loading step, resolve the macroscopic incremental elastic problem by taking the plastic strain of the previous step into consideration, and then calculate the stress fields;

2. At each Gauss point, consider a fictive RVE including a large number of grains. For each grain, evaluate the granular stress from the macroscopic stress by using the *β*-rule localization technique;

3. At each slip system, calculate the plastic slip rate;

4. Calculate the plastic strain velocity in each grain then at each Gauss point by using the homogenization technique;

5. Recalculate the macroscopic stress by taking the updated plastic strain into account until the convergence.

5.3 Finite element modeling

5.3.1 Slip systems

For the CP-Ti with hexagonal close-packed (HCP) crystal structure, the model used will take into account totally 24 slip systems which could be classified into 4 slip families, as illustrated in Table 4.1. Previous experimental observations showed that the activation of the three slip families (Basal, Prismatic, Pyramidal <a>) can be achieved more easily than that of the other two slip families (Pyramidal <a+c>/A, Pyramidal <a+c>/B) at room temperature (Zaefferer, 2003; Bridier et al., 2005; Knezevic et al., 2013). Their observations are consistent with the values of material parameters related to different slip families, identified by Barkia (2014). From investigations carried out so far, twinning "inhibition" seems to be a specificity of harmonic structures, as shown in a recent report (Dirras et al., 2017). Moreover, it is known that a reduction of the grain size inhibits twinning in hexagonal materials (thus we do not expect twinning to occur in grains in the fine-grained regions). According to a microstructural study of the deformation substructure induced by quasi-static tensile loading of harmonic titanium. It is clearly shown that the fraction of the twins is of the order of 6% against more than 70% of GNDs (represented by the LAGBs). Therefore twinning can be neglected in the present case. In the present work, the grain boundary sliding is also not considered.

5.3.2 Parameter determination

To simulate the performance of coarse-grained CP-Ti and harmonic structured CP-Ti, a number of model parameters were introduced into the proposed constitutive formulations to fulfil the description of the mechanical properties at macroscopic,

mesoscopic and microscopic scales. As CP-Ti is widely used in industrial applications and well-studied in technical literature, some of these parameters were available in previous works. Only a limited number of parameters need to be identified in the present work.

Table 5.1

Model parameters used in this work.

Parameter	Value	Parameter	Value
D^{basal}(MPa)	353	m	50.0
D^{prism}(MPa)	397	$\dot{\gamma}_0(s^{-1})$	0.001
$D^{pyr<a>}$(MPa)	441	Q(MPa)	207.0
$D^{pyr<c+a>}$(MPa)	503	a	14.5
E(GPa)	106.0	B(MPa)	815.0
ν	0.3	C	10.0
k_0(MPa)	40.7	C_β(MPa)	65.5
$k_y(\mu m^{0.5})$	4.4	C^g(GPa)	45.0

The value of Young's modulus measured according to our experiments is akin to that in the work (Simmons et al., 1971; Seagle, 1997). The approximate value of k_y was first determined by referring to that reported in (Liu et al., 2019) in which they identified the parameter as 3.8 based on experimental studies presented in (Naka and Lasalmonie, 1983; Naka et al., 1988). By fitting the yield strength of monotonic shear tests for CG CP-Ti and HS CP-Ti samples, a new value for k_y which was readjusted from the approximate value and the value of k_0 were estimated. Afterwards, these two parameters were tested again and slightly changed by fitting the cyclic shear test. The values of $\dot{\gamma}_0$ and m in the flow rule were gathered from different literatures, i.e., from the work of Kasemer and colleagues (2017) for Ti-6Al-4V and from the study (Hama et al., 2017) for CP-Ti, respectively. Parameters related to isotropic hardening and kinematic hardening, namely *C, B, Q* and *a*, were calibrated by fitting the monotonic hardening and cyclic hardening of homogeneous CG specimens for CP-Ti. The values of the slip strengths D^i for different slip systems were determined by referring to the work of Song and colleagues (2008) and akin to those listed in the articles (Yang et al., 2011). The values of parameters C^g and C_β were determined by referring to Barkia's work (2014) which was based on his experiments about single

crystal titanium. Then all the parameters above-estimated were tested again by fitting the entire cyclic responses. The final parameters used in the present work are listed in Table 5.1 for both coarse-grained CP-Ti and harmonic structured CP-Ti.

5.3.3 Finite element model tests

Finite element model tests for homogeneous CG and HS CP-Ti are performed to investigate the reliability of the proposed numerical model. These model tests are all based on the monotonous simple shear experiments described in Section 3.1 and Section 3.2. The boundary condition is schematically shown in Fig. 5.2, where the planned displacements are imposed on all surfaces of RVEs.

Finite element models were constructed for coarse-grained CP-Ti and harmonic-structured CP-Ti. For coarse-grained CP-Ti, a representative volume element (RVE) containing a sufficiently large number of grains was built as shown in Fig. 5.3a. In the present work, the Voronoi tessellation technique was used to generate tetrahedral elements according to the statistical distributions on grain size and grain orientation obtained in the Section 3.1.

For harmonic-structured CP-Ti, a 3D RVE was built with a sufficiently large number of core regions, as shown in Fig. 5.3b. The volume fraction of the shell region was controlled by its "thickness" between two neighboring cores. Here again, the Voronoi tessellation technique was used to generate tetrahedral elements in both the core and shell regions. The size of the core regions is equal to size of the titanium powders, ranging from 100 to 180µm.

ABFE and DCGH:
$$u_x = \Delta l \cdot z$$
$$u_y = u_z = 0$$

ABCD:
$$u_x = \Delta l$$
$$u_y = u_z = 0$$

EFGH:
$$u_x = u_y = u_z = 0$$
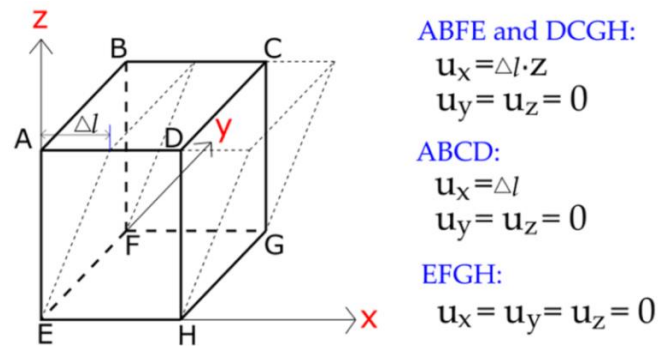
Fig. 5.2 Illustration of the boundary conditions of simple shear loading used in this work.

To reasonably represent the mechanical properties of a polycrystalline material, namely the coarse-grained CP-Ti and harmonic structured CP-Ti in this work, a series of simulation tests were performed to determine the optimal RVEs (size, number of grains or core regions etc.). This allows us to minimize the computational work

without sacrificing significantly its reliability.
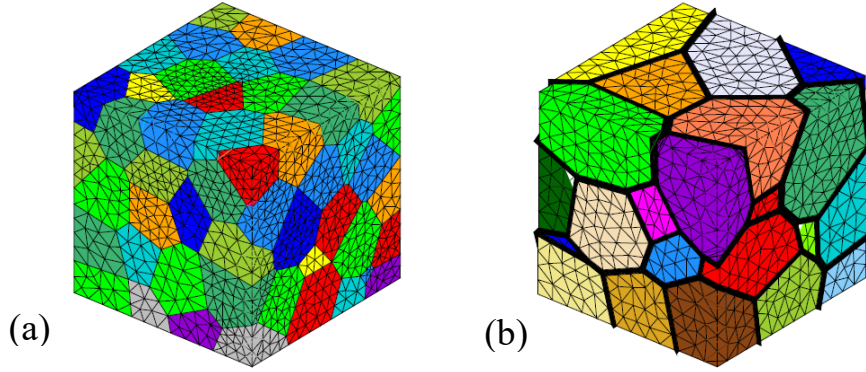
Fig. 5.3 Illustration of the RVEs corresponding to (a) coarse-grained CP-Ti, where each colour represents a single grain and (b) the harmonic structured CP-Ti, where the coloured parts represent the core regions and the black part represents the shell regions.

With respect to the simulations of coarse-grained CP-Ti, three RVEs, with 50, 100 and 200 single crystal grains respectively, were built for the simulation tests, as shown in Fig. 5.4. These finite element models were subjected to monotonic shear loading up to Γ=10.0% of the overall shear strain. The simulated overall strain-stress responses are plotted in Fig. 5.5. From this figure, we can see that only very small differences exist among the results. We can confirm that the accuracy of the FE model is sufficient when the number of grains reaches 100, as the overall stress-strain curve of models with 100 grains is very close to that with 200 grains.

For the harmonic structured CP-Ti, the accuracy of the finite element models depends on two parameters. The first one is the number of the core regions in the RVE, denoted by Nc. The second is the number of grains considered at each Gauss point, denoted by Ng. We first consider the influence of Nc by building three RVEs with Nc=30, 50 and 100 respectively, as shown in Fig. 5.6. By fixing Ng=30, numerical tests were performed for monotonic simple shear up to Γ=10.0% of the overall shear strain. The simulation results (see Fig. 5.7) show that there is no significant difference on the overall stress-strain curves when using the three RVEs. Even though the accuracy seems to be well achieved with the RVE of 50 cores, it is fairly acceptable with the RVE of 30 cores. Consequently, considering the heavy computational work in 3D crystal plasticity simulations under cyclic loading condition, the number of core regions contained in the FE model is chosen as 30 without significant sacrifice of accuracy (see Fig. 5.7).

Consider now the influence of the parameter Ng, the number of grains

considered at each Gauss point, by using the RVE of 30 cores. We carried out numerical tests with *Ng*= 20, 30 and 50 respectively. The simulation results presented in Fig. 5.8 show that the good accuracy on the overall stress-strain curves is obtained with all these *Ng* values. In the present work, the number of grains considered at Gauss points is chosen to be 30.
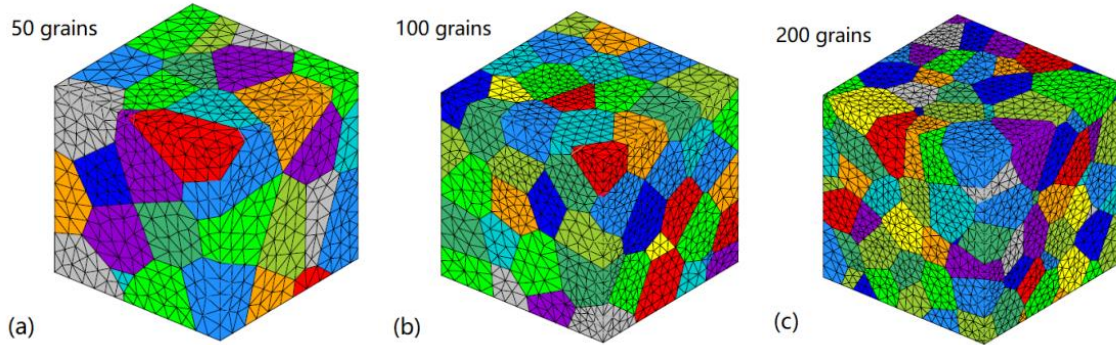
Fig. 5.4 Polycrystalline meshes of RVEs with (a) 50, (b) 100 and (c) 200 single crystal grains for the coarse-grained CP-Ti.
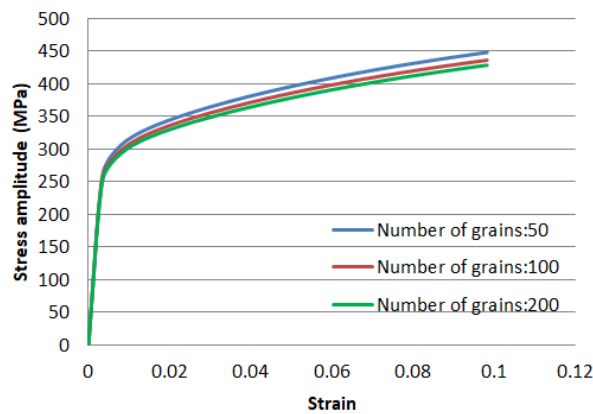
Fig. 5.5 Effect of the number of grains included in a RVE on the overall stress-strain response of CG CP-Ti under monotonic shear loading.
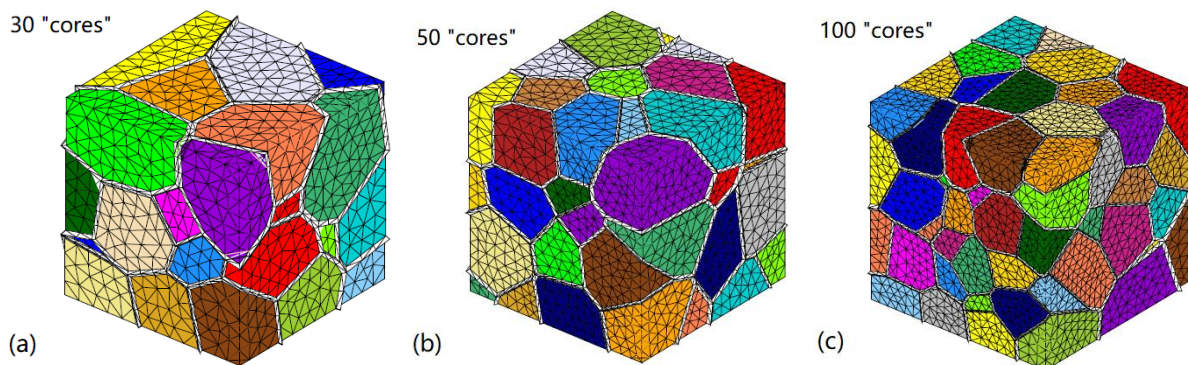
Fig. 5.6 Polycrystalline meshes of RVEs with (a) 30, (b) 50, (c) 100 core regions for the harmonic structured CP-Ti.

As mentioned above, the grain orientations are considered as randomly distributed. For the coarse-grained CP-Ti, every single grain has a randomly generated orientation defined by the Euler angles, which are theoretically different from each other. However, for the harmonic structured CP-Ti, an identical set of randomly distributed orientations (30 in this work) is assigned to all the Gauss points within a same core or shell. Different sets of orientations are assigned to different cores and shells.
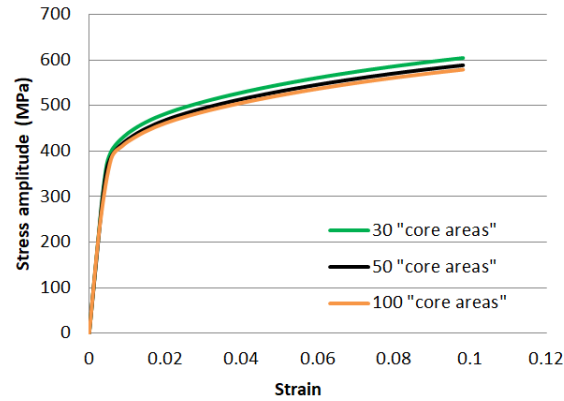
Fig. 5.7 Effect of the number of coarse-grained regions included in a RVE on the overall stress-strain response of HS CP-Ti under monotonic shear loading.
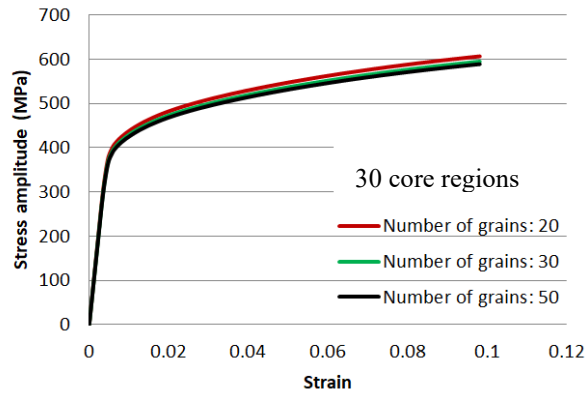
Fig. 5.8 Effect of the number of grains considered at a Gauss point on the overall stress-strain response of HS CP-Ti under monotonic simple shear loading.

Due to the lack of existing approach to generate finite element mesh for harmonic structured materials, authors developed an algorithm based on the Voronoi tessellations. The developed algorithm is able to construct many random coarse-grained regions surrounded by an interconnected 3D network of fine-grained regions whose thickness can be easily changed to control the volume fraction. However, the drawback of the developed algorithm is the faces of the generated RVE are slightly uneven. But in this work, homogeneous strain boundary conditions are

imposed on the contour of the mesh by a displacement vector (in the form of $u_i = \varepsilon_{ij} r_j$), the generated RVE with slightly uneven faces is assumed to be an acceptable approximation of the realistic microstructure.

5.4 Numerical results and discussions

5.4.1 Response to monotonic shear loads

The simulated overall stress-strain response for coarse-grained CP-Ti and harmonic structured CP-Ti under monotonic shear loading are shown in Fig. 5.9a, compared with the experimental results. In order to demonstrate the advantage of harmonic structure design, simulations for these two CP-Ti are presented in a single figure. From this figure, we can confirm that the harmonic structured CP-Ti possesses much higher strength with acceptable loss of ductility compared with the coarse grained CP-Ti. The harmonic structure design is capable of achieving improved performance on strength-ductility combination. Moreover, it is obvious that the model simulations agree well with the test data under monotonic loading condition.

Fig. 5.9b shows the simulated evolution of rate of hardening (the slope of stress-strain curve) within the strain amplitude of 5.0%. The figure exhibits three distinct deformation stages. The first stage is approximately a section of horizontal line representing the elastic response. It's clear that, for the harmonic structured CP-Ti and the coarse grained CP-Ti, their values of elastic moduli are the same but the former has a longer period of elastic deformation stage. Consequently, the macroscopic yield stress of HS CP-Ti is much higher than that of CG CP-Ti, which is caused by the higher critical resolved shear stress of ultrafine grains (grain size effect) and numerically described by means of the Hall-Petch law. In stage 2, with the emergence of plastic slip, the rate of hardening decreases rapidly at first, then it gradually slows down and almost becomes horizontal again. Dislocations glide in intersecting planes and interact with each other, obstructing further plastic slip. The two evolution curves of rate of hardening behave similarly. In stage 3, the rate of hardening remains little changed and the two curves nearly overlap. These results show that the present numerical model can faithfully describe the different deformation mechanisms of both the harmonic structured CP-Ti and the coarse grained CP-Ti under monotonic loading.
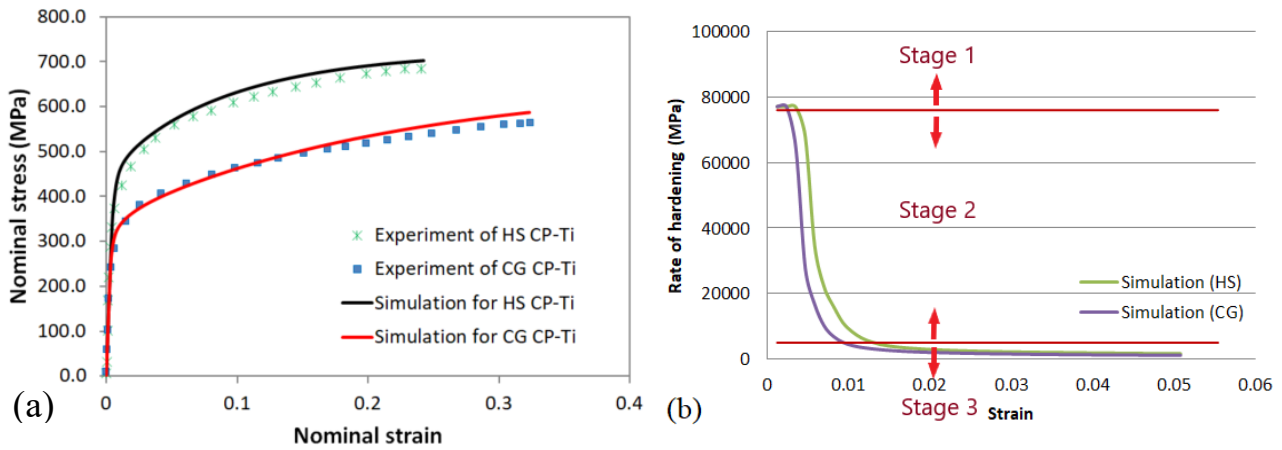
Fig. 5.9 Simulated stress-strain curves and experimental results for homogeneous coarse-grained CP-Ti and harmonic structured CP-Ti in the case of monotonic simple shear condition.
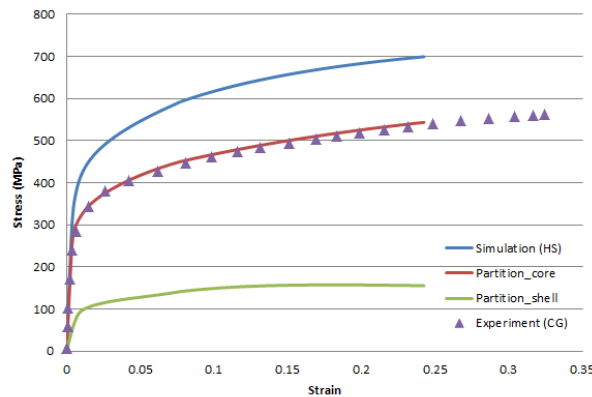
Fig. 5.10 Partition of the overall stress in HS CP-Ti and comparison with the experimental data for CG CP-Ti under monotonic shear loading.

In order to study the strengthening role of the UFG shell region in the harmonic structured CP-Ti, we split the external shear load into two parts: the part carried by the UFG shell region with 16% of volume fraction and the part carried by the CG core region with 84% of volume fraction (see Fig. 5.10). The experimental stress-strain response for CG CP-Ti under monotonic shear loading was also plotted for comparison. The figure shows that the core regions with 84% of volume fraction bear two-thirds of the total load while the shell regions with 16% of volume fraction bear almost one-thirds of the total load. Moreover, as expected, we can remark that the overall stress contributed by the core regions in the harmonic structured CP-Ti sample almost equals to the total loading stress of the CG CP-Ti sample. Consequently, we can affirm that the strengthening of HS CP-Ti is mainly contributed by the UFG shell regions.

Based on this load partition, we calculate the average effective shear stresses of

the shell regions and core regions respectively. In Fig. 5.11, we plot the ratio of the average stress in the shell regions over that in the core regions as function of the overall strain. The ratio starts from 1.0 and increases rapidly until a stabilized plateau. This high ratio is attributed to the higher initial yield stress of the shell regions. Then it drops slowly, which could be explained by the fact that strain hardening reaches in saturation in the shell regions earlier than in the core regions.
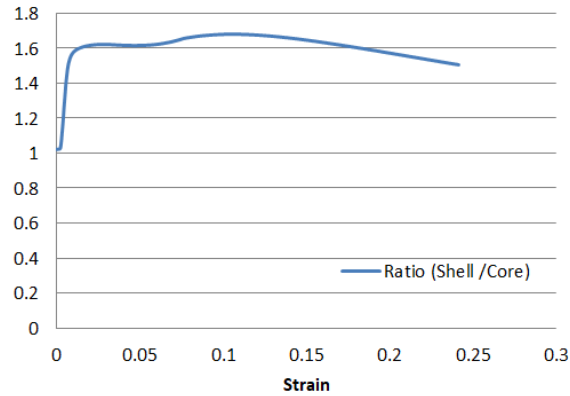
Fig. 5.11 Evolution curve of the ratio of the average effective stress in shell regions over that in core regions.

In order to illustrate the strengthening effect of the shell regions, we display the effective shear stress field when the overall strain equals to 3.46% in the HS CP-Ti RVE in Fig. 5.12. From Fig. 5.12, we can clearly observe the sharp contrast between the stress distribution in the shell regions and that in the core regions.

Fig. 5.13 shows the shear strain field at the overall strain level Γ=6.93%. Opposite to the stress distribution, the strain concentration emerges in the core regions rather than in the shell regions. This kind of deformation behaviour displayed in the simulations is consistent with the experimental observations. Park et al. (2018) quantitatively investigated the deformation behaviour in SUS304L steel with harmonic structure by using micro-digital image correlation (micro-DIC) and observed the concentrated strain distribution in the CG core region. Witkin et al. (2003) and Fan et al. (2006) also observed this deformation behaviour in Al-Mg alloy with bimodal grain-size distributions.

The numerical simulations illustrate the main mechanism of the strengthening effect of the harmonic structure design. The shell regions form a thin but hard skeleton enveloping the massive and soft core regions. Consequently, they can bear an important part of external load and undergo large deformation, resulting in a higher strength without obvious loss of ductility for the HS CP-Ti.
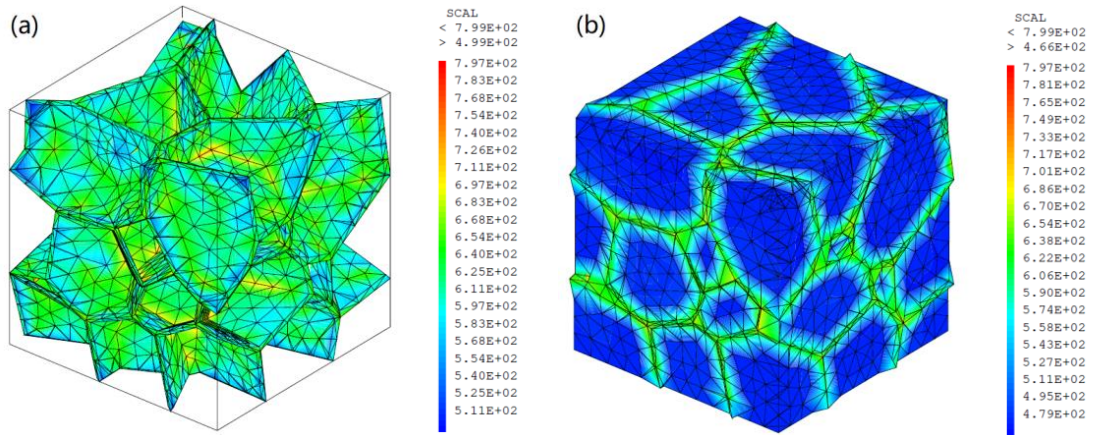
Fig. 5.12 Effective shear stress fields at the overall strain $\Gamma= 3.46\%$ (a) in the shell regions and (b) in the whole RVE.
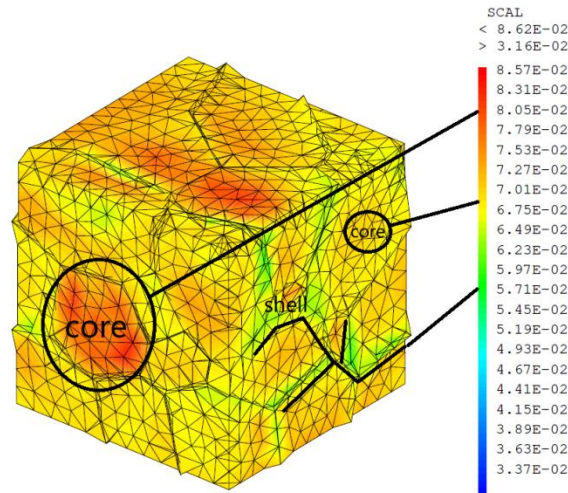
Fig. 5.13 Effective shear strain field at the overall strain $\Gamma=6.93\%$ in the HS CP-Ti RVE.

5.4.2 Response to cyclic shear loads

The numerical cyclic shear simulations with imposed increasing strain amplitudes were performed for coarse-grained CP-Ti and harmonic structured CP-Ti. The increment of the overall strain amplitudes is $\Delta\Gamma=1.155\%$ per cycle. In Fig. 5.14, we compare the simulation result and the experiment data on overall stress-strain response for harmonic structured CP-Ti with $\Delta\Gamma=1.155\%$ per cycle. From this figure, we can remark that the simulated cyclic response agrees well with the experimental data.
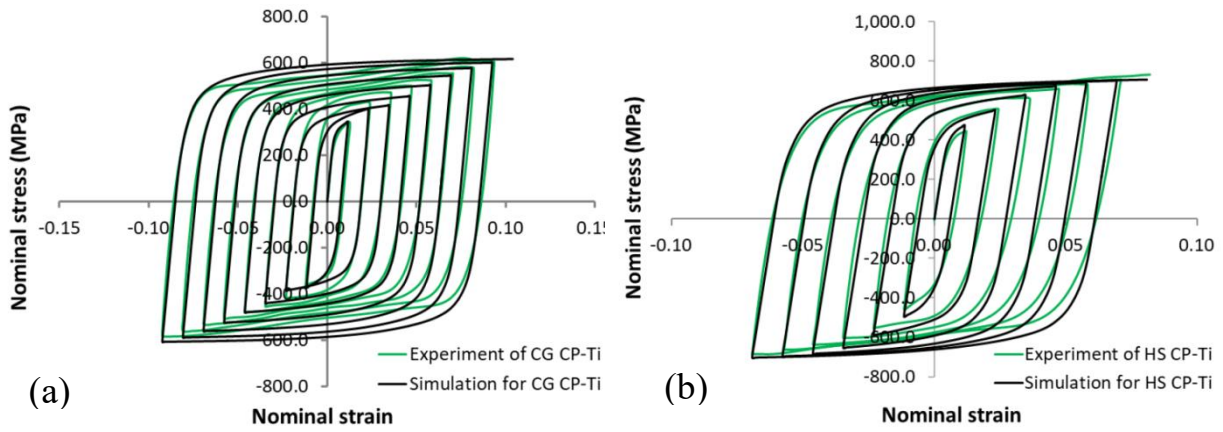
Fig. 5.14 Simulated curves and experimental results for (a) homogeneous coarse-grained CP-Ti and (b) harmonic structured CP-Ti in the case of cyclic simple shear condition when ΔΓ = 1.155% every cycle.

In Fig. 5.15, we plot the test-simulation comparisons for a selected hysteresis loop, namely the 1st cycle for ΔΓ=1.155 for both the CG CP-Ti and HS CP-Ti. Such a choice facilitates the comparison of the material behaviour under the loading condition. From these figures, we can confirm that the plasticity behaviour, including the plastic hardening and the Bauschinger effect were well captured by the proposed numerical model.
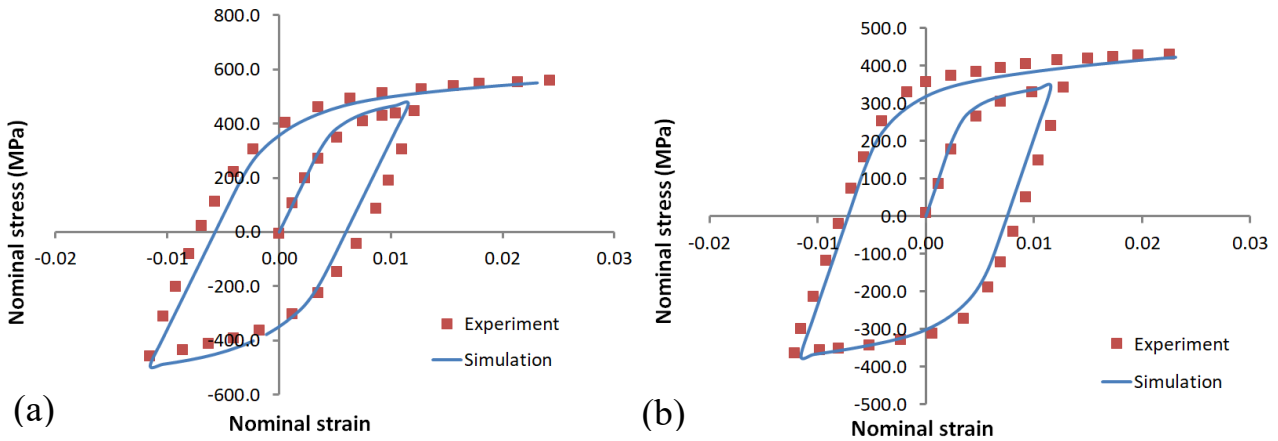
Fig. 5.15 Comparison of simulated hysteresis loop and experimental data for the first cycle under cyclic shear loading with ΔΓ=1.155%: (a) HS CP-Ti, (b) CG CP-Ti.

To describe the cyclic hardening behaviour, Fig. 5.16 illustrates the evolution of the overall stress amplitude versus the number of cycles (Lin et al., 2010) for the two kinds of CP-Ti with the prescribed incremental strain amplitude. Meanwhile, the experimental data were also plotted to show the good match with the simulations. Fig. 5.16 shows that the cyclic stress amplitude of HS CP-Ti is much higher than that of

CG CP-Ti. From the figure, we can observe the following properties. First, the HS CP-Ti has higher initial yield strength comparing with the CG CP-Ti. This property is attributed to the higher critical resolved shear stress of the shell regions. Second, the HS CP-Ti needs fewer cycles to reach the hardening saturation. This property is also attributed to the reinforcing effect of the shell regions in which the critical resolved shear stress saturates more quickly. All these effects can efficiently be captured by the proposed model.
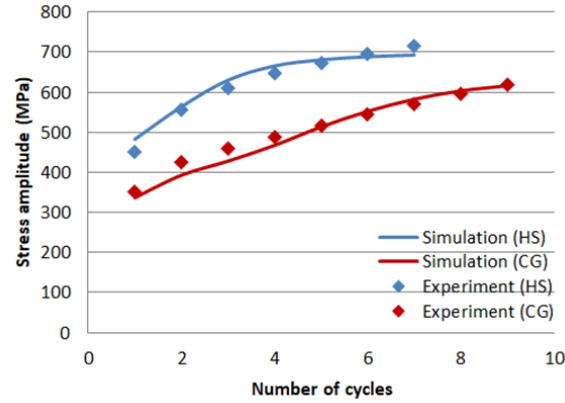
Fig. 5.16 Comparison of simulated cyclic hardening and experimental data for CG CP-Ti and HS CP-Ti with ΔΓ=1.155%.
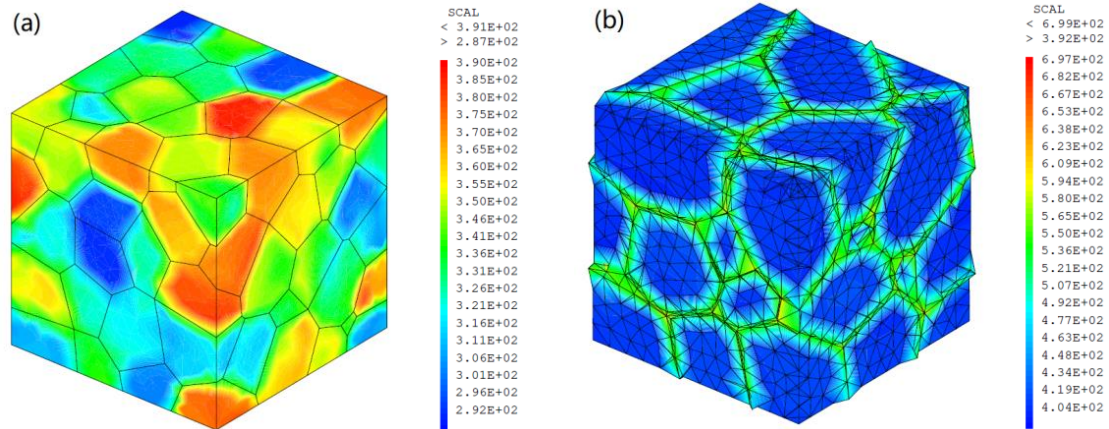
Fig. 5.17 Effective shear stress distribution at the overall strain Γ= 1.155% for (a) CG CP-Ti and (b) HS CP-Ti, with ΔΓ=1.155%.

Figs. 5.17 and 5.18 show the shear stress and strain fields under cyclic shear loading at the overall strain Γ=1.155% with ΔΓ=1.155% for both the CG CP-Ti and HS CP-Ti RVEs. From these figures, we can remark that the stress and strain distributions in the CG CP-Ti RVE are relatively homogeneous compared to those in the HS CP-Ti RVE. The stress concentration in the ultrafine grained shell regions is supposed to be the consequence of the sharp contrast between the grain sizes in the

cores and shells. Conversely, the strain concentration occurs in the core regions. These results are very similar to those observed in the cases of monotonic loading.
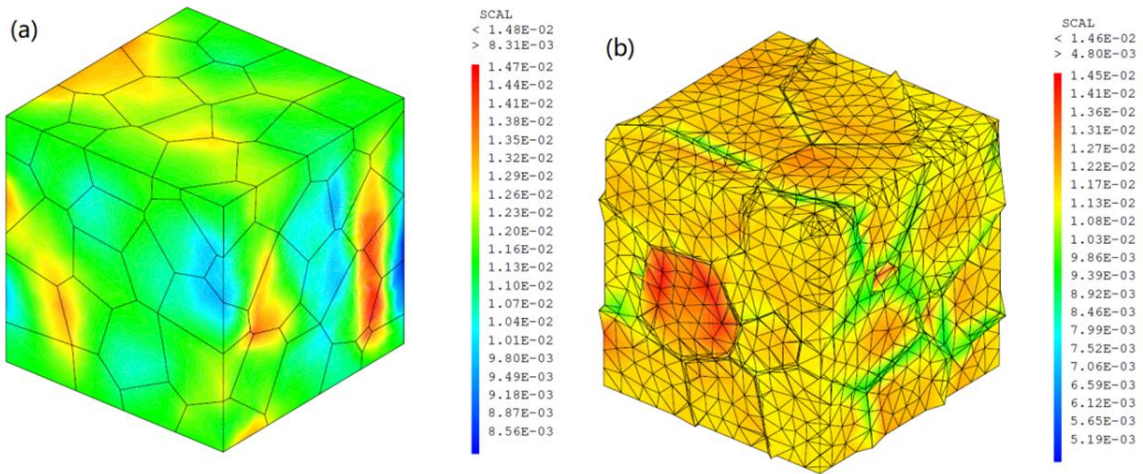
Fig. 5.18 Effective shear strain distribution at the overall strain Γ=1.155% for (a) CG CP-Ti and (b) HS CP-Ti with ΔΓ=1.155%.

5.5 Concluding remarks

In this Chapter, a slip-theory based crystal plasticity model together with a multiscale micro-macro approach was successfully established and implemented into a three dimensional finite element code. Numerical simulations were carried out for polycrystalline CP-Ti with harmonic structure and coarse grained structure respectively under monotonic and cyclic simple shear loading.

Based on these numerical simulations, following concluding remarks can be made. First, the multiscale micro-macro approach, mainly including the localization and homogenization processes across different length scales, was shown to be a reliable and efficient technique for dealing with the numerical modelling of bimodal harmonic structured CP-Ti. Second, the used non-linear kinematic hardening law and non-linear isotropic hardening law have proven its capacity to describe the non-linearity of the stress-strain evolutions and cyclic hardenings. Third, the Hall-Petch law implemented into the crystal plasticity provides satisfactory results for determining the grain size effect on the macroscopic inelastic behaviour.

The predicted macroscopic stress-strain curves agree well with the experimental data under monotonic and cyclic simple shear loading conditions for both harmonic structured CP-Ti and coarse grained CP-Ti. The strengthening effects of harmonic structured CP-Ti have been well captured by the proposed numerical model.

Chapter 6 Crystal plasticity study of cyclic deformation behavior of HS Ti-6Al-4V

6.1 Introduction

This chapter investigates and compares the deformation mechanism of harmonic structured (HS) Ti-6Al-4V alloy to that of homogeneous coarse-grained (CG) counterparts. A set of simple shear tests on homogeneous CG and HS specimens for Ti-6Al-4V was conducted under monotonic and cyclic simple shear loading conditions. Efforts have been made to extend the numerical model mentioned in Chapter 5 to simulations of HS Ti-6Al-4V. Numerical and experimental results were confronted to confirm the validity of the proposed model. To better understand the strengthening mechanisms of the HS design, comparisons between HS CP-Ti and HS Ti-6Al-4V were conducted and discussed in terms of macroscopic stress-strain response and distribution of stress/strain fields. Furthermore, influence of the volume fraction of fine-grained (FG) regions on mechanical properties of HS CP-Ti and HS Ti-6Al-4V was assessed by using the developed model. It was demonstrated that strengthening mechanisms of harmonic designed CP-Ti and Ti-6Al-4V structures are different. This result explains why the HS design induces superior strengthening effect on CP-Ti than on Ti-6Al-4V.

The general deformation mechanisms of different harmonic structured materials are still under exploration up to now. Over the past decade, considerable effort has been put into the processing and characterization of HS materials. High strength with slight ductility loss has been reported in the experimental investigation of commercial-purity titanium within monotonic tensile tests (Vajpai et al., 2016). Dirras and co-workers (2017) fabricated HS Ti-25Nb-25Zr β-titanium alloy and evaluated its mechanical properties through cyclic shear experiments in comparison with the homogeneous counterpart. For HS Ti-25Nb-25Zr, it was reported that plastic incompatibilities because of grain size difference were accommodated through accumulating GNS appearing in the FG region/CG region vicinity. Kikuchi and co-workers (2018) studied the fatigue properties of harmonic structured Ti-6Al-4V and observed an improved fatigue resistance.

It was noticed that grain sizes and volume fractions of FG/CG regions have a direct influence on mechanical properties of HS materials. Zhang and co-workers

performed research on HS SUS304L and SUS316L stainless steels (Zhang et al., 2014; Zheng et al., 2016), which depicted the dependence of material's strength and ductility on average size of all grains and the volume fraction of FG regions. The experimental study in (Vajpai et al., 2016a) on HS CP-Ti also revealed the combined effect of refined grain size and volume fraction of FG regions in material strengthening.

Inspired by the work of Kikuchi and colleagues (2018), according to which the HS Ti-6Al-4V showed a higher fatigue resistance, we carried out a similar investigation on HS Ti-6Al-4V, attempting a better strength-ductility combination under monotonous and cyclic loading. However, the mechanical tests showed that the improvement is not as significant as expected, contrariwise to the remarkable performance of HS CP-Ti. Therefore, besides microstructure specificities, the strengthening effect of the HS design should be different for these two metals.

This work is focused on understanding the general deformation mechanism of HS materials by performing numerical simulations of strengthening behavior under monotonous and cyclic simple shear loading condition for two typical materials, namely CP-Ti and Ti-6Al-4V. To this end, a new approach combining a crystal plasticity model for lamellar α+β colonies (Mayeur, 2004) with the numerical model developed for HS CP-Ti (Chapter 5) has been explored and implemented.

6.2 Crystal plasticity model for lamellar α+β colony

There are two crystallographic phases present in the α+β Ti-6Al-4V, viz. a α phase showing hexagonal close packed crystal symmetry and a β phase displaying body centered cubic crystal symmetry. In general, the β phase is experimentally observed to have a volume fraction of approximately 7%. The bimodal microstructure of $\alpha+\beta$ Ti-6Al-4V is characterized by transformed β colonies consisting of alternating α and β lamellae and equiaxed α grain.

The extension of crystal plasticity theory to multi-phase materials such as the lamellar α+β colony has met great challenges since beginning and is still an area of intensive research. The development of such models should be capable of investigating the deformation mechanisms of multi-phase materials at the crystal scale thus providing an insight into the influence of microstructures on the material properties. According to the existing literature, one of the most important issues in

developing a multi-phase model is the determination of material properties and the representation of slip geometry of the multi-phases. It should be noticed that the constituent property of each phase in a multi-phase material is generally different from the property of its single crystal form for complicated reasons. And it's very difficult to isolate a single crystal of a certain phase from the polycrystalline material and it's not realistic to experimentally measure the property of each phase. The other issue is the determination of how to consider the influence of microstructure-based deformation mechanisms on mechanical behaviors of an individual phase, such as the strengthening effect of phase interfaces and the grain boundary strengthening effect. The microstructural features such as the different slip systems in different phases, the crystalline orientation distribution and the anisotropy of slip systems all have significant influence on the deformation behavior of the multi-phase material.
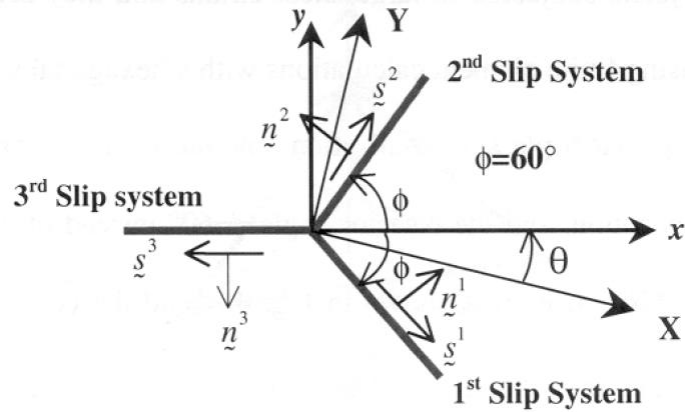
Fig. 6.1 Slip geometry of the planar triple slip model where the angle θ completely specifies the orientation of the grain (Morissey, 2001; Goh , 2002).
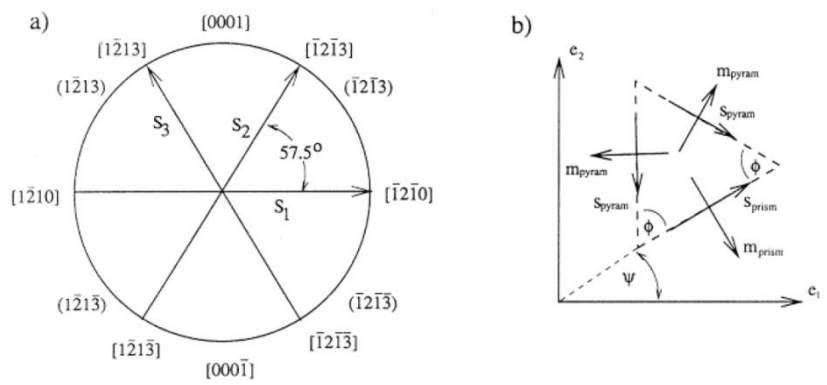
Fig. 6.2 Planar triple slip idealization used by Schoenfeld and Kad (2002).

There exist commonly two approaches to model the multi-phases in the framework of crystal plasticity. One is to model the multi-phases using homogenized slip geometries as the representation of the microstructure of the multi-phases, in

which there is no crystallographic distinction between the individual phases. The slip geometry is assumed to be the same for every grain, while the hardening parameters differ to consider the influence of anisotropy and heterogeneity of the actual material. A non-exhaustive list of the application of this approach in the study of Ti-6Al-4V includes Morrissey (2001), Goh et al. (2001), Goh (2002) and Schoenfeld and Kad (2002). For example, a 2-D planar triple slip idealization for the slip geometry can be made in which only three active slip systems equally spaced 120° apart are adopted to model the deformation solely by prismatic slip, as shown in Fig. 6.1. And as a modification of the previous model, a planar triple slip idealization in which one system represents the prismatic slip and two other systems represent the idealized pyramidal slip along the 1123 direction is proposed by Schoenfeld and Kad (2002), as shown in Fig. 6.2.

The other approach pays attention to distinguish individual phases by assigning each phase with its own set of slip systems either using the simplified 2-D slip geometry or the more realistic 3D slip systems. Generally, the slip geometry and deformation mechanism of each individual phase within the lamellar $\alpha + \beta$ colonies will be modified on the basis of experimental observations and available deformation assumptions, and therefore different from that of an isolated single crystal of the same phase. The advantage of such equivalent constitutive model is its good ability to represent the microstructure's influence on the material's mechanical response without putting considerable effort into the construction of representation of microstructures with fine geometric details. Mayeur (2004) developed a set of more realistic 3D equivalent slip geometry by extending the 2D crystal plasticity theory proposed by Morrissey et al. (2003) and Goh et al. (2003).

The 3D constitutive model by which the micro-mechanical response of lamellar $\alpha + \beta$ colonies was investigated in this work was originally developed by Mayeur (2004), who extended the idealized 2D slip theory used by Morrissey et al. (2003) and Goh et al. (2003). Compared with the highly idealized 2D slip theory, this constitutive model (Mayeur, 2004) included some attractive features such as distinct 3D slip geometry for the lamellar $\alpha + \beta$ regions, length scale dependent critical resolved shear stress (CRSS) considering the obstacle to slip transmission at phase interfaces, anisotropic slip strengths and the ability of handling a wide range of random grain orientations.

Direct meshing of such a complex microstructure must contain a great many of

grains, and therefore is extremely costly. In the present study, a 3D crystal plasticity model (Mayeur and McDowell, 2007), which can be referred as equivalent constitutive model (ECM), is adopted. The ECM integrates the slip systems of α and β phases of a laminar $\alpha + \beta$ colony into an equivalent super grain by following certain geometrical relationships, named as the Burgers orientation relation (BOR). The consequence of this lamellar structure and the BOR is that certain deformation modes are considered as "hard" when the slip directions intersect the α/β interface due to the relatively small effective slip distance and other deformation modes are considered as "soft" when the slip systems slide parallel to the α/β interface or bear parallel slip planes in both phases.

Thanks to the special microstructure of the α+β colonies and the Burgers orientation relation, the entire laminar α+β colony can be considered as a single super grain in the crystal plasticity analysis (Fig. 6.3). Inspired by the notion in the work of Goh et al. (2003), Mayeur (2004) assumed that slip systems having a slip direction intersecting the α/β interfaces are difficult to activate because of the comparatively short effective slip distance. And the threshold stresses of these slip systems belonging to the HCP slip systems and BCC slip systems are governed by α lath width and the β rib width respectively through a Hall-Petch type relation. On the contrary, slip systems which slide parallel to the phase interfaces or bear parallel slip planes in two phases are not affected by the interfaces' obstacles to slip transmission. These soft slip systems consist of three basal, one prismatic and two ⟨111⟩{110} slip systems. The corresponding threshold stresses of these soft slip systems are not governed by the microstructural length scales as the hard slip systems.
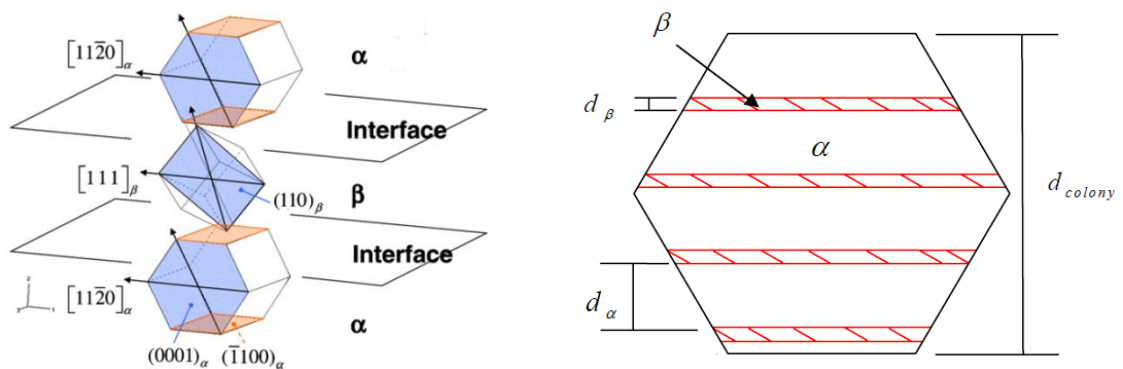
Fig. 6.3 Schematic illustrating (a) Burgers orientation relationship in lamellar α+β colonies and (b) lamellar colony length scales (Zhang et al., 2007).

6.3 Simulation methods

6.3.1 General consideration

In numerical simulations, Voronoi tessellations are regarded as an efficient method to generate random polycrystals (Barbe et al., 2001). However, direct meshing of individual grains or α+β colonies for HS Ti-6Al-4V results in a representative volume element including an extremely huge number of elements due to the huge contrast between the grain sizes in FG and CG regions, leading to thus an impractical and inefficient finite element (FE) model. To overcome this difficulty, a scale transition rule is necessary to develop a realistic 3D numerical model. In this work, an explicit self-consistent method, called 'β-rule' developed by Cailletaud (1987) and reshaped by Pilvin (1990), was employed in the numerical model as in the work presented in Chapter 5.

Another difficulty is the complex microstructure of Ti-6Al-4V with lamellar colonies. In addition to employing the high fidelity finite element modelling in which the α phase and β phase in lamellar α+β colonies are explicitly represented by using large finite element mesh (Obstalecki et al., 2014; Karsemer et al., 2017), an efficient alternative way is to construct equivalent slip geometry of multi-phase materials with the help of simplified representations of microstructures (Morrissey, 2001; Goh et al., 2001, 2003; Schoenfeld et al., 2002; Mayeur et al., 2007). However, such models are incapable of modeling the full spectrum of realistic textures that are commonly attained in Ti-6Al-4V polycrystals. The construction of a 3D constitutive model is of significant importance to study the effects of a wide range of orientation distributions, 3D slip systems and slip system anisotropy on deformation behavior. In the present study, a 3D crystal plasticity model (Mayeur and McDowell, 2007), which can be referred as equivalent constitutive model (ECM), is adopted. The ECM integrates the slip systems of α and β phases of a laminar $\alpha + \beta$ colony into an equivalent super grain by following certain geometrical relationships, named as the Burgers orientation relation (BOR). The consequence of this lamellar structure and the BOR is that certain deformation modes are considered as "hard" when the slip directions intersect the α/β interface due to the relatively small effective slip distance and other deformation modes are considered as "soft" when the slip systems slide parallel to the α/β interface or bear parallel slip planes in both phases. More details of this model can be

found in the original work of Mayeur (2004).

By using the ECM, there is no need to explicitly mesh the individual lamellae in a FE model. The global scheme of the numerical calculations is as follows:

For CG Ti-6Al-4V, polycrystalline RVEs are built by means of Voronoi's tessellation with a large number of $\alpha + \beta$ colonies. Crystal plasticity theory is used to establish the constitutive laws. Besides, polycrystalline models are also used to verify the validity of the β-rule by applying this rule to a homogeneous RVE.

For HS Ti-6Al-4V, the Voronoi tessellation technique is used for the RVE's formation. CG regions and FG regions are separately meshed. At each Gauss point, only a finite number of $\alpha + \beta$ colonies are examined in order to establish the corresponding constitutive law. The β-rule is used as a homogenization-localization procedure for macro-micro stress/strain transition.

6.3.2 Constitutive model

Since the crystal plasticity based multi-scale numerical model used to simulate the Ti-6Al-4V is essentially the same only with some specific details being different from the case of pure Titanium. To avoid repeating the description of the CPFEM which has been present in subsection 5.2.2, only the constitutive laws concerning particularly the Ti-6Al-4V case will be demonstrated here.

The threshold stress k^i is closely related to the free slip length of each slip. Thus a Hall-Petch type relationship is used to assess the scale effects:

$$k^i = k_0(1 + k_y(d^i)^{-0.5})$$ (6.1)

where k_0 is a referential critical resolved shear stress, k_y is fixed coefficient. d^i is the characteristic microstructure length. The d^i values with respect to $\alpha+\beta$ colonies correspond to either the colony size, the α lath width or the β lath width.

The main source of intergranular heterogeneity is related to a phenomenological variable $\boldsymbol{\beta}^g$ which is able to correctly capture the plastic accommodation (Cailletaud and Pilvin, 1994). The granular stress tensor σ^g is determined by:

$$\boldsymbol{\sigma}^g = \boldsymbol{\sigma} + C^g(\boldsymbol{B} - \boldsymbol{\beta}^g)$$ (6.2)

$$\boldsymbol{B} = \sum_{g=1}^{G} f^g \boldsymbol{\beta}^g$$ (6.3)

where $\boldsymbol{B}$ is the mean of variable $\boldsymbol{\beta}^g$ for all grains, g represents the equiaxed α grains

or lamellar α+β colonies, G indicates all grains (or colonies) considered at a continuum point, C^g denotes a material parameter, f^g denotes the volume fraction for every grain (or every colony). The evolution of $\boldsymbol{\beta}^g$ is calculated through a differential equation (Cailletaud and Pilvin, 1994):

$$\dot{\boldsymbol{\beta}}^g = \dot{\boldsymbol{E}}^{gp} - C_\beta \boldsymbol{\beta}^g \sum_{i=1}^{tot} |\dot{\gamma}^i| \tag{6.4}$$

where C_β denotes a material parameter, $\dot{\boldsymbol{E}}^{gp}$ represents the granular plastic strain rate, *tot* denotes the corresponding total number of slip systems in the slip geometry, the summation is over the slip systems i of the grain g (or colony g).

When dealing with equiaxed α phases, the plastic deformation rate at the grain level $\dot{\boldsymbol{E}}^{gp}$ is a linear summation of all activated slip systems described by the symmetrical part of the Schmid tensor in the slip geometry:

$$\dot{\boldsymbol{E}}^{gp} = \sum_{i=1}^{tot} \dot{\gamma}^i \boldsymbol{m}^i \tag{6.5}$$

When dealing with the lamellar α+β colony, the granular plastic deformation rate $\dot{\boldsymbol{E}}^{gp}$ should be calculated through an equation considering the average volume fractions of α and β phases for lamellar α+β colonies:

$$\dot{\boldsymbol{E}}^{gp} = v^\alpha \sum_{i=1}^{s} \dot{\gamma}^i \boldsymbol{m}^i + v^\beta \sum_{l=1}^{t} \dot{\gamma}^l \boldsymbol{m}^l \tag{6.6}$$

where v^α and v^β denote the respective volume fractions of α and β phases and are in direct proportion to their widths, s is the total number of the slip systems corresponding to hcp slip geometry, t is the total number of the slip systems corresponding to bcc slip geometry, and $s + t = tot$. The macroscopic plastic strain rate can be estimated as the weighted average of the granular plastic strain rate as follows:

$$\dot{\boldsymbol{E}}^p = \sum_{g=1}^{G} f^g \dot{\boldsymbol{E}}^{gp} \tag{6.7}$$

6.4 Numerical simulations

6.4.1 Slip systems

There are 24 HCP slip systems considered in the model for equiaxed α phase. And for lamellar α+β colonies, 36 slip systems are considered to form the equivalent

slip geometry including 24 HCP slip systems and 12 BCC slip systems. These slip systems are shown in Table 4.1. It is noticed that both the BCC slip systems and 12 $\langle c+a \rangle$ first-order pyramidal $\{10\bar{1}1\}\langle 11\bar{2}3 \rangle$ are able to give needed degrees of freedom to accommodate plastic deformation along $(0001)_\alpha$ direction in the equivalent slip geometry of lamellar colonies. Deformation twinning is not considered in the present model. According to the inverse pole figure (IPF), no preferential grain orientation is observed. Therefore, the Euler angles which represent the grain orientations for both CP-Ti and Ti-6Al-4V can be considered as randomly distributed.

6.4.2 Parameter determination

Model parameters describing the crystal plasticity properties and the scale transition can be gathered from the literature or identified by the experimental tests. Experimental data of monotonous shear tests for homogeneous coarse-grained specimens and harmonic structured specimens and the cyclic shear tests with $\Delta\Gamma = 1.155\%$ for homogeneous CG specimens were emplyed to determine the model parameters. Whereas the data from the cyclic shear tests with $\Delta\Gamma = 1.155\%$ for HS specimens were then used to examine the performance of the numerical models with the calibrated parameters.

For Ti-6Al-4V, the value of Young's modulus measured according to our experiments is akin to that in the work (Simmons et al., 1971). The approximate value of k_y was first determined by referring to that reported in (Liu et al., 2019) in which they identified the parameter as 3.8 based on experimental studies presented in ((Naka and Lasalmonie, 1983; Naka et al., 1988). By fitting the yield strength of monotonic shear tests for CG Ti-6Al-4V and HS Ti-6Al-4V samples, a new value for k_y which was readjusted from the approximate value and the value of k_0 were estimated. Afterwards, these two parameters were tested again and slightly changed by fitting the cyclic shear test. The values of $\dot{\gamma}_0$ and m in the flow rule were gathered from different literatures, i.e., from the work of Kasemer and colleagues (2017) for Ti-6Al-4V. Parameters related to isotropic hardening and kinematic hardening, namely C, B, Q and a, were calibrated by fitting the monotonic hardening and cyclic hardening of homogeneous CG specimens for Ti-6Al-4V. The values of the slip strengths D^i for different slip systems were determined by referring to the work of Song and colleagues (2008) and akin to those listed in the articles (Yang et al., 2011).

The slip strength of bcc slip systems was set equal to that of the basal systems of the hcp slip systems.

Due to the lack of direct reference in the literature, the parameters C^g and C_β for Ti-6Al-4V were identified by fitting the numerical overall response of monotonous shear test obtained by polycrystalline simulation for homogeneous CG Ti-6Al-4V. Details about the identification process can be found in Appendix B. The calibrated values of the used parameters are listed in Table 6.1.

Table 6.1

Model parameters used in this work.

Parameter	Value	Parameter	Value
	Ti-6Al-4V		Ti-6Al-4V
D^{basal}(MPa)	353	M	9.0
D^{prism}(MPa)	397	$\dot{\gamma}_0(s^{-1})$	1.0
$D^{pyr<a>}$(MPa)	441	Q(MPa)	50.0
$D^{pyr<c+a>}$(MPa)	503	A	2.0
D^{bcc}(MPa)	353	B(MPa)	2070.0
E(GPa)	106.0	C	5.0
ν	0.3	C_β(MPa)	0.0
k_0(MPa)	48.0	C^g(GPa)	15.0
$k_y(\mu m^{0.5})$	5.15		

6.4.3 Finite element model tests

Finite element model tests for homogeneous CG and HS specimens are performed to investigate the reliability of the proposed numerical model. These model tests are all based on the monotonous simple shear experiments described in Section 3.1 and Section 3.2. The boundary condition is schematically shown in Fig. 5.2, where the planned displacements are imposed on all surfaces of RVEs.

When dealing with simulations of Ti-6Al-4V specimens, a cubic RVE of dimension of 1.0×1.0×1.0mm for homogeneous CG Ti-6Al-4V is constructed by using the Voronoi tessellation technique, as shown in Fig. 6.4, which contains 50 arbitrary shaped lamellar α+β colonies with random grain orientations. Here the ECM is implemented in the simulation under the framework of CPFEM. As shown in the figure, each colored region denotes an equivalent grain which essentially represents a

lamellar α+β colony. By using ECM, the fine details of alternating laths of α phase and β phase are not necessary to be explicitly represented, which significantly simplifies the construction of representative geometry and makes the simulations in 3D cases more feasible. Ten polycrystalline simulations with ten sets of randomly distributed grain orientations are carried out under simple shear loading conditions. The overall stress-strain curves corresponding to the ten simulations are shown in Fig. 6.5, where the grain orientation effect to the predicted mechanical performance is observed. However the variation of the overall responses remains reasonably low, thus it's reasonable to employ the polycrystalline FE mesh including 50 lamellar α+β colonies as a RVE for homogeneous CG Ti-6Al-4V.
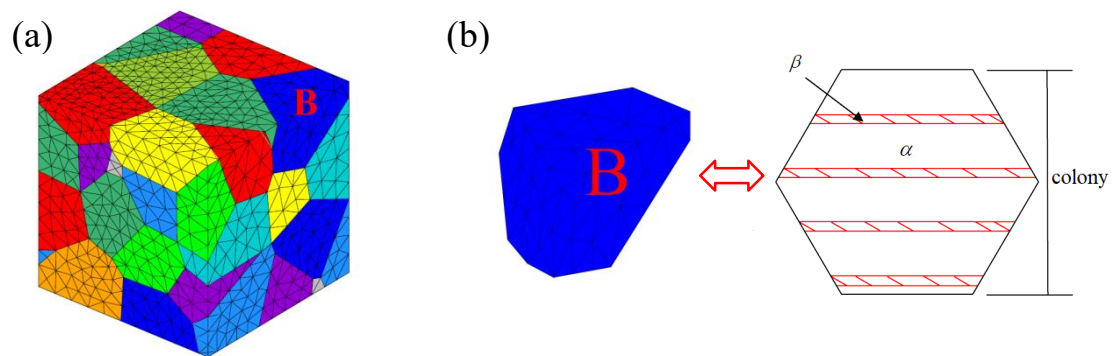
Fig. 6.4 Illustration of (a) the RVE for homogeneous coarse-grained Ti-6Al-4V, where every colored region is an equivalent grain representing a lamellar α+β colony as shown in (b), and 50 lamellar α+β colonies are created.
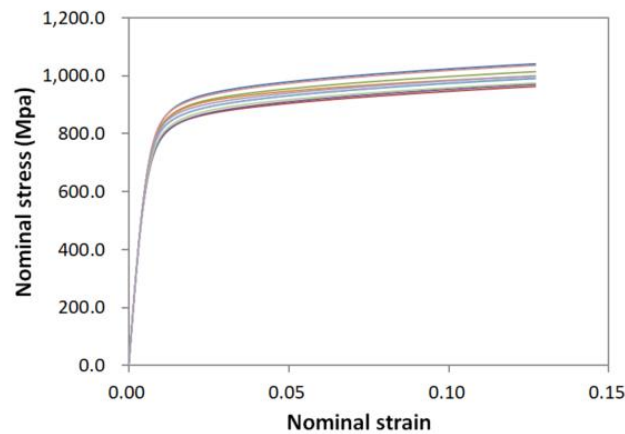
Fig. 6.5 Simulated overall stress-strain curves under monotonic simple shear loading corresponding to ten sets of random grain orientations.

The previous simulated overall response of polycrystalline simulation for homogeneous CG Ti-6Al-4V is taken as a reference to test the performance of 'β-rule' and then calibrate the related parameters, namely C^g and C_β. In this model test, we

use a cubic RVE of dimension of $1.0 \times 1.0 \times 1.0mm$ with 125 cubic elements, as shown in Fig. 6.6a. One of the ten sets of random grain orientations and the corresponding volume fractions of the 50 lamellar α+β colonies are extracted from the previous polycrystalline simulation and then input into the UMAT programmed for the proposed numerical model. Consequently, the FE model in Fig. 6.6a can be regarded as a homogenized counterpart of the polycrystalline FE model in Fig. 6.4a. It's clear that the proposed numerical model which has incorporated the ECM and 'β-rule' makes it unnecessary to directly mesh the fine details of aggregate of lamellar α+β colonies, thus making it feasible to construct the FE meshes for CG regions in HS Ti-6Al-4V.
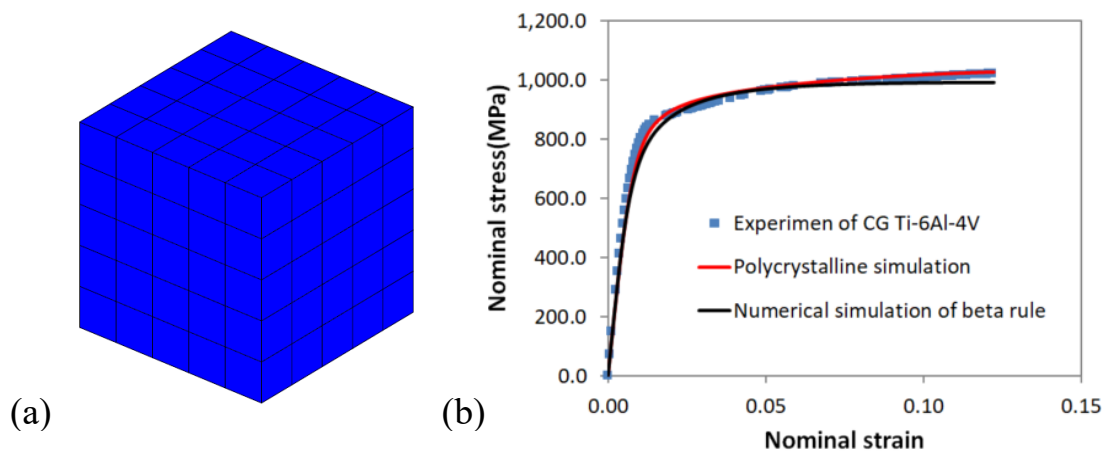
Fig. 6.6 (a) Illustration of FE mesh used in the test of β-rule, (b) Numerical results obtained by FE model test for β-rule and polycrystalline simulation and the comparison with experimental data for homogeneous CG Ti-6Al-4V under monotonic simple shear loading condition.

The values of material parameters describing the crystal plasticity properties will remain the same as that in the previous polycrystalline simulation. And only parameters C^g and C_β need to be identified by fitting the overall response obtained in the previous polycrystalline simulation using the same set of random grain orientation. In Fig. 6.6b, it can be seen that the obtained overall responses matches well with each other when the parameters C^g and C_β are calibrated as 15.0 GPa and 0.0 MPa respectively. We can remark that the ECM coupled with 'β-rule' reproduces faithfully the overall response obtained by polycrystalline simulation.
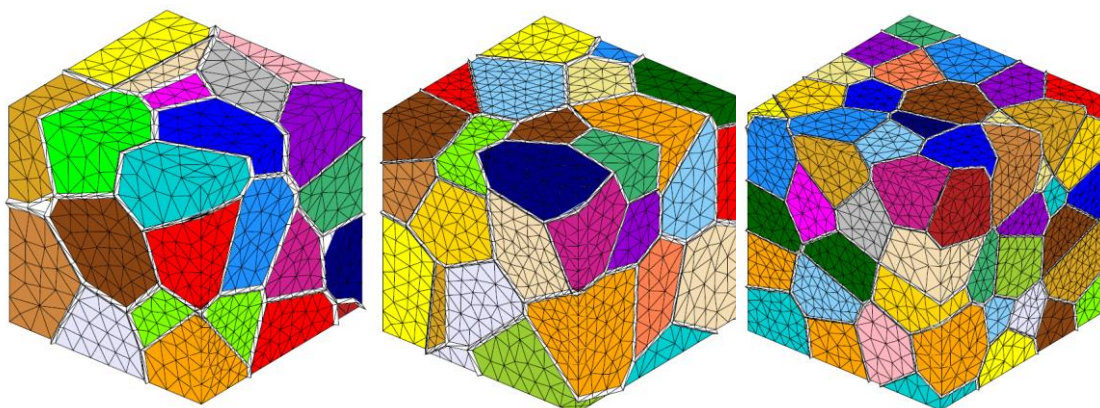
(a)   (b)   (c)

Fig. 6.7 Illustration of RVEs including (a) 30, (b) 50 and (c) 100 CG regions for HS Ti-6Al-4V, where every colored part represents a CG region and the white part represents FG regions.
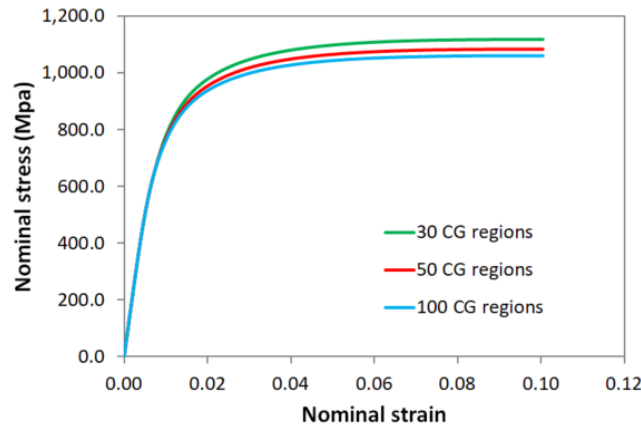
Fig. 6.8 Effect of the number of CG regions in the FE model on the overall response of HS Ti-6Al-4V under monotonic simple shear loading condition.

After the validation of the proposed numerical model as mentioned above, FE model tests are carried out to determine a reasonable RVE to simulate the mechanical properties of HS Ti-6Al-4V. Based on the Voronoi tessellations, a method is developed to generate a microstructure which can represent the geometric features of FG and CG regions for HS Ti-6Al-4V. The volume fraction of FG regions can be accurately controlled in the generated FE model by its 'thickness' between two neighboring CG regions. For FG regions, 50 equiaxed α grains are considered at each Gauss point and are supposed to be sufficient for the accuracy of the numerical model. The average number of lamellar α+β colonies in every CG regions can be determined by using the EBSD maps. In this simulation, 7 lamellar α+β colonies are considered for each CG region. Another important parameter which influences the accuracy of the FE model is the number of CG regions included in the RVE. Fig. 6.7 shows three RVEs with edge length of 1mm, which contain 30, 50 and 100 CG regions respectively and have the same volume fraction of FG regions (13.34%). Monotonic simple shear loading is applied in the FE model tests up to $\Gamma = 10.0\%$ of the overall shear strain. The numerical results shown in Fig. 6.8 indicate that the difference

between the overall responses is not significant when using the three RVEs. And the accuracy of FE models can be obtained when the number of CG regions is 50, as the overall response of RVEs including 50 CG regions is very close to that including 100 CG regions.

6.5 Numerical results and discussions

The above developed model in the previous subsections is used to simulate the microstructure-related mechanical behavior of homogeneous CG and HS specimens for Ti-6Al-4V. Besides, some comparisons between the simulations of CP-Ti and Ti-6Al-4V will be presented where the simulations results for CP-Ti are from Chapter 5. Priority is given to the representation of the numerical results on HS Ti-6Al-4V as these results cannot be found in previous literature.

6.5.1 Comparison with experiments for Ti-6Al-4V

The monotonous and cyclic overall stress-strain responses obtained by simulations for homogeneous CG Ti-6Al-4V and HS Ti-6Al-4V using the proposed numerical model are shown in Fig. 6.9 and Fig. 6.10 respectively, in comparison with the experimental data. It can be noticed that there is a good agreement between the simulations and experimental results. The simulations capture well the strengthening effect of harmonic structure design on Ti-6Al-4V material, as shown in Fig. 6.9. The cyclic hardening is also precisely reproduced by the proposed numerical model according to Fig. 6.10. It can be remarked that the numerical model is able to describe the microstructure's influence on the macroscopic behavior of homogeneous CG Ti-6Al-4V and HS Ti-6Al-4V.

6.5.2.1 Strengthening effects

Referring to experimental data (Fig. 5.8), HS CP-Ti shows a much higher ultimate shear stress (684 MPa) compared with that of homogeneous CG CP-Ti (581 MPa). The material strength is increased by 17.7%. However, Fig. 6.9 shows that the ultimate shear stress of Ti-6Al-4V is only augmented by 6.6%, from 1021 MPa (homogeneous CG Ti-6Al-4V) to 1088 MPa (HS Ti-6Al-4V). It's apparent that the improvement of Ti-6Al-4V's strength by applying harmonic structure design is not as significant as that observed in CP-Ti. This phenomenon consists of the key point of

discussions.
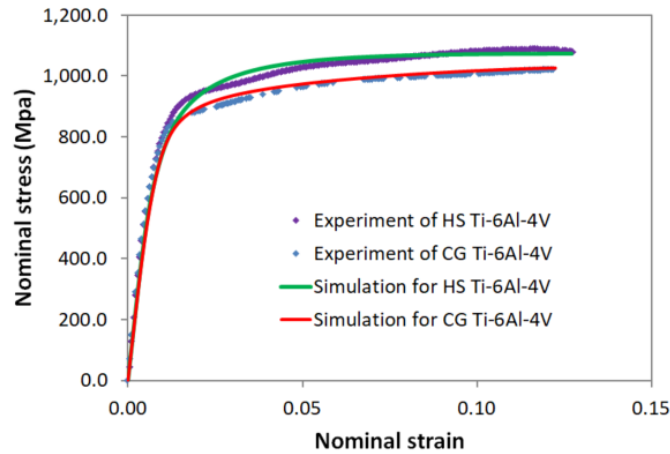
Fig. 6.9 Comparison between simulations and experimental results for homogeneous CG Ti-6Al-4V and HS Ti-6Al-4V in the case of monotonic simple shear condition.
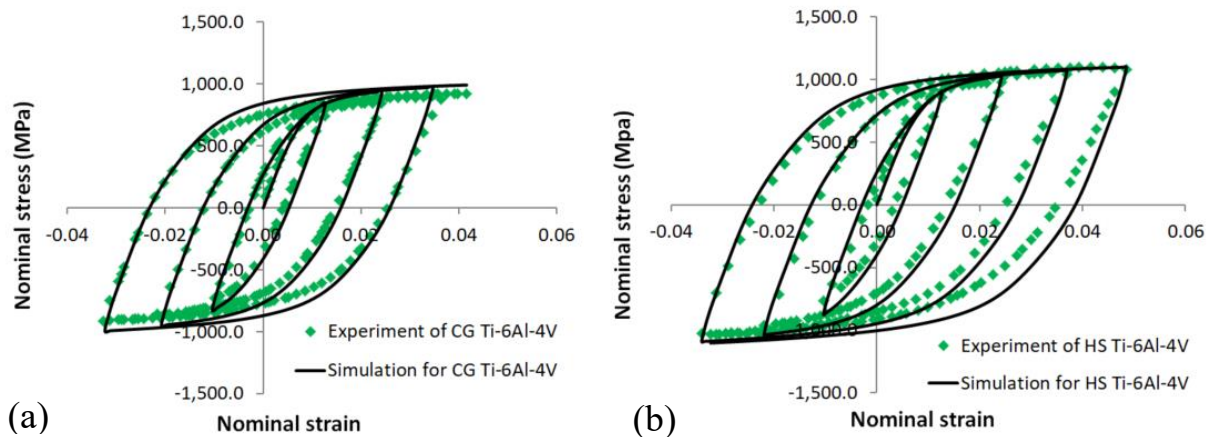
Fig. 6.10 Simulated curves and experimental results for (a) homogeneous coarse-grained Ti-6Al-4V and (b) harmonic structured Ti-6Al-4V in the case of cyclic simple shear condition when ΔΓ = 1.155% every cycle.

6.5.2 Comparison between Ti-6Al-4V and CP-Ti

6.5.2.2 Comparison between HS CP-Ti and HS Ti-6Al-4V

Fig. 6.11 displays the simulated effective shear stress distributions on the surfaces of the HS CP-Ti and HS Ti-6Al-4V RVEs in the case of monotonic shear condition when the overall strain reaches the largest imposed value. From Fig. 6.11a, a sharp contrast of stress levels can be observed between the FG and CG regions in the harmonic structured CP-Ti RVE. The stress level in FG regions is apparently much higher than that in CG regions, which only approximates the overall stress. It can be deduced that for HS CP-Ti the strengthening effect is mainly caused by the FG

regions.

As a contrasting case, the stress field in HS Ti-6Al-4V is dramatically different, as shown in Fig. 6.11b. It can be seen that some neighboring CG regions display completely different stress levels. It appears that some CG regions are much 'harder' than the others. This phenomenon is quite different from the HS CP-Ti sample, in which stress field in the CG regions is relatively homogeneous. Moreover, no special stress concentration can be found in the FG regions. Different from the HS CP-Ti sample, no strong strengthening effect of FG regions is revealed.
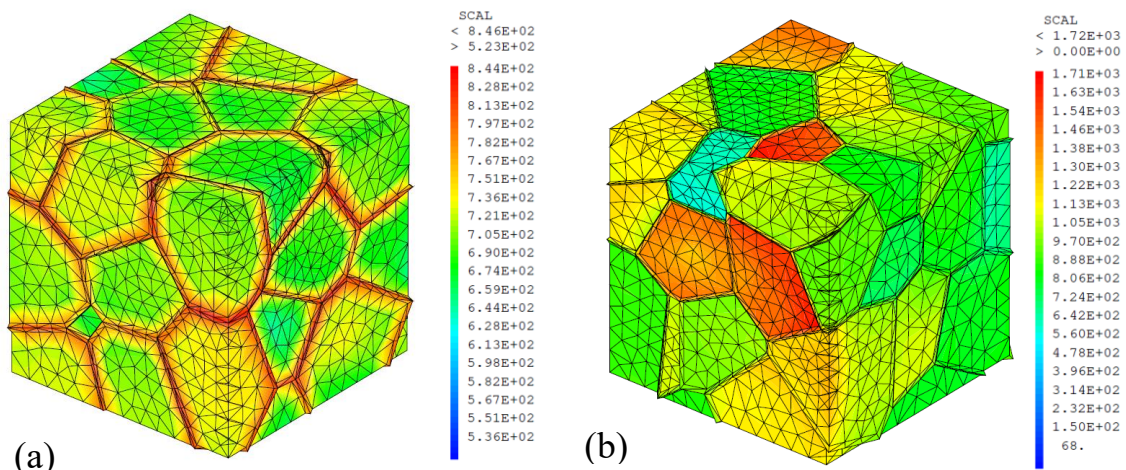
Fig. 6.11 Effective shear stress distribution for (a) HS CP-Ti when $\Gamma = 24.0\%$ and (b) HS Ti-6Al-4V when $\Gamma = 12.7\%$.

6.5.2.3 Comparison between CG CP-Ti and CG Ti-6Al-4V

Looking at the effective shear stress distribution for homogeneous CG CP-Ti and homogeneous CG Ti-6Al-4V in Fig.6.12, it can be noticed that there exists 'hard' grains (or colonies for Ti-6Al-4V) with high stress concentration neighboring with 'soft' grains (or colonies) with relatively low stress level. This arrangement of neighboring 'hard' and 'soft' grains (or colonies) inevitably creates mismatches of deformation and generates heterogeneous strain distribution among the neighboring grains (or colonies), as displayed by Fig. 6.13.

6.5.3 Prevision for different volume fractions of FG regions

It's very challenging to change one microstructure feature without modifying the others experimentally, because the variation of these features is usually highly coupled. However, it can be convenient to vary the microstructure features

independently in numerical simulations to obtain a direct insight of their effect on material properties. Thus an array of synthetic specimens is generated in this section by varying the volume fraction of FG regions in HS CP-Ti and HS Ti-6Al-4V. Then simulations are conducted to study the responses to variations in this volume fraction. It should be noted that only the volume fractions of FG and CG regions are varied while other microstructure lengths and parameter values are held constant in the analysis. Referring to the reported ranges in previous experimental studies, volume fraction of FG regions for each synthetic specimen is fixed at 13.3%, 16.0%, 20.0% and 25.0% respectively. All the simulation results for HS CP-Ti and HS Ti-6Al-4V (Fig. 6.14) show a positive correlation between the volume fraction of FG regions and material strength. Material strength follows a rising trend with an increase of volume fraction of FG regions in HS CP-Ti and HS Ti-6Al-4V. As mentioned in the previous comparisons, there is a greater sensitivity to changes of HS features for CP-Ti in comparison with Ti-6Al-4V.
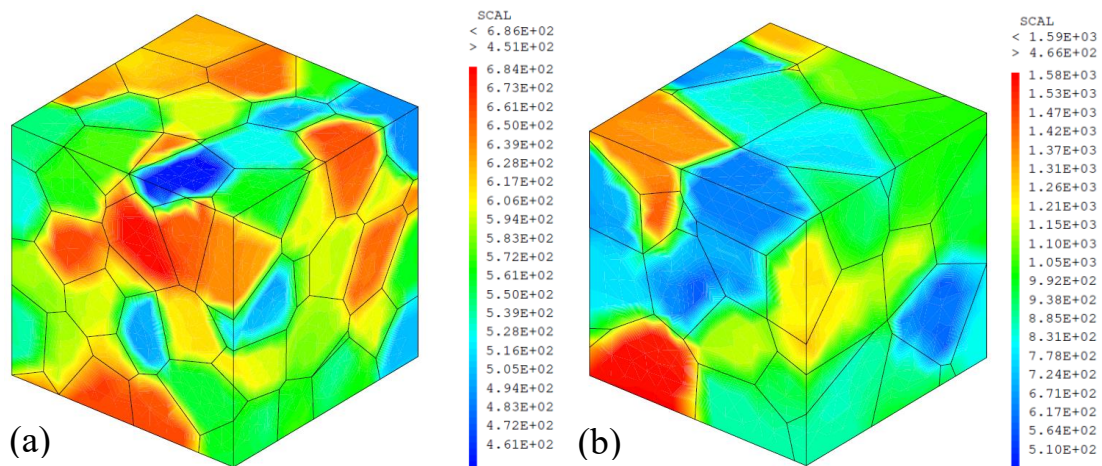
Fig. 6.12 Effective shear stress distribution for (a) homogeneous CG CP-Ti when $\Gamma = 24.0\%$ and (b) homogeneous CG Ti-6Al-4V when $\Gamma = 12.7\%$.

6.5.4 Discussions on the strengthening mechanism

In the present numerical model, the length scale effect as depicted by Eq. (6.9) is considered as one of the main sources of strengthening effect caused by HS design, which essentially represents the obstacles formed by grain or α/β interface boundaries to dislocation motions. Another underlying source of strengthening effect is the spatial arrangement of FG and CG regions due to the HS design, which is implicitly represented through the corresponding FE meshes.
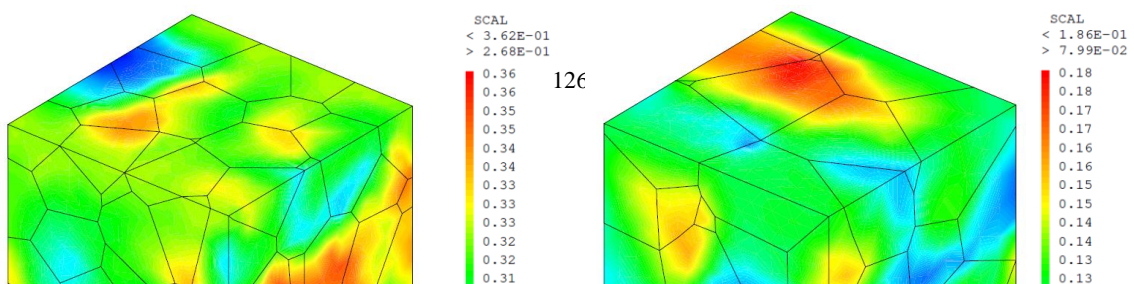
Fig. 6.13 Effective shear strain distribution for (a) homogeneous CG CP-Ti when $\Gamma = 24.0\%$ and (b) homogeneous CG Ti-6Al-4V when $\Gamma = 12.7\%$.

(a)   (b)
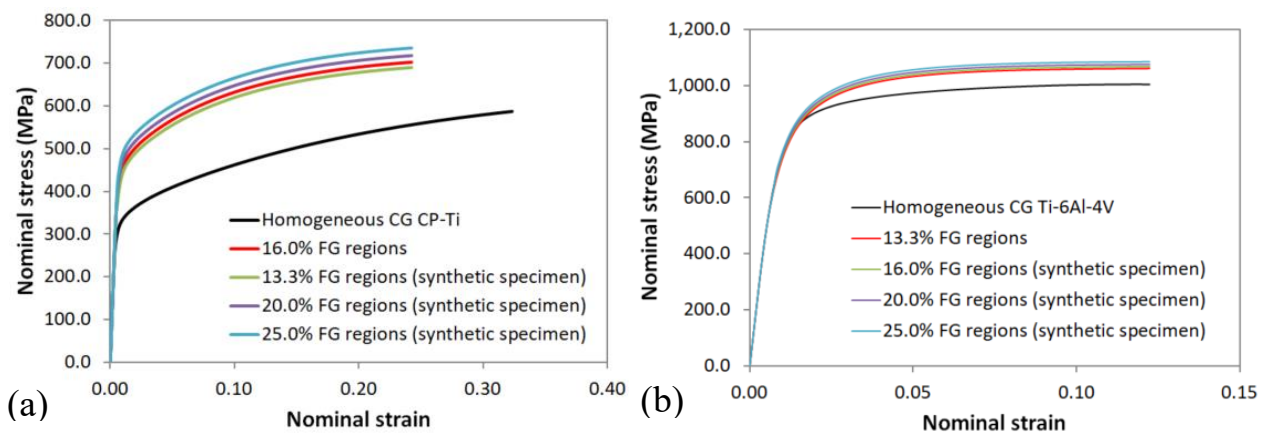
Fig. 6.14 Simulated responses to variations in volume fraction of FG regions conducted on synthetic specimens (a) for HS CP-Ti and (b) for HS Ti-6Al-4V in comparison with simulations for experimental specimens.

As pointed previously, the microstructure effects of the HS design on the material properties are quite different CP-Ti and Ti-6Al-4V. For HS CP-Ti, numerical studies show that the FG regions tend to perform like a thin but relatively hard skeleton enveloping the soft CG regions. Therefore, CP-Ti with HS design is able to bear higher level of external load and endure large deformation, exhibiting a higher strength without great loss of ductility. However, the enhancement of material strength by applying HS design to Ti-6Al-4V is not as efficient as observed in the case of HS CP-Ti. This is most likely attributed to the following two facts:

(1) From the viewpoint of length scale effect, in CG regions the average size of the lamellar α+β colonies is about 50 μm. However, the mechanical properties of an individual lamellar α+β colony are not determined only by this length scale due to the special deformation mechanism caused by the lamellar α+β microstructure. When the hard deformation mode is predominant in certain cases, the widths of α and β laths (2.5 μm and 0.2 μm respectively) could have a major influence on the mechanical

127

behavior of the lamellar α+β colony (Mayeur, 2004). Consequently, even though the average size of equiaxed α grains in FG regions is about 2 μm, the strengthening effect caused by its relatively small grain sizes is no longer as significant as in the case of HS CP-Ti.

(2) Among the 36 slips systems in a lamellar α+β colony, 6 slip systems are related to the soft deformation modes. They are three basal, 1 prismatic and 2 $\langle 111 \rangle\{110\}$ slip systems. It can be noticed that, by obeying the Burgers orientation relationship, the distribution of these slip planes and slip directions are quite concentrated in three-dimensional space. Besides, there is a big difference between the length scales concerning the soft and hard deformation modes. Because of these two aspects, an individual lamellar α+β colony becomes significantly anisotropic. In each CG region, only 7 lamellar α+β colonies are taken into account in the numerical simulation and the grain orientation for every lamellar α+β colony is randomly generated. Therefore a CG region is very likely to be anisotropic too. When a load in a fixed direction is applied to the RVE, some CG regions become 'hard' and some other become 'soft.' Consequently, the local stress is not concentrated in FG regions. This anisotropy strengthening mechanism, which is not significant in CP-Ti, hides the strengthening effect of the FG regions.

6.6 Concluding remarks

In this Section, we proposed a multi-scale numerical model, which incorporated a crystal plasticity model and a micro-macro transition scheme, to simulate the microstructure dependent behavior of CP-Ti and Ti-6Al-4V with or without HS design. This model is successfully implemented into a three-dimensional finite element code. It is shown that experimental results can be well reproduced for homogeneous CG and HS specimens under monotonous and cyclic simple shear loading conditions. The present study leads us to make the following concluding remarks:

1. Based on the investigations of HS CP-Ti and HS Ti-6Al-4V, a general strengthening mechanism of harmonic structure designed materials is proposed. The underlying sources of strengthening effect are mainly the length scale effect and the special arrangement of FG and CG regions. Meanwhile, the strengthening of HS materials also is directly influenced by grain orientations, the number of grains (or

colonies) in CG regions and the anisotropy of slip system strength.

2. The enhancement of material strength caused by the HS design is more significant for CP-Ti than Ti-6Al-4V. For HS CP-Ti, numerical simulations clearly indicate that the strengthening is mainly caused by the FG regions, which carry an big part of external load. However, for HS Ti-6Al-4V, even the average size of equiaxed α grains in FG regions is much small compared with the lamellar α+β colony size in CG regions, the improvement of the mechanical property is not as significant as expected. The main reason for this counter performance is the hard deformation model in lamellar α+β colonies in Ti-6Al-4V. In fact, the small microstructure lengths in lamellar α+β colonies, i.e., the widths of α and β laths, are similar to the average size of equiaxed α grains in FG regions. Therefore, the strengthening effect of FG regions is largely hidden, resulting in a slight improvement of material strength.

3. The proposed numerical model is capable of simulating deformation behavior of HS CP-Ti and HS Ti-6Al-4V. Numerical results are in good agreement with experimental data. By varying microstructure features independently in simulations, it's possible to gain a quantitative understanding of the key microstructure effects of the HS design on material properties, viz. the influence of some important parameters such as volume fractions of FG and CG regions, average size of grains or colonies, or widths of α and β laths in lamellar α+β colonies.

Chapter 7 Final conclusion and future outlook

A microstructure-based multi-scale constitutive model for conventional and harmonic structured materials is developed in this work which can be applied to predict, improve and optimize the harmonic structured materials' macroscopic strength-ductility synergy. In particular, it can provide insight into the underlying deformation mechanisms tracing back to the microscopic scale. The multi-scale model is established on the basis of extensive experimental observations and previous numerical studies on the multi-scale plasticity theory and the crystal plasticity model for the lamellar α+β colony. Constitutive laws are established to simulate the mechanical behavior of conventional and harmonic structured dual phase titanium alloys Ti-6Al-4V and also single phase metals such as commercial purity titanium.

In Chapter 4, the strengthening effect of α/β phase interface and the microstructure dependent deformation behavior of conventional structured Ti-6Al-4V are investigated using the high fidelity modelling method. To authors' knowledge, it's the first time to study the effects of the α/β phase interfaces on mechanical properties in the framework of high fidelity modelling methods. The obtained numerical results generate a plenty of detailed information about the macroscopic properties and local deformation behaviors. Based on the results, discussions about the microstructure-properties relationships are made. The obtained numerical results considering the effects of the α/β phase interfaces agree well with the observations in related literature, which on the other way validates the necessity of introducing the α/β phase interface effects into the numerical model.

In Chapter 5 and Chapter 6, by using our numerical model, the mechanical behaviors of two typical HS materials with highly complex microstructures can be well simulated and good agreements between the numerical results and experimental data have been obtained. Further analyses of the numerical results for both conventional and harmonic structured Ti-6Al-4V and CP-Ti have provided us the particular strengthening mechanisms of the harmonic structure design. It's observed that the proposed multi-scale model shows good capabilities of considering the effects of the following ingredients: the anisotropic slip strength, the crystalline orientation distribution, the particular microstructure of harmonic structured materials and strengthening mechanisms namely the lattice resistance, the strengthening by strain hardening, the grain boundary strengthening and the strengthening role of phase

interfaces in lamellar α+β colony.

From the implementation of the two numerical methods, it can be concluded that the main advantage of the high fidelity modelling method is the ability to explicitly study the influence of microstructures on the material's macroscopic properties by including the fine geometric details into the finite element model, thus providing a direct understanding of the relationship between microstructures and macroscopic behavior. However, even the exponential increase in computing power has facilitated the use of larger meshes which is indispensable in explicitly representing fine geometric details, the generation of high fidelity representation of microstructures for titanium and its alloys with complex microstructures such as harmonic structured CP-Ti and Ti-6Al-4V is generally very challenging if not impossible, thus making the implementation of this method quite difficult and setting a limit on its applicability especially in 3D cases. This fact has necessitated the study of the current multi-scale model in which there is no need to explicitly model the individual grains or lamellae in a finite element model.

Besides, an overview of the conclusions drawn from all the numerical results in this work is presented here:

- The simulated yield strength of Ti-6Al-4V is observed to be governed by the size of equiaxed α grains and lamellar colonies. The yield strength increases as the size of grains/colonies decreases. Inclusion of *β* lamellae tends to increase the yield strength. The more lamellar colonies are contained in the Ti-6Al-4V, the higher yield strength the material shows. The presence of α/*β* phase interfaces plays an important role in strengthening the lamellar colonies. The enforcement of Burgers orientation relationship between the crystallographic orientation of α and *β* lamellae softens the material. In opposition, it seems that the lamellar width has minor effect on the yield strength.

- Inspection of the local deformation in Ti-6Al-4V samples shows that the mechanical behavior of equiaxed α grains and lamellar colonies are significantly influenced by the crystallographic orientation. For lamellar colonies, the c-axis is the stiffest orientation. Mechanical constraints between α and β lamellae greatly depend on the α/β phase interfaces and are closely linked to the crystallographic orientation. It's found that all the colonies with β lamellae being relatively softer have their c-axis closely aligned with the tensile loading direction z axis. Stress

concentration emerges in β lamellae for lamellar colonies whose c-axis is not oriented along the loading direction.

- It is improper to neglect the influence of α/β phase interfaces on mechanical properties of lamellar colonies in the simulations using high fidelity microstructure representations. Otherwise numerical results which are counterintuitive to experimental observations may be obtained.

- Based on the investigations of HS CP-Ti and HS Ti-6Al-4V, a general strengthening mechanism of harmonic structure designed materials is proposed. The underlying sources of strengthening effect are mainly the length scale effect and the special arrangement of FG and CG regions. Meanwhile, the strengthening of HS materials also is directly influenced by grain orientations, the number of grains (or colonies) in CG regions and the anisotropy of slip system strength.

- The enhancement of material strength caused by the HS design is more significant for CP-Ti than Ti-6Al-4V. For HS CP-Ti, numerical simulations clearly indicate that the strengthening is mainly caused by the FG regions, which carry a big part of external load. However, for HS Ti-6Al-4V, even the average size of equiaxed α grains in FG regions is much small compared with the lamellar α+β colony size in CG regions, the improvement of the mechanical property is not as significant as expected. The main reason βor this counter performance is the hard deformation model in lamellar α+β colonies in Ti-6Al-4V. In fact, the small microstructure lengths in lamellar α+β colonies, i.e., the widths of α and β laths, are similar to the average size of equiaxed α grains in FG regions. Therefore, the strengthening effect of FG regions is largely hidden, resulting in a slight improvement of material strength.

- The proposed numerical model is capable of simulating deformation behavior of HS CP-Ti and HS Ti-6Al-4V. Numerical results are in good agreement with experimental data. By varying microstructure features independently in simulations, it's possible to gain a quantitative understanding of the key microstructure effects of the HS design on material properties, viz. the influence of some important parameters such as volume fractions of FG and CG regions, average size of grains or colonies, or widths of α and β laths in lamellar α+β colonies.

On the basis of the findings achieved in this thesis work, some interesting topics are discussed here which can be tackled in the future work. For the sake of simplicity,

the current model neglects the effects of crystal rotation and latent hardening as well as the influence of twinning. A more rigorous numerical model can be developed by incorporating these issues to improve the capability of simulating more complicated mechanical behavior and providing a better and more comprehensive understanding of the underlying mechanisms. Besides, some of the formulations used in this current model is more phenomenological and tend to be less physics-based. For example, the utility of flow rules involving the dislocation density and its evolution can be explored with the support of certain experimental data. This work is an attempt to investigate the deformation mechanisms of the heterogeneous microstructure design 'harmonic structure design' and the main strengthening mechanisms considered have been limited to the grain boundary strengthening and phase interface strengthening. The introduction of other strengthening mechanisms should be carefully considered and thoroughly testified to improve the current model. Moreover, the numerical study should also be extended to the fields of damage. This requires not only a robust finite element code and the improvement of the current plasticity model but also a proper and physics-based damage model.

Appendix A: Scale transition rule: the 'β-rule'

The early studies on the plastic deformation of metallic polycrystals are essentially deduced from the investigation of single crystal plastic behavior and have been limited within the framework of Sach's (1928) and Taylor's (1938) approaches for a long time. These studies have achieved significant progress in this topic. However, most results based on these studies are qualitative and lead to only a rather loose consistency between the experimental results and the numerical ones.

Realistic assessment of the macroscopic mechanical behavior requires consideration of a large number of grains in order to gain statistically accurate results. If the physical aspect of the deformation mechanisms is captured at the microscopic scale, the macroscopic response of the model has a good chance to represent correctly complex phenomena. This is the basic idea of multi-scale approaches. However, consideration of all individual grains often leads to voluminous numerical effort. Therefore, micro-macro scale transition methods were developed in order to make the multi-scale approaches feasible.

Kroner (1961) proposed a homogenization approach by using the so-called 'self-consistent method'. It refers to the study of an inclusion within an infinite matrix and assumes that every grain of the polycrystal can be treated as an inclusion within the homogenized matrix constituted of other grains. Consequently, the deformation of the polycrystal can be modeled by some suitable average procedure over all grains.

Kroner (1961) proposed a simplified self-consistent scheme by defining a 'a priori' interaction law between one grain and the matrix, which is motivated by the solution of the inclusion problem as provided by Eshelby (1957). In this simplification treatment, an elastic interaction is assumed between the matrix and the inclusion. Therefore, Kroner's model has good ability of predicting the elastic deformation, while not very suitable in the case of a plastically-flowing polycrystal. Based on these previous studies, Hutchinson (1966) investigated the stress localization problem in the framework of visco-plasticity. The local granular stresses $\boldsymbol{\sigma}^g$ can be computed through Eq. (A.1) if the global stresses and the strains and the local strains are known by means of a fourth-order tensor $\boldsymbol{L}^*$:

$$\dot{\boldsymbol{\sigma}}^g = \dot{\boldsymbol{\sigma}} + \boldsymbol{L}^* : (\dot{\boldsymbol{\varepsilon}} - \dot{\boldsymbol{\varepsilon}}^g) \qquad (A.1)$$

with

$$L = \frac{1}{V} \sum_V L^g : (L^* + L^g)^{-1} : (L^* + L) \tag{A.2}$$

where $\dot{\sigma}$ and $\dot{\varepsilon}$ are global stresses and global strains respectively, $\dot{\varepsilon}^g$ is local stress, L^* describes the incremental behavior of the equivalent medium, L^g describes the tangent behavior of each grain.

Afterwards, Berveiller and Zaoui (1979) developed a self-consistent scheme for the case of plasticity which is capable of considering the elasto-plastic intergranular accommodation and plastic internal stress relaxation, thus producing an explicit "a priori" interaction law. The following relation summarizes several models in literature which includes the overall equivalent stress Σ in uniaxial tension and the plastic part of the overall strain tensor E^P:

$$\sigma^g = \sigma + \alpha\mu(E^P - \varepsilon^{pg}) \tag{A.3}$$

with $$\frac{1}{\alpha} = 1 + \frac{3\mu E^P}{2\Sigma} \quad and \quad E^P = \langle\varepsilon^{pg}\rangle \tag{A.4}$$

where μ is the elastic shear modulus, α is a scalar function given by Eq. (A.4), ε^{pg} is the plastic part of local strain in a given grain. This self-consistent scheme is explicit and then easy for applications. It should be noted that when applying this self-consistent scheme the restriction should be limited to spherical inclusions and isotropic and homogeneous materials. From the perspective of physics, the above mentioned self-consistent approaches all implies that a local plastic strain tends to reduce the local stress when the plastic strain becomes larger.

Besides, a self-consistent scheme called the "β-rule" was proposed by Gailleteau (1987) and modified by Pilvin (1990). It deals with the micro-macro transition by using a phenomenological model. An approximate localization rule was used and given under an explicit form. The macroscopic stress and macroscopic strain in a volume element are not directly related. A two-step localization process gives first the local stress in each grain, and then the resolved shear stress on each slip system. The constitutive equations are then defined at a microscale. They allow us to obtain the local slip rate, which is summed up to give the macroscopic plastic strain rate.

The main source of intergranular heterogeneity is related to a phenomenological variable β^g which is able to correctly capture the plastic accommodation (Cailletaud and Pilvin, 1994). The granular stress tensor σ^g is determined by:

$$\sigma^g = \sigma + C^g(B - \beta^g) \tag{A.5}$$

with
$$B = \sum_{g=1}^{G} f^g \beta^g \tag{A.6}$$

where B is the average of the variable β^g for all grains, in the present study, g represents the equiaxed α grains or the lamellar α+β colonies, G indicates all grains (or colonies) considered at a continuum point, C^g denotes a material parameter, f^g denotes the volume fraction for every grain (or every colony). The evolution of β^g is calculated through a differential equation (Cailletaud and Pilvin, 1994):

$$\dot{\beta}^g = \dot{E}^{gp} - C_\beta \beta^g \sum_{i=1}^{tot} |\dot{\gamma}^i| \tag{A.7}$$

where C_β denotes a material parameter, $\dot{E}^{gp}$ represents the granular plastic strain rate, *tot* denotes the corresponding total number of slip systems in the slip geometry, the summation is over the slip systems i of the grain g (or colony g).

Fig. A.1 Images showing the implementation of 'β-rule' in the present numerical model.

In the present study on HS CP Ti or HS Ti6Al4V, three operating levels can be defined according to the scale on which the deformation is described by the constitutive relations. The macroscopic scale is defined by a FE model including a sufficient number of coarse grained regions or lamellar α+β colonies, separated by a interconnected network of fine grains. At this scale, the macroscopic responses are assumed to follow the linear elastic relation between stress and the elastic part of strain. The second level called mesoscopic level is defined at each continuum point by a RVE containing sufficient grains or lamellar α+β colonies. Here the 'β-rule' is used to calculate the granular local stresses from the macroscopic stresses of Gauss points. With respect to the plastic strain, the macroscopic plastic strains are estimated from the granular plastic strains through a homogenization procedure. Finally, the plasticity

development is estimated at the third level corresponding to the scale of crystallographic slip system (CSS). Crystal plasticity is applied at this level to relate slip activities to resolved shear stresses on all slip systems. The implementation of the scale transition rule 'β-rule' is then fulfilled and the three operating levels are depicted in Fig. A.1.

Appendix B: Performance of the 'β-rule' coupling with the crystal plasticity model for lamellar α+β colonies

The application of the 'β-rule' for micro-macro transition in the multi-scale model is an efficient tool for simplify the numerical simulations using crystal plasticity. In this appendix, the accuracy and performance of this method on simulating mechanical behavior of polycrystalline aggregate are investigated for lamellar α+β colonies (Mayeur, 2004).

This study consists in establishing a FE polycrystalline RVE containing a large number of lamellar α+β colonies. The numerical results will be compared to those obtained by using the 'β-rule'.

The experimental data base used in the following computational study can be found in Section 3.2. The overall responses, the intergranular and intragranular heterogeneities of local stress/strain fields are studied. Then the overall response of simulation is used to calibrate the parameters used in the "β-rule", whose performance will be further estimated by analyzing the simulated intergranular heterogeneities of local fields.

B1. Polycrystalline FE model and 'β-rule' FE model

To generate meshes corresponding to polycrystalline aggregate with β annealed microstructure containing 50 arbitrary shaped grains, the Voronoi tessellation technique has been used. As shown in Fig. B.1a, each colored region denotes an equivalent grain which essentially represents a lamellar α+β colony. Microstructural lengths are determined by referring to the experimental data of simple shear tests for Ti-6Al-4V with conventional microstructures as presented in Section 3.2. The measured average lamellar $\alpha + \beta$ colony size, widths of α lath and β lath were 49.4μm, 2.5μm and 0.2μm respectively.

In parallel, a homogenous FE model using the 'β-rule' was also established for comparison (Fig. B.1b). In this FE model, 50 lamellar α+β colonies identical to those used in the polycrystalline FE model are strictly mapped to the RVE at each Gauss point, i.e., both the chosen set of the crystal orientations and volume fractions of the equivalent grains in the polycrystalline simulations are exactly input into the 'β-rule' FE model by means of the user-defined materials subroutine (UMAT). Both FE models are subjected to the same boundary conditions in numerical simulations.
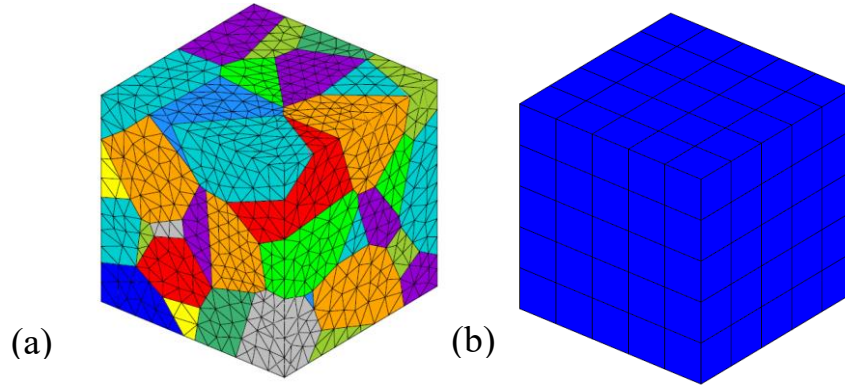
Fig. B.1 Illustration of meshes used in (a) polycrystalline simulation, where every colored part represents an equivalent grain and (b) "β-rule" simulation.

B2. Scattering effect of the random crystal orientations

Polycrystalline simulations with ten sets of randomly generated crystal orientations are conducted under simple shear loading conditions using the polycrystalline mesh illustrated in Fig. B.1a. The overall stress-strain curves corresponding to the ten simulations are shown in Fig. B.2. The orientation effect to the predicted macroscopic behavior is observed. It is observed that the variation of the overall responses caused by randomly distributed crystal orientations remains reasonably low.
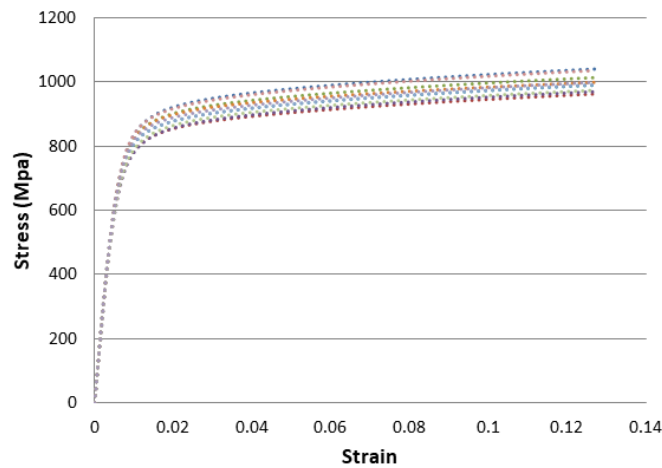
Fig. B.2 Simulated overall stress-strain curves under monotonic simple shear loading corresponding to ten sets of randomly generated crystalline orientations.

B3. Stress and strain distribution in the polycrystalline RVE

Fig. B.3 shows the distribution of the maximal shear stress and the maximal shear strain obtained by the polycrystalline simulations under simple shear loading at the overall strain of 12.7%. Heterogeneous stress/strain distributions can be clearly

observed. The corresponding overall stress is 1040.5 MPa and the range of local stresses is of 564.0MPa-1530.0MPa. The maximum local strain (19.0%) is about 1.5 times the overall strain (12.7%).
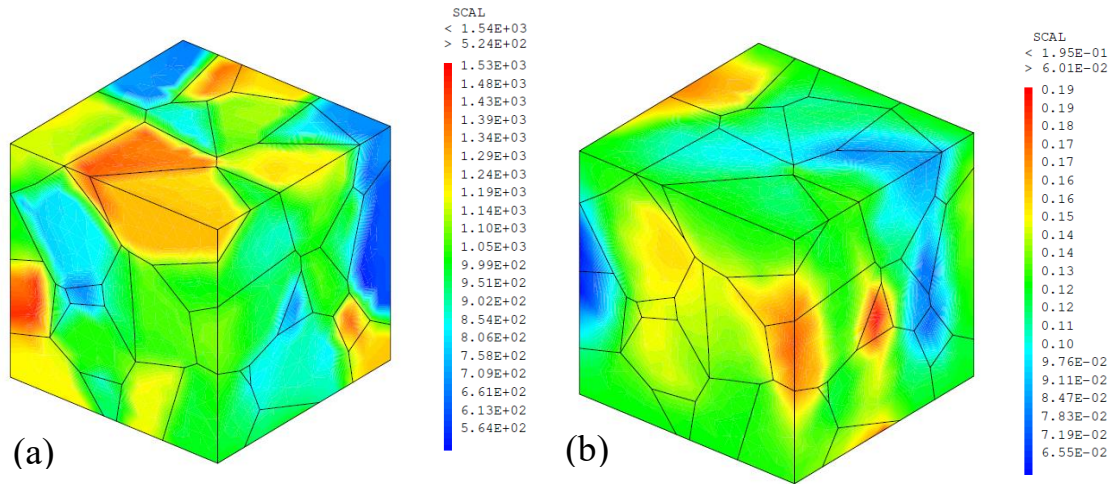
(a) (b)

Fig. B.3 Distributions of (a) shear stress and (b) shear strain at the overall strain of 12.7% predicted by polycrystalline simulation.

To provide an insight into the heterogeneous behavior at the granular scale, the volume averaged stress-strain response of each of the 50 lamellar α+β colonies is plotted as shown in Fig. B.4, where the dotted lines represent the averaged local responses for the 50 α+β colonies and the red solid line represents the overall response of the polycrystalline RVE.
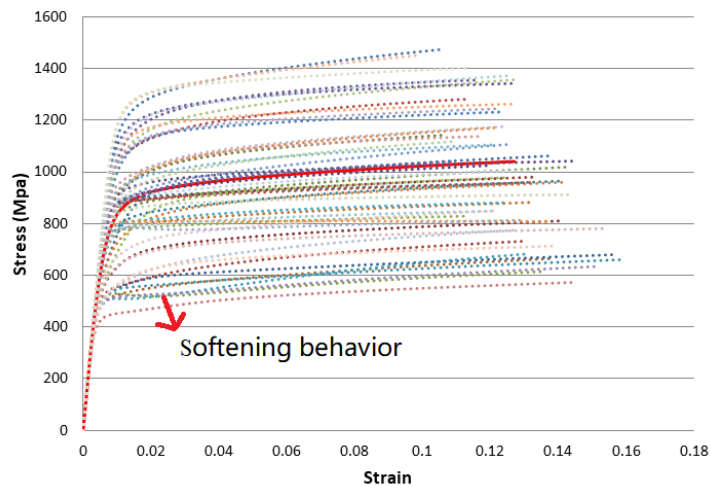
Fig. B.4 Illustration of intergranular heterogeneity based on the volume averaged responses of 50 equivalent grains for lamellar α+β colonies.

From this figure, the *intergranular* heterogeneities of local state among different α+β colonies are observed. Furthermore, it can be noticed that some α+β colonies work in monotonic shear as imposed by the overall loading, others undergo a certain degree of softening behavior as marked in the figure. This can be attributed, as

pointed out in Sarma et al. (1996) or in Barbe et al. (2001), to the interaction among α+β colonies of a polycrystalline aggregate.

Another feature remains to be investigated is the *intragranular* heterogeneity predicted by the polycrystalline simulation. In Fig. B.5, the stress-strain states at all the Gauss points of the smallest equivalent grain (number 10) and biggest equivalent grain (number 39) are illustrated at three loading levels (average granular strain = 5.1%, 9.7% and 14.1% for grain10 and average granular strain = 4.1%, 8.1% and 12.2% for grain39, corresponding to overall strain = 4.38%, 8.54% and 12.7% respectively). The volume averaged (mean) responses of the two grains are also plotted. The intragranular heterogeneity can be clearly observed in both grains at different strain levels.
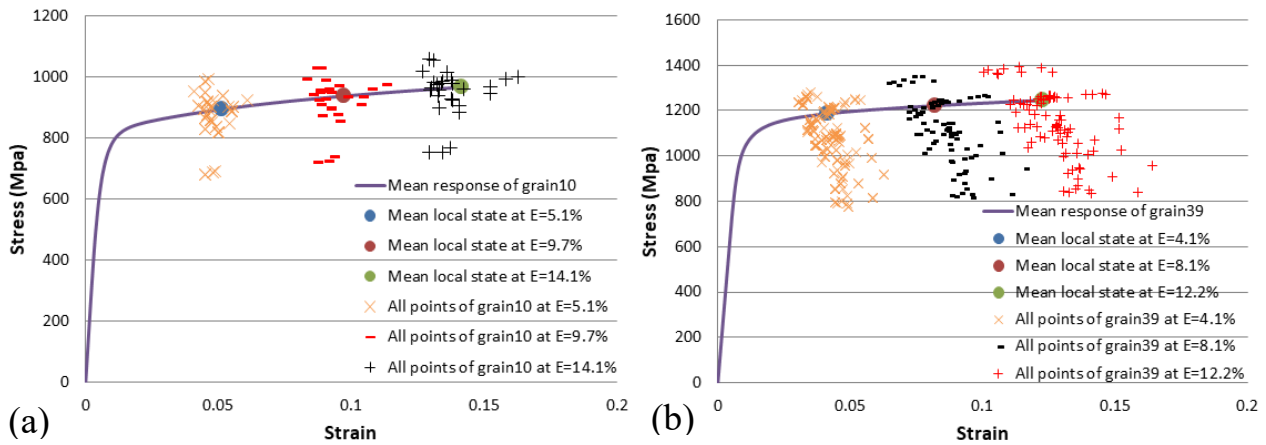
Fig. B.5 Intragranular heterogeneity: (a) response at three volume averaged local strains (E = 5.1%, 9.7%, 14.1%) of all the points in grain10, (b) response at three volume averaged local strains (E = 4.1%, 8.1%, 12.2%) of all the points in grain39.

B4. Calibration and validation of the 'β-rule'

The predicted overall stress-strain curve of the polycrystalline simulations under monotonic simple shear loading is taken as a reference to calibrate the parameters of the β-rule FE model, namely C^g and C_β. As mentioned above, both the 50 crystal orientations and volume fractions of the 50 equivalent grains involved in the polycrystalline simulations will be strictly mapped to the simulations of the using β-rule FE model. The parameters C^g and C_β are identified by fitting the overall response predicted by polycrystalline simulation. As shown in Fig. B.6, the obtained overall responses matches well with each other when the parameters C^g and C_β are calibrated as 15.0 GPa and 0.0 MPa respectively.

141

Fig. B.7a shows the intergranular heterogeneities of local state among different α+β colonies predicted by the β-rule FE model simulations, where the dotted lines represent the averaged local responses for the 50 α+β colonies and the red solid line represents the overall response of the β-rule FE model (Fig. B.1b). It can be seen that the simulation results using the β-rule FE model possess significant intergranular heterogeneities as observed in Fig. B.4. Besides, the upper bound (the strongest grain) and lower bound (the softest grain) of the volume averaged local responses obtained by the two simulations are plotted together with their corresponding overall responses in Fig. B.7b. It's remarked that the range of volume averaged granular responses predicted by the β-rule FE model is very close to that obtained by the polycrystalline simulations.
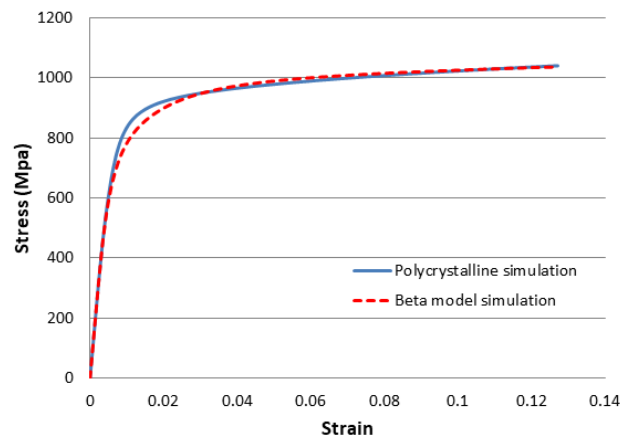
Fig. A.6 Fitting on monotonic simple shear test, the overall response of calibrated β-model is compared with that of polycrystalline simulation.
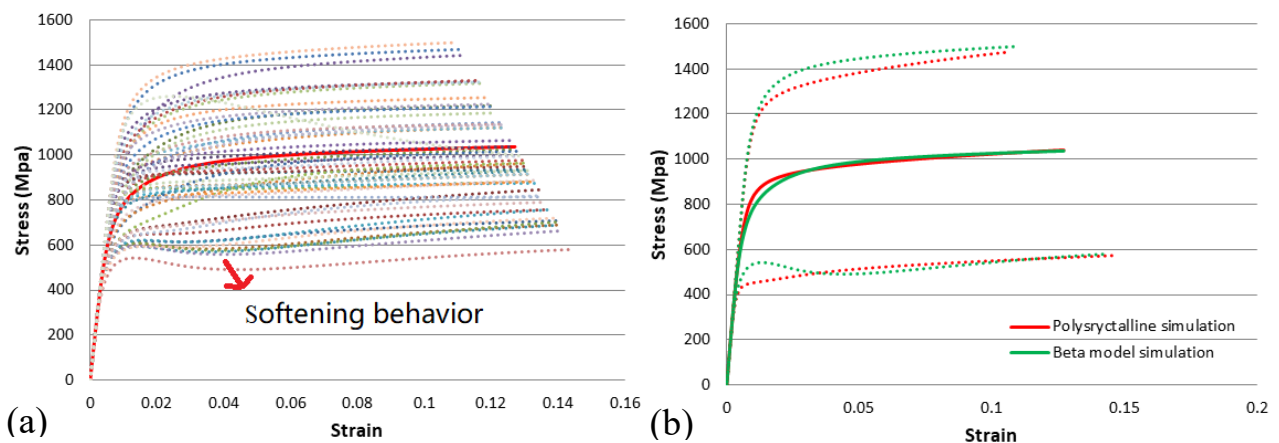
Fig. B.7 (a) Illustration of intergranular heterogeneity predicted by β-rule simulation, (b) the comparison of intergranular heterogeneities between polycrystalline simulation and β-model simulation, where the dotted lines represent the upper and lower bounds of each simulation.

In Fig. B.8 the comparison between the local responses of four selected equivalent grains obtained by the polycrystalline simulation and the β-rule FE simulation are plotted. It can be conclude that the β-rule FE model has satisfactory capability to capture the intergranular heterogeneity.
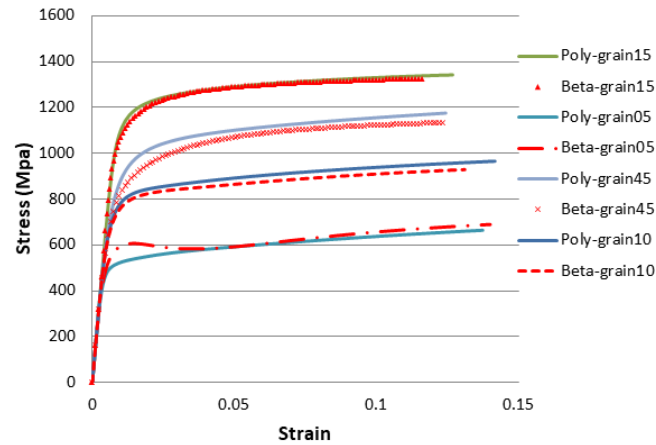
Fig. B.8 Local responses for four selected equivalent grains obtained from polycrystalline simulation and β-model simulation under simple shear loading.

Fig. B.9a and B.9b show the comparisons between polycrystalline simulation and the β-rule FE simulation for a monotonic tensile test and a cyclic simple shear test respectively, using the parameters calibrated by fitting the monotonic simple shear test. Considering the two loading conditions are not included in the database of the calibration procedure, the fine agreement shown in these figures is thus a further validation of the β-rule FE model.
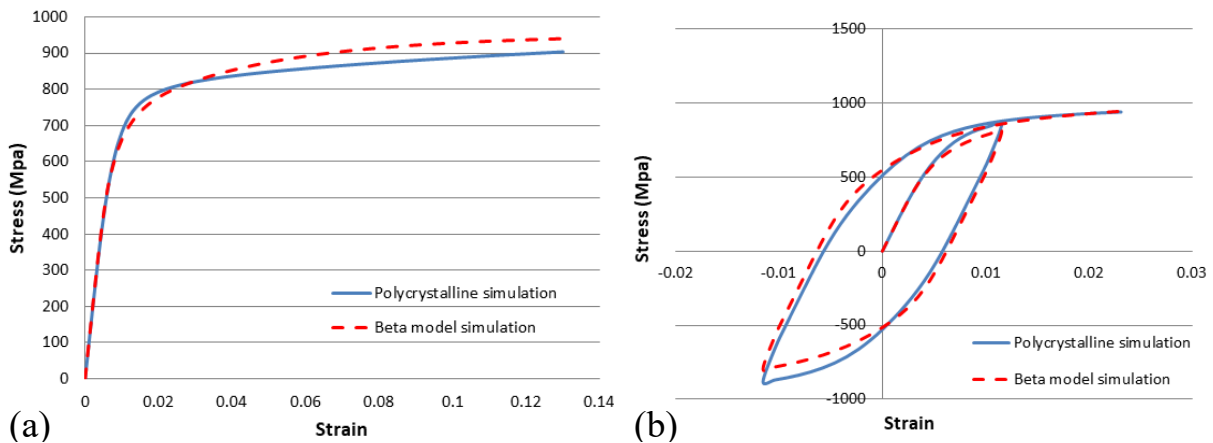
Fig. B.9 Validation of the calibrated parameters in β-model: comparison between the polycrystalline simulation and β-model, (a) monotonic tensile test and (b) cyclic simple shear test.

References

Abdul-Latif, A., Saanouni, K., 1994. Damaged Anelastic Behavior of FCC Polycrystalline Metals with Micromechanical Approach. Int. J. Damage Mech. 3, 237-259.

Ameyama, K., Fujiwara, H., 2012. Creation of harmonic structure materials with outstanding mechanical properties. Mater. Sci. Forum 706-709, 9-16.

Ameyama, K., Sekiguchi, T., Seo, T., Ciuca, O.P., 2012. Harmonic Structure Design by Severe Plastic Deformation Powder Metallurgy Process and their Outstanding Mechanical Properties. 15th Intl. Conf. on Advances in Materials and Processing Technologies (AMPT), 23-26 Sept.

Arsenlis A, Tang M., 2003. Simulations on the growth of dislocation density during Stage 0 deformation in BCC metals. Modell Simul Mater Sci Eng. 11, 251-264.

Argon, A., 2008. Strengthening mechanisms in crystal plasticity. Oxford University Press, USA.

Balint, D.S., Deshpande, V.S., Needleman, A, Giessen, E.V., 2006. Size effects in uniaxial deformation of single and polycrystals: a discrete dislocation plasticity analysis. Modelling and Simulation in Materials Science and Engineering. 14, 409-422.

Balint, D.S., Deshpande, V.S., Needleman, A., Giessen, E.V., 2005. A discrete dislocation plasticity analysis of grain-size strengthening. Materials Science and Engineering a-Structural Materials Properties Microstructure and Processing. 400, 186-190.

Bacon, D.J., 1967. A Method for Describing a Flexible Dislocation. Physica Status Solidi (b). 23, 527-538.

Bachmann, F., Hielscher, R., Schaeben, H., 2010. Texture analysis with MTEX-free and open source software toolbox. Sol. St. Phen. 160, 63-68.

Bania, P.J., 1994. Beta Titanium Alloys and Their Role in the Titanium Industry. JOM. 46, 16–19.

Barton, N.R., Dawson, P.R., 2001. On the spatial arrangement of lattice orientations in hot-rolled multiphase titanium. Modell. Simul. Mater. Sci. Eng. 9, 433-463.

Barbe, R.J., Decker, L., Jeulin, D., Cailletaud, G., 2001. Intergranular and intragranular behavior of polycrystalline aggregates. Part 1: F.E. model. Int. J. Plast. 17 (4), 513-536.

Barkia, B., 2014. Viscoplasticité à l'ambiante du titane en relation avec ses teneurs en oxygène et hydrogène. PhD thesis. Ecole Polytechnqiue.

Beranger, A. S., Feaugas , X., Clavel, M., 1993. Low cycle fatigue behaviour of an α+β titanium alloy: Ti6246. Materials Science and Engineering A 172, 31-41.

Berveiller, M., Zaoui, A., 1979. An extension of the self-consistent sche,e to plastically-flowing polycrystals. J. Mech. Phys. Solids. 26, 325-344.

Billard, S., Fondere, J.P., Bacroix, B., Dillard, G.F., 2006. Macroscopic and microscopic aspects of the deformation and fracture mechanisms of ultrafine-grained aluminum processed by hot isostatic pressing. Acta Mater. 54, 411-21.

Boyer, R., 1996. An overview on the use of titanium in the aerospace industry. Mater. Sci. Eng. A 213, 103–114.

Brown, L.M., 1964. The self-stress of dislocations and the shape of extended nodes. Philosophical Magazine. 10, 441-466.

Brockman, R., 2003. Analysis of elastic-plastic deformation in TiAl polycrystals. Int. J. Plasticity 19, 1749-1772.

Bridier, F., Villechaise, P., Mendez, J., 2005. Analysis of the different slip systems activated by tension in a α/β titanium alloy in relation with local crystallographic orientation. Acta Mater. 53, 555-567.

Bridier, F., McDowell, D.L., Villechaise, P., Mendez, J., 2009. Crystal plasticity modeling of slip activity in Ti-6Al-4V under high cycle fatigue loading. Int. J. Plast. 25, 1457-1485.

Bui, Q.H., Dirras, G., Ramtani, S., Gubicza, J., 2010. On the strengthening behavior of ultrafine-grained nickel processed from nanopowders. Mater. Sci. Eng. A 527, 3227-3235.

Castany, P., Pettinari-Sturmel F, Douin J, Coujou A., 2008. "Insitu transmission electron microscopy deformation of the titanium alloy Ti-6Al-4V: interface behaviour." Materials Science and Engineering A 483: 719-722.

Cailletaud, G., 1987. Une Approche Micromécanique Phénoménologique du Comportement Inélastique des Métaux. Thèse d'état, Univ. Paris VI.

Cailletaud, G., 1992. A micromechanical approach to inelastic behaviour of metals. Int. J. Plast. 8, 55-73.

Cailletaud, G., Pilvin, P., 1994. Utilisation de modéles polycristallins pour le calcul par éléments finis. Rev. Eur. Eléments Finis. 3, 515-541.

Chaboche, J.L., 1989. Constitutive equations for cyclic plasticity and cyclic viscoplasticity. Int. J. Plast. 5, 247-302.

Challa, V.S.A., Misra, R.D.K., Somani, M.C., 2016. Strain hardening behavior of nanograined/ultrafine-grained (NG/UFG) austenitic 16Cr-10Ni stainless steel and its relationship to austenite stability and deformation behavior. Mater. Sci. Eng. A. 649, 153-157.

Challa, V.S.A., Wan, X.L., Somani, M.C., Karjalainen, L.P., 2014. Strain Hardening behavior of Phase Reversion-induced nanograined/ultrafine-grained (NG/UFG) austenitic stainless Steel and Relationship with Grain Size and Deformation Mechanism. Mater. Sci. Eng. A. 613, 60-70.

Chatterjee, K., Echlin, M.P., Kasemer, M., Callahan, P.G., Pollock, T.M., Dawson, P., 2018. Prediction of tensile stiffness and strength of Ti-6Al-4V using instantiated volume elements and crystal plasticity. Acta Materialia. 157, 21-32.

Ciuca, O.P., Ota, M., Deng, S., Ameyama, K., 2013. Harmonic Structure Design and Mechanical Properties of Pure Ni Compact, Mater. Trans. 54, 162-163.

Cleveringa, H.H.M., Giessen, E.V., Needleman, A., 1999. A discrete dislocation analysis of bending. International Journal of Plasticity. 15, 837-868.

Collins, P., 2004. A combinatorial approach to the development of composition–microstructure–property relationships in titanium alloys using directed laser deposition. Ph.D. thesis, The Ohio State University, 201 West 19th Avenue, Columbus, OH 43210.

Coghe, F., Tirry, W., Rabet, L., Schryvers, D., Houtte, P.V., 2012. Importance of twinning in static and dynamic compression of a Ti-6Al-4V titanium alloy with an equiaxed microstructure. Mater. Sci. Eng. A. 537, 1-10.

Curtin, W.A., Miller, R.E., 2003. Atomistic/continuum coupling in computational materials science. Modelling and Simulation in Materials Science and Engineering. 11, 33-68.

Dirras, G., Ota, M., Tingaud, D., Ameyama, K., Sekiguchi, T., 2015. Microstructure evolution during direct impact loading of commercial purity α-titanium with harmonic structure design. Matériaux & Techniques, 103, 311.

Dirras, G., Tingaud, D., Ueda, D., Hocini, A., Ameyama, K., 2017. Dynamic Hall-Petch versus grain-size gradient effects on the mechanical behavior under simple shear loading of β-titanium Ti-25Nb-25Zr alloys. Mater. Letters, 206, 214–216.

Dirras, G., Ueda, D., Hocini, A., Tingaud, D., Ameyama, K., 2017. Cyclic shear behavior of conventional and harmonic structure-designed Ti-25Nb-25Zr β-titanium alloy: Back-stress hardening and twinning inhibition. Scr. Mater. 138, 44-47.

Donea, J., Huerta, A., Ponthot, J.-Ph., Rodriguez-Ferran, A., 2004. Encyclopedia of Computational Mechanics. Chapter 8: Crystal Plasticity and Evolution of Polycrystalline Microstructure. John Wiley and Sons.

Doquet, V., Barkia, B.,2015. A micromechanical model of the viscoplastic behavior of titanium accounting for its anisotropic and strain-rate-dependent viscosity. Mech. Time-Depend. Mater. 19, 153-166.

Eshelby, J.D., 1957. The determination of the elastic field of an ellipsoidal inclusion. Comput. Mech. Adv. 2(1).

Farbaniec, L., Dirras, G., Krawczynska, A., Mompiou, F., Couque, H., F. Naimi, Bernard, F., Tingaud, D., 2014. Powder metallurgy processing and deformation characteristics of bulk multimodal nickel, Mater. Charact., 94, 126-137.

Fan, G.J., Choo, H., Liaw, P.K., Lavernia, E.J., 2006. Plastic deformation and fracture of ultrafine-grained Al–Mg alloys with a bimodal grain size distribution. Acta Mater. 54, 1759-1766.

Fang, T.H., Li, W.L., Tao, N.R., Lu, K., 2011. Revealing extraordinary intrinsic tensile plasticity in gradient nano-grained copper. Sci. 331, 1578-1590.

Fleck, N.A., Muller, G.M., Ashby, M.F., Hutchinson, J.W., 1994. Strain Gradient Plasticity - Theory and Experiment. Acta Metallurgica Et Materialia. 42, 475-487.

Fujiwara, H., Tanaka, H., Nakatani, M., Ameyama, K., 2010. Effects of nano/meso harmonic microstructure on mechanical properties in austenitic stainless steel produced by MM/HRS process. Mater. Sci. Forum, 638-642, 1790-1795.

Geetha, M., Singh, A.K., Asokamani, R., Gogiac, A.K., 2009. Ti based biomaterials, the ultimate choice for orthopaedic implants – a review. Prog. Mater. Sci. 54, 397–425.

Goh, C.-H., Wallace, J.M., Neu, R.W., McDowell, D.L., 2001. Polycrystal Plasticity Simulations of Fretting Fatigue. Int. J. of Fatigue. 23, S423-S435.

Goh, C.-H., 2002. Crystallographic Plasticity in Fretting of Ti-6Al-4V. Ph.D. Thesis, Georgia Institute of Technology.

Goh, C.-H., Neu, R.W., McDowell, D.L., 2003. Crystallographic plasticity in fretting of Ti-6Al-4V. Int. J. Plasticity 19 (10), 1627-1650.

Groh, S., Zbib, H.M., 2009. Advances in Discrete Dislocations Dynamics and Multiscale Modeling. Journal of Engineering Materials and Technology-Transactions of the Asme. 131.

Gubicza, J., Bui, H.Q., Fellah, F., Dirras, D., 2009. Microstructure and mechanical behavior of ultrafine-grained Ni processed by different powder metallurgy methods, J. Mater. Research, 24, 217-226.

Hall, E.O., 1951. The Deformation and Ageing of Mild Steel: III Discussion of Results. Proceedings of the Physical Society. Section B. 64, 747.

Hama, T., Kobuki, A., Takuda, H., 2017. Crystal-plasticity finite-element analysis of anisotropic deformation in a commercially pure titanium Grade 1 sheet. Int. J. Plast. 91, 77-108.

Han, B.Q., Lee, Z., Witkin, D., Nutt, S., Lavernia, E.J., 2005. Deformation behavior of bimodal nanostructured 5083 Al alloys. Metall. Mater. Trans. A, 36A, 957-965.

Hill, R., 1965. Continuum micro-mechanisms of elastoplastic polycrystals. J. Mech. Phys. Solids. 13, 89-101.

Horita, Z., Smith, D.J., Furukawa, M., Nemoto, M., Valiev, R.Z., Langdon, T.G., 1996. An investigation of grain boundaries in submicrometer-grained Al-Mg solid solution alloys using high-resolution electron microscopy. J. Mater. Res. 11, 1880-1890.

Horita, Z., Furukawa, M., Langdon, T.G., Nemoto, M., 1998. Equal-channel angular pressing (ECAP): A novel method for microstructural control. Materia Jpn. 37, 767-774.

Hocini, A., 2017. Étude comparative du comportement mécanique et des mécanismes de déformation sous cisaillement simple et cyclique des alliages de titane élaborés par métallurgie des poudres: structures harmoniques versus alliages conventionnels, PhD Thesis, Univ. Paris XIII.

Hull, D., Bacon, D.J., 2001. Introduction to dislocations (4th ed.), Butterworth Heinmann.

Hutchinson, J.W., 1966. Elastic-plastic behavior of polycrystalline metals and composites. Proc. R. Soc. London. A 319, 247-272.

Ibishi B. Finite-element simulations of harmonic structured materials [Manuscript]. Lund: Lund University; 2016.

Joshi, S.P., Ramesh, K.T., Han, B.Q., Lavernia, E.J., 2006. Modeling the Constitutive Response of Bimodal Metals. Metall and Mat Trans A 37, 2397.

Kasemer, M., Quey, R., Dawson, P., 2017. The influence of mechanical constraints introduced by β annealed microstructures on the yield strength and ductility of Ti-6Al-4V. J. Mech. Phys. Solids. 103, 179-198.

Kalidindi, S.R., Salem, A.A., Doherty, R.D., 2003. Role of deformation twinning od strain hardening in cubic and hexagonal polycrystalline metals. Adv. Eng. Mater. 5, 229-232.

Kanit, T., Forest, S., Galliet, I., Mounoury, V., Jeulin, D., 2003. Determination of the size of the representative volume element for random composites: statistical and numerical approach. Int. J. Solids Struct. 40, 3647-3679.

Kang, J.Y., Kim, J.G., Kim, S.K., Chin, K.G., Lee, S., Kim, H.S., 2016. Outstanding mechanical properties of higi-pressure torsion processed multiscale TWIP-cored three layer steel sheet. Scr. Mater. 123, 122-125.

Kelly, A. , Groves, G.W. , 1970. Crystallography and Crystal Defects. Prentice Hall, Reading.

Kikuchi, S., Kubozono, H., Nukui, Y., Nakai, Y., Ueno, A., Kawabata, M.O., Ameyama, K., 2018. Statistical fatigue properties and small fatigue crack propagation in bimodal harmonic structured Ti-6Al-4V alloy under four-point bending. Mater. Sci. Eng. A 711, 29-36.

Knezevic, M., Lebensohn, R.A., Cazacu, O., Revil-Baudard, B., Proust, G., Vogel, S.C., Nixon, M.E., 2013. Modeling bending of α-titanium with embedded polycrystal plasticity in implicit finite elements, Mater. Sci. Eng. A 564, 116-126.

Koch, C.C., 2003. Optimization of strength and ductility in nanocrystalline and ultrafine grained metals. Scripta Mater. 49, 657-662.

Koiter, W.T., 1969. Progress in Solid Mechanics. Amsterdam: North-Holland, Vol. 1, pp. 165.

Kroner, E., 1961. On the plastic deformation of polycrystals. Acta metallurgica. 9, 155-161.

Kubin, L.P., Canova, G., Condat, M., Devincre, B., Pontikis, V., Bréchet, Y., 1992. Dislocation microstructures and plastic flow: a 3D simulation. Solid State Phenomena. 23, 455-472.

Langlois, P., Tingaud, D., Dirras, G., 2019. Spark Plasma Sintering as a route for producing in-demand microstructures: Application to the tensile-ductility enhancement of polycrystalline nickel, In: Cavaliere, P. (Eds.), Spark Plasma Sintering of Materials. Springer, Cham, pp. 575-604.

Leyens, C., Peters, M., 2003. Titanium and Titanium alloys: Fundamentals and Applications. Wiley-VCH GmbH & Co. KGaA, Weinheim.

Lee, E., 2004. Microstructure evolution and microstructure: mechanical properties relationships in alpha–beta titanium alloys, Ph.D. thesis, The Ohio State University, 201 West 19th Avenue, Columbus, OH 43210.

Leutering, G., Williams, J.C., 2007. Phase transformations. Titanium. Springer Verlag, Berlin, Heidelberg. 15-382.

Li, W.L., Tao, N.R., Lu, K., 2008. Fabrication of a gradient nano-micro-structured surface layer on bulk copper by means of a surface mechanical grinding treatment. Scripta Materialia. 546-549.

Lin, B., Zhao, L.G., Tong, J., Christ, H.-J., 2010. Crystal plasticity modeling of cyclic deformation for a polycrystalline nickel-based superalloy at high temperature. Materials Science and Engineering A 527, 3581-3587.

Liu, J., Li, J., Dirras, G., Ameyama, K., Cazes, F., 2018. A three-dimensional multi-scale polycrystalline plasticity model coupled with damage for pure Ti with harmonic structure design. Int. J. Plast. 100, 192–207.

Lubarda, V.A., Blume, J.A., Needleman, A., 1993. An Analysis of Equilibrium Dislocation Distributions. Acta Metallurgica Et Materialia. 41, 625-642.

Lu, K., 2014. Making strong nanomaterials ductile with gradients. Science. 1455-1456.

Lu, K., Lu. J., 2004. Nanostructured surface layer on metallic materials induced by surface mechanical attrition treatment. Materials Science and Engineering: A. 38-45.

Lutjering, G., Williams, J.C., 2003. Titanium. Springer, New York, NY.

Lutjering, G., Willaims, J.C., 2007. Titanium. New York, Springer.

Mayeur, J.R., 2004. Three-dimensional modeling of titanium–aluminum alloys with application to attachment fatigue. M.S. Thesis, Georgia Institute of Technology, Atlanta, GA, USA.

Mayeur, J.R., McDowell, D.L., 2007. A three-dimensional crystal plasticity model for duplex Ti-6Al-4V. Int. J. Plast. 23, 1457-1485.

Ma, E., 2006. Eight routes to improve the tensile ductility of bulk nanostructured metals and alloys. JOM 58, 49-53.

Madec, R., Devincre, B., Kubin, L.P., 2000. New Line Model for Optimized Dislocation Dynamics Simulations. MRS Online Proceedings Library. 653.

Ma, E., Zhu, T., 2017. Towards strength–ductility synergy through the design of heterogeneous nanostructures in metals. Materials Today. 6, 323-331.

Ma, Q., Clarke, D.R., 1995. Size-Dependent Hardness of Silver Single-Crystals. Journal of Materials Research. 10, 853-863.

McDowell, D.L., 1994. Multiaxial effects in metallic materials," Symposium on Durability and Damage Tolerance. ASME AD-Vol. 43, ASME Winter Annual Meeting, Chicago, IL, Nov. 6-11, 213-267.

Méric, L., Cailletaud, G., 1991. Single crystal modeling for structural calculations. Part2: finite element implementation. J. Eng. Mater. Technol. 113, 171-182.

Misra, R.D.K., Challa, V.S.A., Venkatsurya, P.K.C., Shen, L., Somani, M.C., Karjalainen, L.P., 2015. Interplay between Grain Structure, Deformation Mechanisms, and Austenite Stability in Phase Reversion-Induced Nanograined/Ultrafine-Grained Ferrous Alloy. Acta Materialia, 84, 339-348.

Misra, R.D.K., Zhang, Z., Surya, P.K.C., Somani, M.C., Karjalainen, L.P., Martensite Shear Phase Reversion-Induced Nanograined/Ultrafine-Grained Fe-16Cr-10Ni alloy: The Effect of Interstitial Alloying Elements and Degree of Austenite Stability on Phase Reversion. Mater. Sci. Eng. A. 527, 7779-7792.

Mompiou, F., Tingaud, D., Chang, Y., Gault, B., Dirras, G., 2018. Conventional vs harmonic-structured β-Ti-25Nb-25Zr alloys: A comparative study of deformation mechanisms. Acta Materialia. 161, 420-430.

Monnet, G., Devincre B, Kubin L.P, 2004. "Dislocation study of prismatic slip systems and their interactions in hexagonal close packed metals: application to zirconium." Acta Materialia 52: 4317-4328.

Morrissey, R.J., 2001. Strain Accumulation and Shakedown in Fatigue of Ti-6Al-4V. Ph.D. Thesis, Georgia Institute of Technology.

Mythili, R., Saroja S., Vijayalakshmi, M., 2007. Study of mechanical behaviour and deformation mechanism in α-β Ti4.4Ta1.9Nb alloy. Materials Science and Engineering A. 454, 43-51.

Naka, S., Lasalmonie, A., 1983. Cross-slip on the first order pyramidal plane $(10\bar{1}1)$ of atype dislocations $[12\bar{1}0]$ in the plastic deformation of α-titanium single crystals. J. Mater. Sci. 18, 2613-2617.

Naka, S., Lasalmonie, A., Costa, P., Kubin, L., 1988. The low-temperature plastic deformation of α-titanium and the core structure of a-type screw dislocations. Phil. Mag. A 57, 717-740.

Neeraj, T., Savage, M.F., Tatalovich, J., Kovarik, L., Hayes, R.W., Mills, M.J., 2005. Observation of tension-compression asymmetry in a and a-b titanium alloys. Phil. Mag. A 85, 279-295.

Numakura, H., Minonishi Y, Koiwa M., 1986. <1123> (1011) Slip in titanium polycrystals at room temperature. Scripta Metallurgica. 20, 1581-1586.

Nye, J.F., 1953. Some geometrical relations in dislocated crystals. Acta Metallurg. 1, 153-162.

Obstalecki, M., Wong, S.L., Dawson, P.R., Miller, M.P., 2014. Quantitative analysis of crystal scale deformation heterogeneity during cyclic plasticity using high-energy X-ray diffraction and finite-element simulation. Acta Mater. 75, 259–272.

Ohthuki, C., Osake, A., Lida, H., Ohta, K., 1999. Biocompatible titanium implant. US Patent 5, 855, 612.

Orlov, D., Fujiwara, H., Ameyama, K., 2013.Obtaining copper with harmonic structure for the optimal balance of structure-performance relationship. Mater. Trans. 54, 1549-1553.

Orlov, D., Ameyama, K., 2020. Critical Assesment 37: Harmonic-structure materials - idea, status and perspectives. Materials Science and Technology 36, 517-526.

Orlov, D., Kulagin, R., Beygelzimer, Y., 2020. Strain partitioning and back-stress evaluation in harmonic-structure materials. Materials Letters 275, 128126.

Ota, M., Vajpai, S.K., Kurokawa, K., Watanabe, T., Ameyama, K., Dirras, G., 2014. Creation of High Performance Ti and Ti-6Al-4V via Harmonic Structure Design Approach. 35th Risoe Intl. Symposium on Materials Science, 1-5 Sept.

Ota, M., Kurokawa, K., Vajpai, S.K., Ameyama, K., 2013. Harmonic Microstructure Formation in a Two Phase Stainless Steel. Conference: 16th International Conference on Advances in Materials and Processing Technologies, Taipei, Taiwan.

Ota, M., Vajpai, S.K., Imao, R., Kurokawa, K., 2015. Application of high pressure gas jet mill process to fabricate high performance harmonic structure designed pure titanium trans. JIM 56, 154–159.

Park, H.K., Ameyama, k., Yoo, J., Hwang, H., Kim, H.S., 2018. Additional hardening in harmonic structured materials by strain partitioning and back stress. Mater. Res. Lett. 5, 261-267.

Perilla, J.A. M., Sevillano, J.G., 1995. Two-Dimensional sections of the yield locus of a Ti-6%AL-4%V alloy with a strong trasverse-type crystallographic α – texture. Mat. Sci. Eng. A, 201, 103-110.

Pettifor, D.G., Oleinik , I.I., Nguyen-Manh, D., Vitek, V., 2002. Bond-order potentials: bridging the electronic to atomistic modelling hierarchies. Computational Materials Science. 23, 33-37.

Philippe, M.J., Serghat, M., Van Houtte, P., Esling, C., 1995. Modelling of texture evolution for materials of hexagonal symmetry - II. application to zirconium and titanium αor near αalloys. Acta Metall. Mater. 43, 1619-1630.

Pilvin, P., 1990. Approaches Multiéchelles pour la Prévision du Comportement Inélastique des Métaux. PhD thesis, Univ. Paris VI.

Picu, R.C., Majorell, A., 2002. Mechanical behavior of Ti-6Al-4V at high and moderate temperatures. II. Constitutive modelling. Mater. Sci. Eng. A 326, 306-316.

Poole, W.J., Ashby, M.F., Fleck, N.A., 1996. Micro-hardness of annealed and work-hardened copper polycrystals. Scripta Materialia. 34, 559-564.

Prakash, D.G.L., Ding, R., Moat, R.J., Jones, I., Withers, P.J., Fonseca, J.Q., Preuss, M., 2010. Deformation twinning in Ti-6Al-4 V during low strain rate deformation to moderate strains at room temperature. Mater. Sci. Eng. A. 527, 5734-5744.

Ramtani, S., Dirras, G., Bui, H.Q., 2010. A bimodal bulk ultra-fine-grained nickel: Experimental and micromechanical investigations, Mech. Mater., 42, 522-536.

Rhee, M., Stolken, J.S., Bulatov, V.V., Rubia, T.D., Zbib, H.M., Hirth, J.P., 2001. Dislocation stress fields for dynamic codes using anisotropic elasticity: methodology and analysis. Materials Science and Engineering: A. 309, 288-293.

Roters, F., Eisenlohr, P., Hantcherli, L., Tjahjanto, D.D., Bieler, T.R., Raabe, D., 2010. Overview of constitutive laws, kinematics, homogenization and multiscale methods in crystal plasticity finite-element modeling: Theory, experiments, applications. Acta Materialia. 58, 1152-1211.

Saito, Y., Tsuji, N., Utsunomiya, H., Sakai, T., Hong, R.G., 1998. Ultra-fine grained bulk aluminum produced by accumulative roll-bonding (ARB) process. Scr. Mater. 39, 1221-1227.

Sauvage, X., Wildeb, G., Divinski, S.V., Horita, Z., 2012. Grain boundaries in ultrafine grained materials processed by severe plastic deformation and related phenomena. Mater. Sci. Eng. A 540, 1-12.

Sachs, G., 1928. Zur Ableitung einer Fliessbedingung. Z. VDI, 72, 734.

Sawangrat, C., Yamaguchi, O., Vajpai, S.K., Ameyama, K., 2014. Application of harmonic structure design to biomedical Co-Cr-Mo alloy for improved mechanical properties. Trans. JIM 55, 99-105.

Sawangrat, C., Kato, S., Orlov, D., Ameyama, K., 2014. Harmonic-structured copper: performance and proof of fabrication concept based on severe plastic deformation of powders. Journal of Materials Science. 49, 6579-6585.

Saada, G., Dirras, G., 2009. Plasticity of nanocrystalline materials: a critical viewpoint. Int. J. Mater. Research, 100, 1456–1460.

Sánchez-De Jesús, F., Bolarín-Miró, A.M., Torres-Villaseñor, G., Cortés-Escobedo, C.A., 2010. Mechanical alloying of biocompatible Co–28Cr–6Mo alloy. J. Mater. Sci: Mater. Med. 21, 2021-2026.

Schmid, E., Boas, W., 1935. Kristallplastizity¨at. Springer-Verlag: Berlin.

Schoenfeld, S.E., Kad, B., 2002. Texture Effects on Shear Response in Ti-6Al-4V Plates. Int. J. of Plasticity. 18, 461-486.

Segal, V.M., 1995. Materials processing by simple shear. Mater. Sci. Eng. A 197, 157-164.

Seagle, S.R., 1997. Titanium and titanium alloys. Kirk-Othmer Encyle. Chem. Technol. 24, 2.

Sekiguchi, T., Ono, K., Fujiwara, H., Ameyama, K., 2010. New microstructure design for commercially pure titanium with outstanding mechanical properties by mechanical milling and hot roll sintering. Trans. JIM 51, 39–45.

Shilkrot, L.E., Curtin, W.A., Miller, R.E., 2002. A coupled atomistic/continuum model of defects in solids. Journal of the Mechanics and Physics of Solids. 50, 2085-2106.

Shilkrot, L.E., Miller, R.E., Curtin, W.A., 2004. Multiscale plasticity modeling: coupled atomistics and discrete dislocation mechanics. Journal of the Mechanics and Physics of Solids. 52, 755-787.

Sheh, M.Y., Stouffer, D.C., 1990. A crystallographic model for the tensile and fatigue response for Rene N4 at 982 degrees C. J. Appl. Mech. 57, 25-31.

Shu, J.Y., Fleck, N.A., Giessen, E.V., Needleman, A., 2001. Boundary layers in constrained plastic flow: comparison of nonlocal and discrete dislocation plasticity. Journal of the Mechanics and Physics of Solids. 49, 1361-1395.

Simmons, G., Wang, H., 1971. Single Crystal Elastic Constants and Calculated Aggregate Properties: A Handbook. The MIT Press, Cambridge, MA.

Sluys, L., Estrin, Y., 2000. The analysis of shear banding with a dislocation based gradient plasticity model. International Journal of Solids and Structures. 37, 7127-7142.

Smyshlyaev, V.P., Fleck, N.A., 1996. The role of strain gradients in the grain size effect for polycrystals. Journal of the Mechanics and Physics of Solids. 44, 465-495.

Song, X., Zhang, S.Y., Dini, D., Korsunsky, A.M., 2008. Finite element modeling and diffraction measurement of elastic strains during tensile deformation of HCP polycrystals. Comput. Mater. Sci. 44, 131-137.

Suryanarayana, C., 2001. Mechanical alloying and milling. Prog. Mater. Sci. 46, 1-184.

Suri, S., Viswanathan, G.B., Neeraj, T., Hou, D.H., Mills, M.,1999. Room temperature deformation and mechanisms of slip transmission in oriented single-colony crystals of an α/β titanium alloy. Acta Metall. 47, 1019-1034.

Tan, X., Gu, H., Laird, C., Munroe, N.D.H., 1998. Cyclic Deformation Behavior of High-Purity Titanium Single Crystals: Part I. Orientation Dependence of Stress-Strain Response. Met. Trans. A. 29, 507-512.

Taylor, G.I., 1938. Analysis of plastic strain in a cubic crystal. Stephen Timoshenko 60th Anniversary. 218-224.

Taylor, G.I., 1934. The mechanism of plastic deformation. Proc. R. Soc. London A.145:362.

Taylor, G., 1938. Plastic strain in metals. I. Int. Metals. 62, 307-324.

Tenckhoff, E., 1988. Deformation mechanism, texture and anisotropy in Zirconium. Philadelphia, Special technical publication.

Thomas, J., Groeber, M., Ghosh, S., 2012. Image-based crystal plasticity FE framework for microstructure dependent properties of Ti-6Al-4V alloys. Mater. Sci. Eng. A. 553, 164-175.

Tingaud, D., Sadat, T., Dirras, G., 2019. Nickel-Tungsten Composite-Like Microstructures Processed by Spark Plasma Sintering for Structural Applications, In: Cavaliere P. (Eds), Spark Plasma Sintering of Materials. Springer, Cham, pp. 605-634.

Ueda, D., Dirras, G., Hocini, A., Tingaud, D., Ameyama, K., Langlois, P., Vrel, D., Trzaska, Z., 2018. Data on processing of Ti-25Nb-25Zr β-titanium alloys via powder metallurgy route: Methodology, microstructure and mechanical properties. Data in Brief, 17, 730-708.

Vassel, A., Eylon, D., Combers, Y., 1993. Beta Titanium Alloys, Editions de la Revue de Metallurgie.

Vajpai, S.K., Ota, M., Watanabe, T., Maeda, R., Sekiguchi, T., Kusaka, T., Ameyama, K., 2015. The development of high performance ti-6al-4v alloy via a unique microstructural design with bimodal grain size distribution. Metall. Mater. Trans. A 46, 903–914.

Vajpai, S.K., Yu, H., Ota, M., Watanabe, I., Dirras, G., Ameyama, K., 2016a. Three-dimensionally gradient and periodic harmonic structure for high performance advanced structural materials. Mater. Trans. 57, 1424–1432.

Vajpai, S.K., Ota, M., Zhang, Z., Ameyama, K., 2016b. Three-dimensionally gradient harmonic structure design: an integrated approach for high performance structural materials. Mater. Res. Lett. 4, 191-197.

Vandergiessen, E., Needleman, A., 1995. Discrete Dislocation Plasticity - a Simple Planar Model. Modelling and Simulation in Materials Science and Engineering. 3, 689-735.

Venkatramani, G., Ghosh, S., Mills, M., 2007. A size-dependent crystal plasticity finite-element model for creep and load shedding in polycrystalline titanium alloys. Acta. Materialia. 55, 3971-3986.

Venkatramani, G., Kirane, K., Ghosh, S., 2008. Microstructural parameters affecting creep induced load shedding in Ti-6242 by a size dependent crystal plasticity FE model. Int. J. Plast. 28, 428-454.

Wang, Y., Chen, M.-W., Zhou, F., Ma, E., 2002. High tensile ductility in a nanostructured metal. Nature, 419, 912-915.

Wang, X., Cazes, F., Li, J., Hocini, A., Ameyama, K., Dirrsa, G., 2019. A 3D crystal plasticity model of monotonic and cyclic simple shear deformation for commercial-purity polycrystalline Ti with a harmonic structure. Mech. Mater. 128, 117-128.

Wang, X., Li, J., Cazes, F., Dirras, G., Hocini, A., 2020. Numerical modeling on strengthening mechanisms of the harmonic structured design on CP-Ti and Ti-6Al-4V. Int. J. Plasticity.

Wang, X., Li, J., Cazes, F., Dirras, G., 2020. A three-dimensional microstructure-based crystal plasticity model for coarse-grained and harmonic-structured Ti-6Al-4V under monotonic and cyclic shear loading. Acta Mechanica.

Weng, G.J., 1981. Self-consistent determination of time-dependent behavior of metals. J. Appl. Mech. 48, 41-46.

Wei, Q., Cheng, S., Ramesh, K.T., Ma, E., 2004. Effect of nanocrystalline and ultrafine grain sizes on the strain rate sensitivity and activation volume: fcc versus bcc metals. Mater. Sci. Eng. A 381, 71–79.

Wei, Y.G., Hutchinson, J.W., 1997. Steady-state crack growth and work of fracture for solids characterized by strain gradient plasticity. Journal of the Mechanics and Physics of Solids. 45, 1253-1273.

Wei, Y.J., Li, Y.Q., Zhu, L.C., Liu, Y., Lei, X.Q., Wang, G., Wu, Y.X., Mi, Z.L., Liu, J.B., Wang, H.T., Gao, H.J., 2014. Evading the strength–ductility trade-off dilemma in steel through gradient hierarchical nanotwins. Nature Communications. 5, 3580.

Williams, J.C., Baggerly, R.G., Paton, N.E., 2002. Deformation behavior of HCP Ti-Al alloy single crystals. Met. Mat. Trans. 33, 837-850.

Witkin, D., Lee, Z., Rodriguez, R., Nutt, S., Lavernia, E.J., 2003. Al–Mg alloy engineered with bimodal grain size for high strength and increased ductility. Scripta Mater. 49, 297-302.

Wu, X.L., Yuan, F.P., Yang, M.X., Jiang, P., Zhang, C.X., Chen, L., Wei, Y.G., Ma, E., 2015. Nanodomained Nickel Unite Nanocrystal Strength with Coarse-Grain Ductility. Scientific Reports. 5, 11728.

Wu, X.L., Yang, M.X., Yuan, F.P., Wu, G.L., Wei, Y.J., Huang, X.X., Zhu, Y.T., 2015. Heterogeneous lamella structure unites ultrafine-grain strength with coarse-grain ductility. National Acad Sciences. 112, 14501-14505.

Xu, Y.L., 2015. On the Development of a Multi-scale Modelling Framework to Study Plasticity and Damage through the Coupling of Finite Element Crystal Plasticity and Discrete Dislocation Plasticity. PhD thesis. Imperial College London.

Yang, Y., Wang, L., Zambaldi, C., Eisenlohr, P., Barabash, R., Liu, W., Stoudt, M.R., Crimp, M.A., Bieler, T.R., 2011. Characterization and modeling of heterogeneous deformation in commercial purity titanium. JOM. 63, 66-73.

Yoo, M.H., 1981. Slip, Twinning, and Fracture in Hexagonal Close-Packed Metals. Met. Trans. A, 12, 409-418.

Yu, H., Watanabe, I., Ameyama, K., 2015. Deformation behavior analysis of harmonic structure materials by multi-scale finite element analysis. Adv. Mater. Res. 1088, 853–857.

Zaefferer, S., 2003. A study of active deformation systems in titanium alloys: dependence on alloy composition and correlation with deformation texture. Mater. Sci. Eng. A 344, 20-30.

Zhang, M., Zhang, J., McDowell, D.L., 2007. Microstructure-based crystal plasticity modeling of cyclic deformation of Ti-6Al-4V. Int. J. Plast. 23(8), 1328-1348.

Zhang, Z., Vajpai, S.K., Orlov, D., Ameyama, K., 2014. Improvement of mechanical properties in SUS304L steel through the control of bimodal microstructure characteristics. Mater. Sci. Eng. A 598, 106–113.

Zhang, Z., Orlov, D., Vajpai, S.K., Tong, B., Ameyama, K., 2015. Importance of bimodal structure topology in the control of mechanical properties of a stainless steel. Adv. Eng. Mater. 17, 791–795.

Zhang, Z., Ma, H., Zheng, R., Hu, Q., Nakatani, M., Ota, M., Chen, G., Chen, X., Ma, C., Ametama, K., 2017. Fatigue behavior of a harmonic structure designed austenitic stainless steel under uniaxial stress loading. Mater. Sci. Eng. A. 707, 287-294.

Zheng, R., Zhang, Z., Nakatani, M., Ota, M., Chen, X., Ma, C., Ametama, K., 2016. Enhanced ductility in harmonic structure designed SUS316L produced by high energy ball milling and isostatic sintering. Mater. Sci. Eng. A. 674, 212-220.